

Mohamed Khider University of Biskra Faculty of Exact Sciences Material Sciences Department

MASTER DISSERTATION

Field of Material Sciences
Physics
Specialty: Energetic Physics and Renewable Energies

Réf.: Entrez la référence du document

Presented by:

BRAHMI Douaa

THE:02/06/2025

Study of multilayer solar cells based on GaInP/GaAs heterojunction

Jury:

Ms	LAZNEK Samira	MCA	Med Khider University of Biskra	President
Ms	MEFTAH Amjad	Professor	Med Khider University of Biskra	Supervisor
Mss	ATTAFI Diemaa	MCB	Med Khider University of Biskra	Examiner

AcademicYear: 2024/2025

W

Dedication

With pride, I dedicate my work:

To the one whose prayers were the secret of my success, whose tenderness healed my wounds, and whose presence gave me strength—my dearest mother, **Fadila Merzouk**. No words can ever do you justice.

To the one whose name I carry with pride and whose support was my constant strength—my beloved father, **Abdelhamid**, my role model and safe haven.

To my dear sisters—**Khawla, Naima, Madiha, and Khadidja**—thank you for your love, encouragement, and unwavering support at every step.

And to their children—Nour, Aicha, Abdelrahman, Mohamed, Saleh, Israa, Abdelrazak, Mohamed Ouwab, Fatima, and Houmam.

To everyone who has had an impact on my journey, I extend my deepest gratitude and appreciation. With you, my path has been filled with achievements and beautiful meanings.



Acknowledgement

Praise be to ALLAH, by whose grace and guidance I was able to complete this graduation thesis.

I extend my deepest gratitude to my supervisor, **Pr. Meftah Amjad**, who has been more than an academic mentor—she has been a pillar of support throughout this journey. Her meticulous guidance, unwavering patience, and invaluable advice have played a crucial role in shaping and refining this work. She never hesitated to provide assistance and generously shared her expertise, making this experience truly enriching and meaningful.

I also express my sincere appreciation to the members of the examination committee—**Pr. Laznek Samira**, the chair of the committee, and **Pr. Attafi Djemaa**, the examiner—for their time and effort in reviewing and evaluating this thesis.

Finally, I hold immense appreciation for my family and friends, whose unwavering support and encouragement have been a driving force behind this achievement.

May ALLAH bless them all.

Abstract

We conducted a study on multilayer solar cells based on a GaInP/GaAs heterojunction, analysing the performance of both single-junction and dual-junction tandem solar cells under standard irradiation conditions (AM1.5),with solar an optical of $P_{opt} = 0.099271 \, W/cm^2$ at a temperature of T = 300K. Using Solis-1D simulation software, we determined the electrical characteristics of these solar cells, including current densityvoltage (I - V) and power-voltage (P - V) profiles, and extracted key photovoltaic parameters such as short-circuit current density (J_{sc}) , open-circuit voltage (V_{oc}) , maximum power (P_{max}) , fill factor (FF), and conversion efficiency (E_{ff}). For the single-junction solar cell, our investigation focused on optimizing layer thickness and doping concentrations to maximize conversion efficiency. The results revealed that reducing the thickness of the N⁺-type $In_{0.4}Ga_{0.6}P$ and N^+ -type $In_{0.5}Ga_{0.5}P$ layers to 0.01 μm , while simultaneously increasing the P-type GaAs base layer thickness to 3.5 μ m and doping it at a concentration of $10^{17} cm^{-3}$, significantly enhanced the conversion efficiency (E_{ff}) from 26.92% to 29.088%. For the dualjunction tandem solar cell, performance was further improved by increasing the thickness of the P-type $In_{0.4}Ga_{0.6}P$ base layer in the top sub-cell to 0.94 μm . This optimization facilitated current density matching (J_{sc}) between the top and bottom sub-cells, ultimately raising the overall efficiency from 25.77% to 35.93%. These findings underscore the crucial role of doping concentration and layer thickness optimization, as well as current matching between sub-cells, in enhancing photovoltaic performance and maximizing solar cell efficiency.

Keywords: GaInP/GaAs heterojunction; Solar cells; Multilayers; Solis-1D; Conversion efficiency; Solar energy.

Table of contents

DedicationII
AcknowledgementIV
Abstract
Table of contentsV
List of figures
List of tablesXIV
General introduction2
References
Chapter I: Photovoltaic Solar Cells
I.1. Introduction
I.2 The Solar Spectrum
I.3 Solar Cell as p-n Junction Diode
I.4 Equivalent Circuit and Analysis of a Solar Cell as a Diode12
I.5 Parameters of a Solar Cell13
I.5.1 Short-Circuit Current (I_{SC})13
I.5.1 Short-Circuit Current (I _{SC})1
I.5.1 Short-Circuit Current (I_{SC})
I.5.1 Short-Circuit Current (I_{SC}) 13I.5.2 Open-Circuit Voltage (V_{OC}) 14I.5.3 Fill Factor (FF) 15
I.5.1 Short-Circuit Current (I_{SC}) 13I.5.2 Open-Circuit Voltage (V_{OC}) 14I.5.3 Fill Factor (FF) 15I.5.4 Conversion Efficiency (E_{ff}) 15
I.5.1 Short-Circuit Current (I_{SC}) 13I.5.2 Open-Circuit Voltage (V_{OC}) 14I.5.3 Fill Factor (FF) 15I.5.4 Conversion Efficiency (E_{ff}) 15I.5.5 Characteristic Resistance (R_{CH}) 16
I.5.1 Short-Circuit Current (I_{SC}) 13I.5.2 Open-Circuit Voltage (V_{OC}) 14I.5.3 Fill Factor (FF) 15I.5.4 Conversion Efficiency (E_{ff}) 15I.5.5 Characteristic Resistance (R_{CH}) 16I.5.6 Series (R_S) and Shunt (R_{SH}) Resistances17
I.5.1 Short-Circuit Current (I_{SC}) 13I.5.2 Open-Circuit Voltage (V_{OC}) 14I.5.3 Fill Factor (FF) 15I.5.4 Conversion Efficiency (E_{ff}) 15I.5.5 Characteristic Resistance (R_{CH}) 16I.5.6 Series (R_S) and Shunt (R_{SH}) Resistances17I.5.7 Quantum Efficiency (QE) 17
I.5.1 Short-Circuit Current (I_{SC}) 13I.5.2 Open-Circuit Voltage (V_{OC}) 14I.5.3 Fill Factor (FF) 15I.5.4 Conversion Efficiency (E_{ff}) 15I.5.5 Characteristic Resistance (R_{CH}) 16I.5.6 Series (R_S) and Shunt (R_{SH}) Resistances17I.5.7 Quantum Efficiency (QE) 17I.5.8 Spectral Response (SR) 19
I.5.1 Short-Circuit Current (I_{SC}) 13I.5.2 Open-Circuit Voltage (V_{OC}) 14I.5.3 Fill Factor (FF) 15I.5.4 Conversion Efficiency (E_{ff}) 15I.5.5 Characteristic Resistance (R_{CH}) 16I.5.6 Series (R_S) and Shunt (R_{SH}) Resistances17I.5.7 Quantum Efficiency (QE) 17I.5.8 Spectral Response (SR) 18I.6 Solar Cells Generations19

I.6.4 Fourth-generation of photovoltaic cells26
I.7 Conclusion26
I.8 References
Chapter II: GaInP/GaAs Solar Cells32
II.1 Introduction33
II.2 Overview of III-V Compound Semiconductors for Photovoltaics and High-Efficiency
Solar Cells34
II.3 Gallium Arsenide and Gallium Indium Phosphide for photovoltaics and high-
efficiency solar cells38
II.3.1 Gallium Arsenide (GaAs)38
II.3.2 Indium Phosphide39
II.3.3 Gallium Indium Phosphide (GaInP)40
II.4 Multi-Junction Solar Cells41
II.4.1 Single Junction Solar Cells:41
II.4.2 InGaP/GaAs Double Junction Solar Cells41
II.5. Bandgap Engineering in GaInP/GaAs Solar Cells43
II.6 Multi-junction approach45
II.7 Conclusion47
II.8 References:49
Chapter III: Study of Multilayer Solar Cells Based on GaInP/GaAs Heterojunction 59
III.1 Introduction60
III.2. 1D Semiconductor Device Simulator: Solis60
III.2.1 Modeling, numerical methods, and implementation61
III.2.2 Solis Input File Format65
III.2.3. Solis tools
III.3 Description of the studied multilayer solar cells based on GaInP/GaAs
heterojunction73
III.4 Results and discussion76
III 4.1 Single solar cell based on CaInD/CaAs betarojunction 76

III.4.2 Effect of thickness variation on the photovoltaic output parameters of	f the single
solar cell based on GaInP/GaAs heterojunction	80
III.4.3 Effect of doping variation on the photovoltaic output parameters of th	ıe single
solar cell based on GaInP/GaAs heterojunction	88
III.4.4 Tandem solar cell based on GaInP/GaAs heterojunction	94
III.5 Conclusion	100
III.6. References	102
General conclusion	105

List of figures

Chapter I: Photovoltaic Solar Cells

Figure	Titles	Page
number	Titles	
I.1	Solar spectrum along with various atmospheric absorbing these	9
1.1	radiations in range of 240 nm to 2.5 µm wavelengths.	9
I.2	Solar cell as p-n junction diode.	10
	I - V characteristics of a solar cell.	10
I.3	1 – V Characteristics of a solar cen.	11
I.4	I-V Curve of a solar cell: (a) without light; (b) when sunlight	10
1.4	shines on the cell; (c) with greater light intensity; and (d) solar	13
	cell curve is flipped by convention.	
I.5	Characteristic resistance of a solar cell.	16
	A schematic diagram of the equivalent circuit of a solar cell.	
I.6	A schematic diagram of the equivalent circuit of a solar cen.	17
1.7	Graphical representation of QE of a silicon solar cell.	10
I.7		18
I.8	Various solar cell types and current developments within this	20
	field.	
	Examples of photovoltaic cell efficiencies.	_
I.9		21
I.10	Schematic illustration of a triple-junction cell and approaches	25
	for improving efficiency of the cell.	

Chapter II: GaInP/GaAs Solar Cells

Figure number	Titles	Page number
II.1	Diagram illustrating various compound semiconductors.	34
II.2	Bandgap energy as a function of lattice constant for different III-V materials.	35
II.3	Theoretical Shockley-Queisser (SQ) detailed balance efficiency limit as a function of bandgap for single junction solar cells under AM1.5G illumination [39]. The points represent the record efficiencies for the typical III-V cells including GaAs, InP, and InGaP.	39
II.4	(a) Schematic illustration of the electron-hole pairs generation process in the bandgap material (E_g) excited by light photons with different energies (hv) . (b) Schematic illustration of the absorption of solar spectrum for each subcell in multijunction (MJ) solar cells. (c) Schematic illustration of flexible InGaP/GaAs tandem solar cells, (d) and the corresponding EQE spectrum of each subcell.	42
II.5	The layered structure of a GaInP/GaAs tandem solar cell.	44
II.6	Schematic comparison of (a) spatial-configuration approaches and (b) stacked configuration approaches to distributing light to subcells of different band gaps. (c) Illustration of two-, three-, and four-terminal connection to a two-junction cell. The figure shows the subcells as mechanically separate, but the two- and three-terminal devices can be monolithic	46

Chapter III: Study of Multilayer Solar Cells Based on GaInP/GaAs Heterojunction

Figure	Titles	Page
number	Titles	number
III.1	A schematic of the Solis architecture. The core part of Solis is entirely	64
	coded in standard C++ (the Lua engine being coded in standard C)	
	and is easily portable to almost all operating systems, in addition to	
	the natively supported Windows and Linux systems. The Solis code	
	editor, device editor, and data plotter are developed in C and use the	
	IUP GUI toolkit coded in C [7] and the Scintilla component coded in	
	C++.	
III.2	A schematic structure of a device as simulated by Solis.	65
III.3	Solis Input Syntax.	66
III.4	SolisEdit Screenshot.	67
III.5	SolisDevice Screenshot.	68
III.6	SolisDevice : Parameters Dialog.	69
III.7	SolisDevice: Doping Dialog.	69
III.8	SolisDevice : Traps Dialog	70
III.9	SolisDevice: Refractive Index and Extinction Coefficient Dialog.	70
III.10	SolisDevice: Anode and Cathode Dialog.	71
III.11	SolisDevice: Voltage and Light Dialog.	71
III.12	SolisPlot Screenshot.	72
III.13	(J-V) curve from SolisPlot.	73

III.14	Structure of the studied solar cells based on GaInP/GaAs heterojunction: (a) Single solar cell, (b)tandem solar cell.	75
III.15	Band gap diagram at thermal equilibrium for the single solar cell.	77
III.16	Band gap diagram at short circuit conditions for the single solar cell.	78
III.17	Band gap diagram at open circuit conditions for the single solar cell.	78
III.18	Free carrier density distributions at thermal equilibrium, short and open circuit conditions for the single solar cell.	79
III.19	J-V and $P-V$ electrical characteristics under the AM1.5 standard pectrum for the single solar cell.	80
III.20	Dependence of photovoltaic output parameters on the thickness of the N^+ -type ZnO layer in the single solar cell.	81
III.21	Thickness variation effect of the N ⁺ -type $In_{0.4}Ga_{0.6}P$ layer on: (a) $J - V$ characteristics and (b) photovoltaic output parameters of	82
	the single solar cell.	
III.22	Thickness variation effect of the N ⁺ -type $In_{0.5}Ga_{0.5}P$ layer on: (a) $J-V$ characteristics and (b) photovoltaic output parameters of the single solar cell.	84
III.23	Thickness variation effect of the P-type GaAs layer on: (a) $J-V$ characteristics and (b) photovoltaic output parameters of the single solar cell.	86
III.24	Dependence of photovoltaic output parameters on the thickness of the P^+ -type $\mathrm{Al}_{0.4}\mathrm{G}a_{0.6}\mathrm{As}$ layer in the single solar cell.	87
III.25	Dependence of photovoltaic output parameters on the donor doping concentration (N_d) of the N ⁺ -type I $n_{0.4}$ G $a_{0.6}$ P layer in the single solar cell.	89
III.26	Dependence of photovoltaic output parameters on the donor doping concentration (N_d) of the N ⁺ -type I $n_{0.5}$ G $a_{0.5}$ P layer in the single solar cell.	89

III.27	Effect of the acceptor doping concentration (N_a) of the P-type GaAs	91
111,21	layer on: (a) $J - V$ characteristics and (b) photovoltaic output	31
	parameters of the single solar cell.	
111.00	Effect of the P-type doping concentration in the GaAs base layer on	00
III.28	the distribution of: (a) the direct (radiative) recombination rate (R_D) ,	93
	(b) the Auger recombination rate (R_A) and (c) the Shockley-Read-	
	Hall recombination rate (R_{SRH}) .	
111.00	Dependence of photovoltaic output parameters on the acceptor	0.4
III.29	doping concentration (N_a) of the P ⁺ -type Al _{0.4} G $a_{0.6}$ As layer in the	94
	single solar cell.	
111.00	Energetic band gap diagram at thermal equilibrium of the tandem	95
III.30	solar cell based on GaInP/GaAs heterojunction.	
III 21	Energetic band gap diagram at short circuit conditions of the tandem	95
III.31	solar cell based on GaInP/GaAs heterojunction.	33
111 22	Energetic band gap diagram at open circuit conditions of the tandem	96
III.32	solar cell based on GaInP/GaAs heterojunction.	90
111.00	J-V characteristics of the top sub-cell, bottom sub-cell, and tandem	0.7
III.33	solar cell based on GaInP/GaAs heterojunction, under the AM1.5	97
	standard solar spectrum.	
111.04	Dependence of the top sub-cell output photo-parameters on the base	00
III.34	layer thickness (P-type $In_{0.4}Ga_{0.6}P$) of the top sub-cell.	99
111.25	J-V characteristics of the top sub-cell, bottom sub-cell, and tandem	99
III.35	solar cell based on GaInP/GaAs heterojunction under the AM1.5	
	standard solar spectrum, with the achievement of the current	
	matching condition between the top and bottom sub-cells.	

List of tables

Chapter III: Study of Multilayer Solar Cells Based on GaInP/GaAs Heterojunction

Table number	Titles	Page number
III.1	The normalization factors employed in the drift-diffusion model.	62
III.2	Baseline parameters for modeling the single and tandem solar cells based on GaInP/GaAs heterojunction at $T = 300 ^{\circ}K$.	75
III.3	Photovoltaic output parameters of the single solar cell based on GaInP/GaAs heterojunction.	80
III.4	Dependence of photovoltaic output parameters on the thickness of the N ⁺ -type $In_{0.4}Ga_{0.6}P$ layer in the single solar cell.	83
III.5	Dependence of photovoltaic output parameters on the thickness of the N ⁺ -type $In_{0.5}Ga_{0.5}P$ layer in the single solar cell.	85
III.6	Dependence of photovoltaic output parameters on the thickness of the P-type GaAs layer in the single solar cell.	87
III.7	Dependence of photovoltaic output parameters on the acceptor doping concentration (N_a) of the P-type GaAs layer in the single solar cell.	91
III.8	Photovoltaic output parameters of the top sub-cell, bottom sub-cell, and tandem solar cell based on GaInP/GaAs heterojunction.	98
111.9	Photovoltaic output parameters of the top sub-cell, bottom sub-cell, and tandem solar cell based on GaInP/GaAs heterojunction, with the achievement of the current matching condition between the top and bottom sub-cells.	100

General introduction

Solar energy is one of the most prominent sources of renewable energy due to its continuous availability and minimal environmental impact. Solar cells play a key role in directly converting sunlight into electrical energy, making them an effective solution to meet the growing demand for energy. Since the invention of the first solar cell, this technology has progressed significantly, leading to the emergence of several generations and types of solar cells that differ in their structure, efficiency, and cost. Recent advancements in solar cell technologies have contributed to improving performance and increasing efficiency, especially with the development of multilayer cells. These cells are characterized by their ability to absorb a wider range of the solar spectrum, which improves energy conversion compared to traditional designs. Additionally, integrating them into tandem structures helps reduce energy losses and enhances the overall performance of the device, making them a promising option for a sustainable energy future [1-4].

Heterojunction solar cells based on GaInP/GaAs are among the most effective and advanced structures in the field of photovoltaic technology. These cells employ semiconductor materials known for their exceptional electronic and optical properties. The tunable bandgap allows for optimized light absorption across a wide range of the solar spectrum, while the good lattice matching between GaInP and GaAs layers minimizes structural defects at the interface, thereby enhancing energy conversion efficiency and reducing losses [5,6].

The GaInP/GaAs solar cells have demonstrated remarkably high performance, making them a preferred choice for advanced applications, particularly in the aerospace sector. They are widely used to power satellites and spacelab due to their ability to survive harsh environmental conditions and deliver high conversion efficiencies. These cells are indeed among the most efficient photovoltaic technologies, primarily due to their high bandgap tunability, low defect density, and excellent lattice matching properties. Additionally, advancements in multijunction architectures involving GaInP/GaAs layers have paved the way for next-generation solar technologies with higher efficiencies. [7,8].

The GaInP/GaAs solar cells are available in two primary configurations, each differing in design and light absorption efficiency. The first type, single-junction solar cells, utilize a single junction to absorb sunlight and generate electrical energy. However, their spectral absorption is limited, restricting their overall efficiency. The second type, tandem (multi-junction) solar cells,

incorporate multiple layers with varying bandgaps (E_g), allowing them to capture photons across a wider range of the solar spectrum. This layered structure significantly enhances energy conversion efficiency. The transition toward multi-junction architectures has been recognized as a key advancement in modern solar energy technologies, enabling improved performance and more effective utilization of solar radiation [9, 10].

Study objectives:

In this study, we will focus on the analysis of multi-layer solar cells based on GaInP/GaAs heterojunction structures, specifically examining two distinct configurations: a single-junction solar cell and a dual-junction tandem cell. The single-junction solar cell is composed of the following layers: a highly doped N-type (N⁺) ZnO region, a highly doped N-type (N⁺) $In_{0.4}Ga_{0.6}P$ region, a highly doped N-type (N⁺) $In_{0.5}Ga_{0.5}P$ region, a doped P-type GaAs region, and a highly doped P-type (P⁺) $Al_{0.4}Ga_{0.6}As$ region. The dual-junction tandem solar cell consists of the following layers: a highly doped N-type (N⁺) ZnO region, a highly doped N-type (N⁺) $In_{0.4}Ga_{0.6}P$ region, a doped P-type $In_{0.4}Ga_{0.6}P$ region, a highly doped P-type (P⁺) $In_{0.4}Ga_{0.6}P$ region, a highly doped N-type (N⁺) $In_{0.5}Ga_{0.5}P$ region.

In this investigation, the solar cells are subjected to standard solar irradiation AM1.5, with an optical power (P_{opt}) of 0.099271 W/cm^2 at an ambient temperature of T=300K. The performance of these cells is evaluated through numerical simulations using the Solis-1D simulation software, which facilitates the computation of their electrical properties, such as current density-voltage (J-V) and power-voltage (P-V) characteristics. From the simulation results, we extract key photovoltaic output parameters, including: short-circuit current density (J_{sc}) , open-circuit voltage (V_{oc}) , maximum output power (P_{max}) , fill factor (FF) and photovoltaic conversion efficiency (E_{ff}) .

By systematically analysing the effects of varying layer thickness and doping concentrations, this study aims to enhance the photovoltaic conversion efficiency of both the single-junction and dual-junction tandem solar cells, paving the way for further optimization in solar energy technologies.

Thesis organization:

The master's thesis is structured into three main chapters, framed by a comprehensive introduction and a conclusion. Below is an overview of each chapter:

Chapter I: Photovoltaic Solar Cells; this chapter provides a detailed examination of photovoltaic solar cells, covering fundamental aspects such as the solar spectrum, principles of photovoltaic conversion, operational mechanisms, and key photovoltaic parameters. Additionally, it explores the evolution of solar cell technologies across different generations, highlighting their advancements and efficiency improvements.

Chapter II: GaInP/GaAs Solar Cells; this chapter explores the fundamental principles, materials, and recent advancements that define GaInP/GaAs solar cells. It underlines their technological significance and potential applications, particularly in next-generation renewable energy systems. The discussion also highlights their structural advantages and superior performance in energy conversion.

Chapter III: Study of Multilayer Solar Cells Based on GaInP/GaAs Heterojunction; this chapter focuses on analysing the performance of multi-layer solar cells based on GaInP/GaAs heterojunctions using the advanced Solis-1D simulation software. The study includes numerical modelling of single-junction and dual-junction tandem configurations under standard AM1.5 solar irradiation. Key findings, including the current density-voltage (J - V) and power-voltage (P - V) characteristics, will be presented, discussed, and analyzed. The objective is to gain deeper understandings of the operational behavior of these solar cells and contribute to the development of high-efficiency photovoltaic devices.

The general introduction provides a comprehensive context for the research topic and offers an overview of the study. The general conclusion summarizes the major findings and discusses their potential implications.

References

- [1] M.D. Archer, M.A. Green, 2014 (2 nd edition). Clean electricity from photovoltaics. *Imperial College Press*, https://doi.org/10.1142/p139
- [2] A.K. Pal, H.C.Potter, 2019. Advances in solar energy: Solar cells and their applications. In: Tyagi, H., Agarwal, A., Chakraborty, P., Powar, S. (Eds.), *Advances in Solar Energy Research*. Energy, Environment, and Sustainability, Springer, Singapore. https://doi.org/10.1007/978-981-13-3302-6_4
- [3] A.H. Alami, S. Alasad, H. Aljaghoub, M. Ayoub, A. Alashkar, A. Mdallal, R. Hasan, 2023. Recent Advances in Solar Cells. Springer, Cham. https://doi.org/10.1007/978-3-031-31349-3_10
- [4] A. Farajollahi, 2025. Nanotechnology in solar energy: From active systems to Advanced Solar cells. *Frontiers in Energy Research*. https://doi.org/10.3389/fenrg.2025.1560718
- [5] A. Myllynen, T. Sadi, J. Oksanen, 2020. Interdigitated back-contact double-heterojunction GaInP/GaAs solar cells. *Progress in Photovoltaics: Research and Applications*. https://doi.org/10.1002/pip.3339.
- [6] M. Steiner, R. France, J. Buencuerpo Farina, J. Simon, W. McMahon, 2019. Rear heterojunction GaAs solar cells with strain-balanced GaInAs/GaAsP quantum wells. 46th IEEE Photovoltaic Specialists Conference, PVSC 2019. https://doi.org/10.1109/PVSC40753.2019.8980576.
- [7] J. Schön, G.M.M.W. Bissels, R.H.van Leest, N. Gruginskie, P. Mulder, E. Vlieg, D. Lackner, 2022. Improvements in ultra-light and flexible epitaxial lift-off GaInP/GaAs/GaInAs solar cells for space applications. Progress in Photovoltaics: Research and Applications. https://doi.org/10.1002/pip.3542.
- [8] K.A. Bertness, D.J. Friedman, S.R. Kurtz, A.E. Kibbler, C. Kramer, J.M. Olson, 1994. High efficiency GaInP/GaAs tandem solar cells. IEEE Aerospace and Electronic Systems Magazine. https://doi.org/10.1109/62.334755.
- [9] J.M. Olson, S.R. Kurtz, A.E. Kibbler, P. Faine, 1990. Recent advances in high-efficiency GaInP2/GaAs tandem solar cells. Twenty First IEEE Photovoltaic Specialists Conference 1990 Part 2 (of 2), Kissimmee, FL, USA. https://research-

General introduction

- hub.nrel.gov/en/publications/recent-advances-in-high-efficiency-gainp2 gaastandem-solar-cells.
- [10] I. Zidani, Z.Bensaad, N. Hadroug, A. Kouzou, A.Hafaifa, J. Rodriguez, M. Abdelrahem, 2025. Modeling and optimization of enhanced high-efficiency InGaP/GaAs tandem solar cells without anti-reflective coating. Applied Sciences, 15(7), 3520. https://doi.org/10.3390/app15073520.

Chapter I Photovoltaic Solar Cells

I.1. Introduction

Solar cells are the electrical devices that directly convert solar energy (sunlight) into electric energy. This conversion is based on the principle of photovoltaic effect in which DC voltage is generated due to flow of electric current between two layers of semiconducting materials (having opposite conductivities) upon exposure to the sunlight [1]. A solar cell is a type of photoelectric cell which consists of a p-n junction diode. Solar cells are also called photovoltaic (PV) cells. An intrinsic (pure or undoped) semiconducting material like silicon (Si) or germanium (Ge) does not contain any free charge carriers. They contain four electrons in their outermost shell and just act like resistors [2]. The conductivity of such intrinsic semiconductors can be improved by adding specific impurities within the crystal lattice of it. This process is called doping.

This chapter provides an overview of photovoltaic solar cells, addressing the following aspects: the solar spectrum, the fundamental principles of solar cells, their operation and photovoltaic parameters, and finally, the different generations of solar cells.

I.2 The Solar Spectrum

Sun is the ultimate source of energy on earth, and various radiations emitted by the sun are called solar radiations [3]. A solar spectrum as shown in Figure I.1 is obtained when solar radiations are plotted in terms of wavelength (nanometers) and irradiance (Wm⁻² nm⁻¹) [4].

Some of the important points concluded from the solar spectrum are [4]:

- Below 750 nm, majority of the solar energy falls in the visible region.
- For wavelengths less than 300 nm, O_3 and O_2 gases absorb most of the UV radiations. The O_3 gas also absorbs some visible radiations.
- When visible radiations fall on earth, 70% of these radiations reach the sea level.
- Large portion of the visible light falling on earth reflects back or gets scattered by the clouds and particles in atmosphere. Thus, a large share of visible energy never reaches the earth.
- Water vapours, O₃, and CO₂ absorb infrared radiations in the large wavelength regions.
- The major absorbers of the IR radiations are carbon dioxide, water vapours, and ozone. The energy in solar irradiation comes in the form of electromagnetic waves of a wide

spectrum [5]. The energy and wavelengths of the radiations are inversely proportional, i.e., shorter wavelengths have high energy and longer wavelengths have less energy [4].

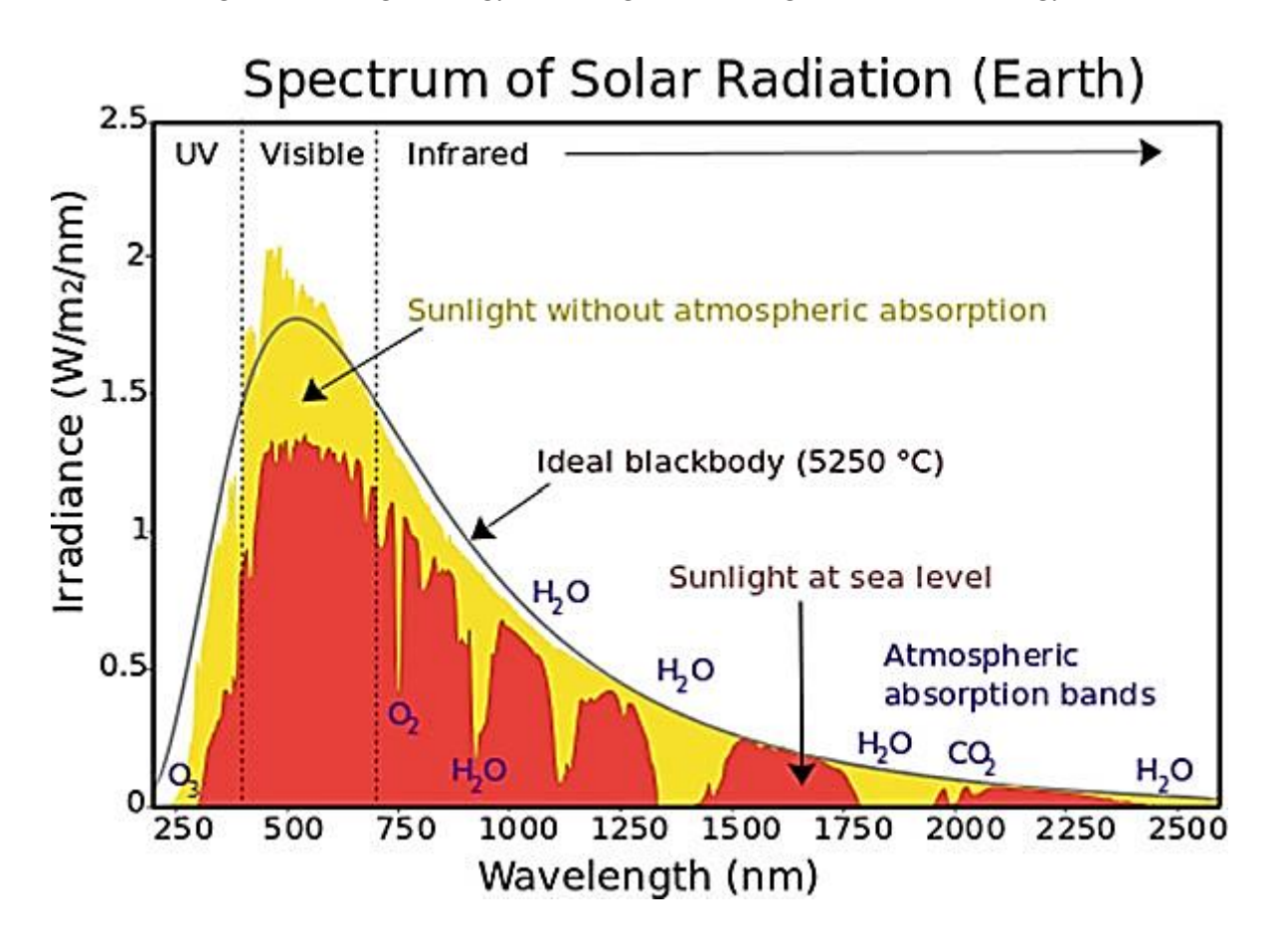


Figure I.1: Solar spectrum along with various atmospheric absorbing these radiations in range of 240 nm to 2.5 μm wavelengths [4].

I.3 Solar Cell as p-n Junction Diode

The function of a solar cell is basically similar to a p-n junction diode [6]. The construction of a solar cell is very simple. A thin p-type semiconductor layer is deposited on top of a thick n-type layer. Electrodes from both the layers are developed for making contacts. A thin electrode on the top of the p-type semiconductor layer is formed. This electrode does not obstruct light to reach the thin p-type layer. Thus, a p-n junction is formed just below the p-type layer. Similarly, a current collecting electrode is formed at the bottom of the n-type layer. The whole assembly is then encapsulated inside a thin glass to protect the solar cell from any mechanical shock. Figure I.2 shows the constructional details of basic p-n junction diode solar cell [7].

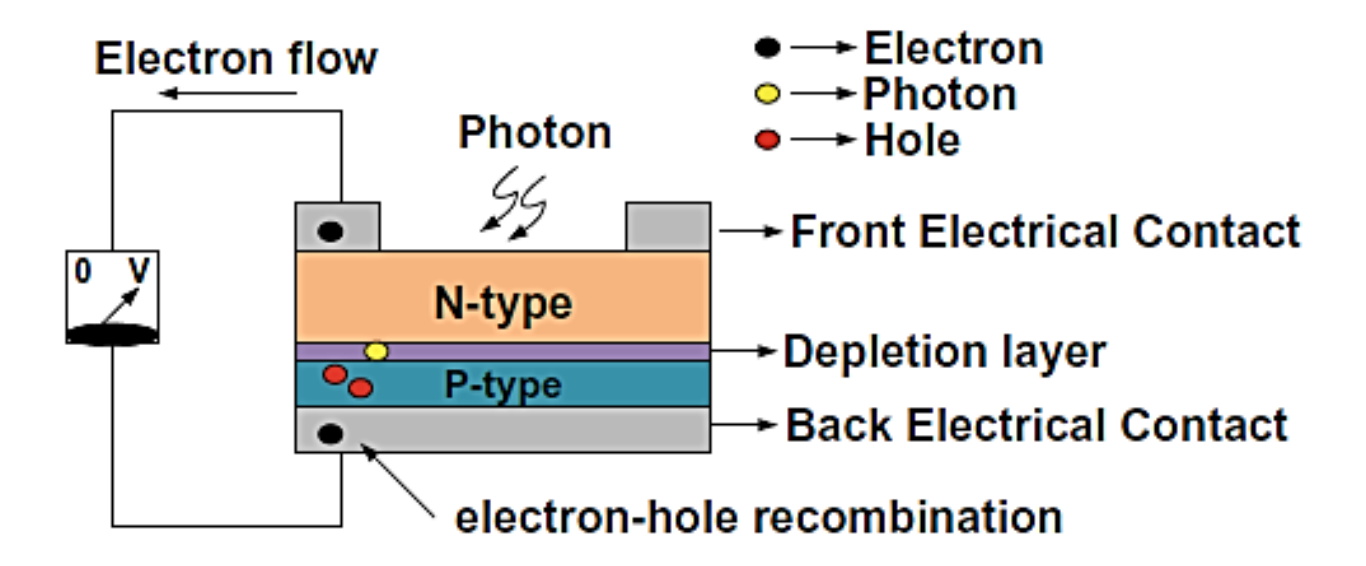


Figure I.2: Solar cell as p-n junction diode [4].

When light is incident on a solar cell, it can easily enter the p-n junction through the extremely thin N-type layer. The photons from the light contain sufficient energy to break the thermal equilibrium of the junction and thus create many electron-hole pairs in the depletion region. The electrons travel toward the n-type side of the junction, and holes travel toward the p-type side of the junction [8]. After crossing the junction, the electrons and holes cannot return to the depletion layer due to creation of a potential barrier at the junction. As the concentration of electrons and holes starts to increase on their respective sides, the p-n junction starts to behave as a battery cell. A current flow through an external load connected across the junction [4]. Plotting current vs. voltage for a particular solar cell, is called its I-V characteristics. Using I-V characteristics, the efficiency and energy conversion ability of a solar cell is calculated. By knowing P_{max} of a solar cell, the performance and solar efficiency of the device can be determined [9]. The current produced in a solar cell is directly proportional to the intensity of radiation and is governed by the photoelectric effect, i.e., with an increase in the intensity, the current increases. However, an increase in the temperature of the solar cell reduces its voltage [4]. The I-V characteristics of a solar cell are actually the graph plotted between the current and voltage of the solar cell at a particular temperature and intensity of radiation. I-Vcharacteristic curves help in providing information regarding the operating conditions where a solar cell can perform to its optimum capacity known as maximum peak power point (MPP) [4]. Figure I.3 shows the basic I - V characteristics of a solar cell. Power delivered is equal to the product of current and voltage of the solar cell. For a specific intensity of radiation, the power curve as shown in Figure I.3 can be obtained by multiplying all voltages with corresponding

currents from point to point, both for short-circuit and open-circuit condition. When the solar cell is in open-circuit condition (no load), the current will be minimum and the voltage will be maximum. This voltage is known as solar cell open-circuit voltage (V_{OC}). However, in short-circuit condition, the voltage will be minimum and the current will be maximum. This current is known as solar cell short-circuit current (I_{SC}). Thus, maximum voltage is available in a solar cell for open-circuit condition, and maximum current is available for short-circuit condition [4]. However, it is important to note that no power generates in the cell under these two conditions. A solar cell generates maximum power at a point in between these two extremes known as maximum power point (MPP). At MPP, current (I_{MP}) and voltage (V_{MP}) are maximum in the solar cell. On an I-V curve, the MPP is located near the bend as shown in Figure I.3. Because the output voltage and current of a solar cell are both temperature dependent, the actual output power will vary with variations in ambient temperature [4].

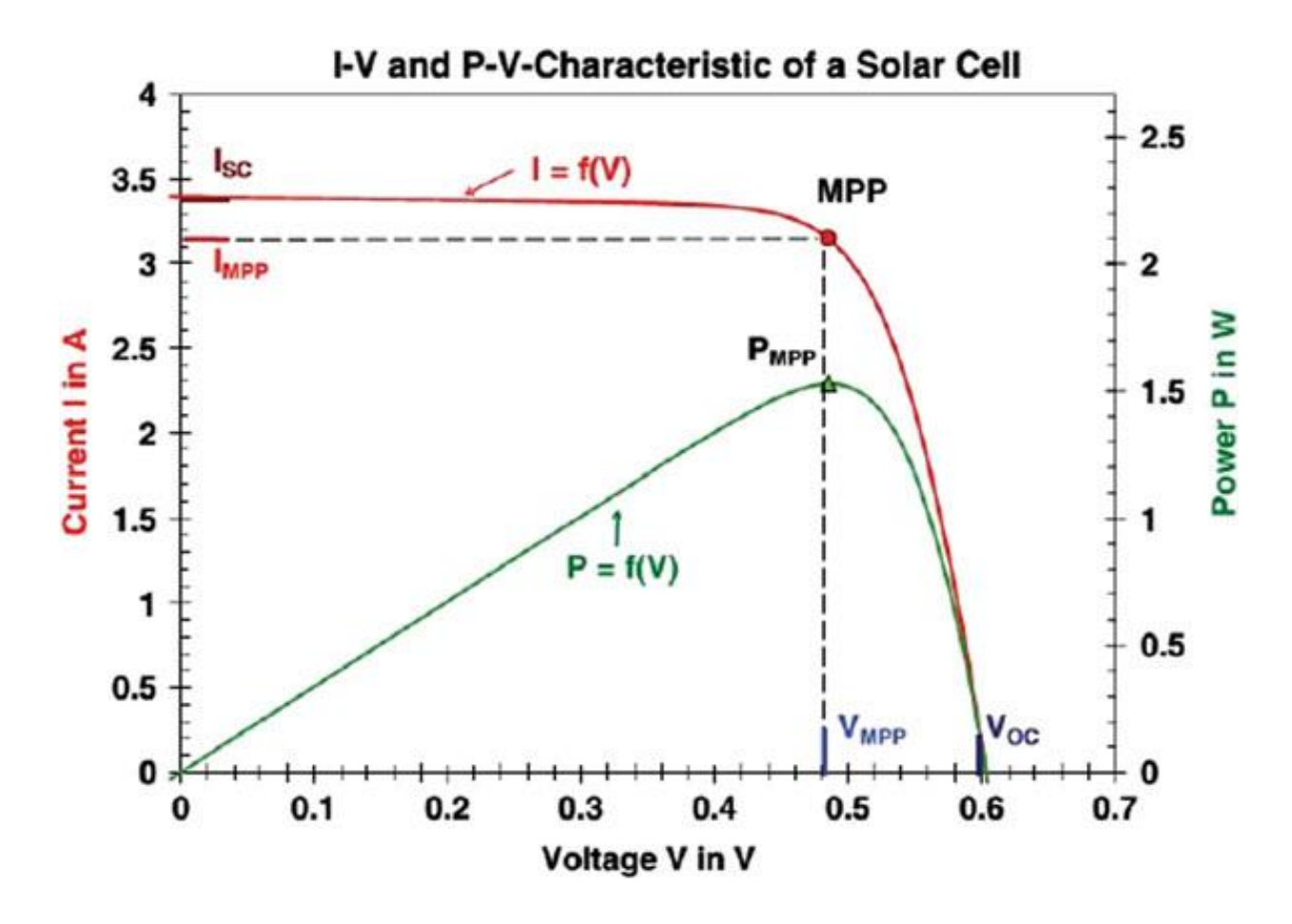


Figure I.3: I - V characteristics of a solar cell [4, 9].

I.4 Equivalent Circuit and Analysis of a Solar Cell as a Diode

The light shifts I - V curve of a solar cell into 4th quadrant as shown in Figure I.4 [3]. Without illumination, the solar cell has the same characteristics as that of a normal p-n junction diode under forward bias condition. This current is known as dark current. However, when sunlight shines on the solar cell, the I - V curve starts shifting to fourth quadrant thereby generating power and with increase in the intensity of sunlight, the shift toward fourth quadrant also increases. Illuminating a cell adds to the normal "dark" currents in the diode so that the diode law becomes [4]:

$$I = I_0 \left[exp\left(\frac{qV}{nk_BT}\right) - 1 \right] - I_L \tag{I.1}$$

Where I_L is the current generated due to sunlight, I_0 is the saturation current, η the ideality factor, k_B is the Boltzmann constant, T the temperature in degrees Kelvin and q the charge of the electron.

The above equation (Eq.I.1) is only valid for the I-V curve in the 4th quadrant. For the I-V curve in the first quadrant, the equation becomes [4]:

$$I = I_L - I_0 \left[exp\left(\frac{qV}{\eta k_B T}\right) - 1 \right]$$
 (I.2)

For voltages < 100 mV, the value of exponential term is very large and at further lower voltages, I_L term dominates. Hence, –1 term can be neglected in the equation, to give:

$$I \cong I_L - I_0 \left[exp\left(\frac{qV}{nk_BT}\right) \right] \tag{I.3}$$

Plotting the above equation gives the I - V curve as shown in Figure I.4 with the relevant points on the curve [4].

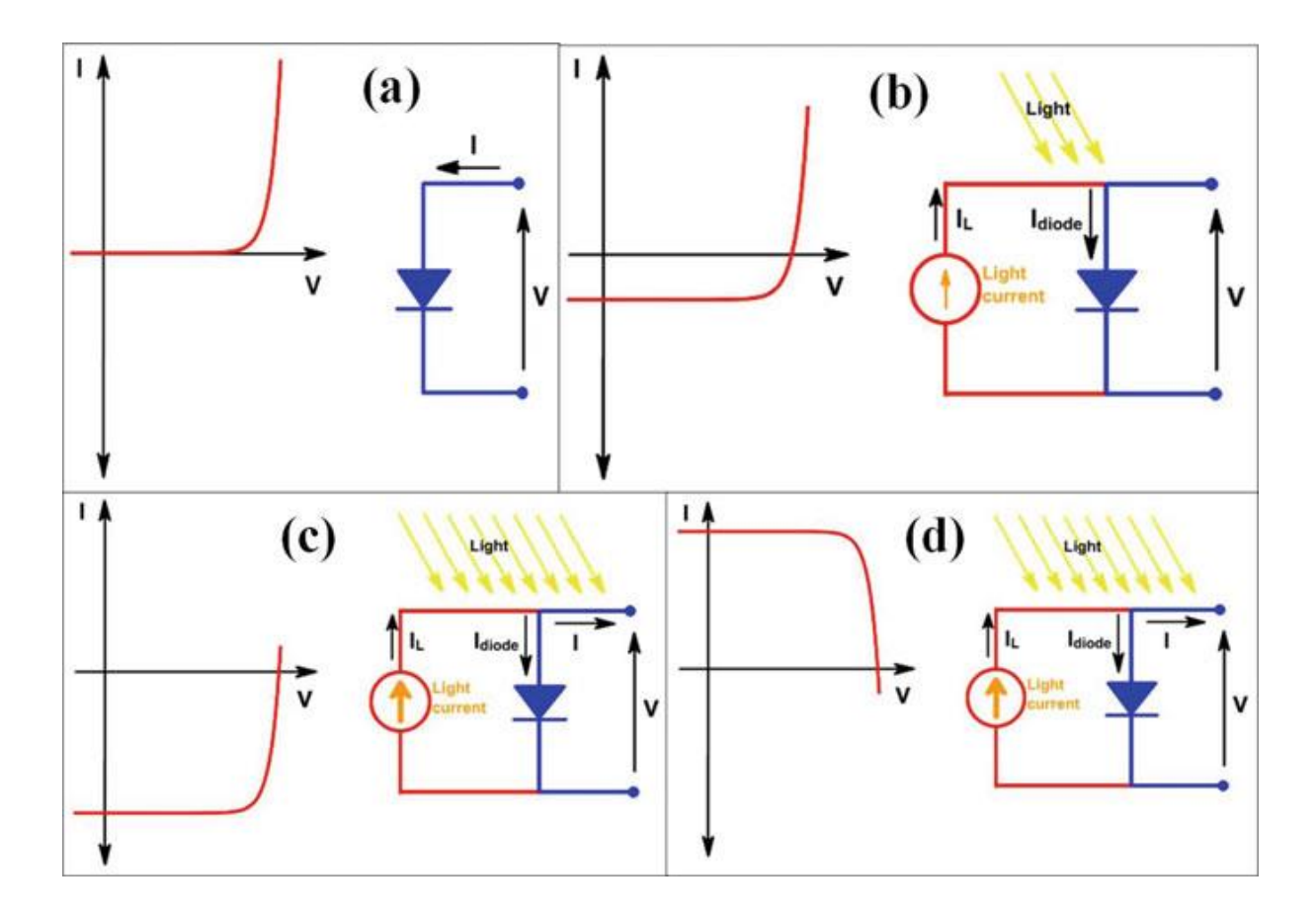


Figure I.4: I - V Curve of a solar cell: (a) without light; (b) when sunlight shines on the cell; (c) with greater light intensity; and (d) solar cell curve is flipped by convention [3, 4]

I.5 Parameters of a Solar Cell

I.5.1 Short-Circuit Current (I_{SC})

The current that flows through a solar cell when there is no voltage across the cell is called short-circuit current [10, 11]. In other terms, when solar cell is in short-circuit condition, the current that flows through the cell is called short-circuit current (I_{SC}). The creation and collection of light-generated carriers cause the flow of short-circuit current in a solar cell. The light-generated current (I_L) and short-circuit current for an ideal solar are identical. Therefore, the largest current that may be extracted from a solar cell is the short-circuit current. The short-circuit current depends on the following factors [4]:

• Solar cell area: The area of a solar cell strongly affects the short-circuit current. Hence, to remove this dependence, we mostly used short-circuit current density (J_{SC}) in place of short-circuit current. The unit of J_{SC} is mA/cm².

- Number of photons: I_{SC} from a solar cell is directly proportional to the intensity of light.
- Spectrum of the incident light: AM1.5 spectrum is considered as standard for solar cell measurements.

While comparing solar cells made from same material, the most important parameters are surface passivation and diffusion length. For a solar cell with uniform generation and perfect passivation, J_{SC} can be calculated as [4]:

$$J_{SC} = qG(L_n + L_p) (I.4)$$

where G is the rate of generation, and L_n and L_p are the diffusion length of electrons and holes, respectively. The relation between J_{SC} and I_{SC} is as follows:

$$J_{SC} = \frac{I_{SC}}{S} \tag{I.5}$$

Where $S(cm^2)$ is the cell area.

I.5.2 Open-Circuit Voltage (V_{OC})

The maximum voltage available at zero current in a solar cell is called open-circuit voltage (V_{OC}) . The V_{OC} in a solar cell depends upon the amount of forward bias applied to the cell [8, 11–14]. Using current equal to zero in the solar cell equation, the equation for V_{OC} is as follows:

$$V_{OC} = \frac{\eta k_B T}{q} \ln \left(\frac{I_L}{I_0} + 1 \right) \cong \frac{n k_B T}{q} \ln \left(\frac{I_L}{I_0} \right)$$
 (I.6)

From Eq.I.6, V_{OC} depends directly on the temperature, i.e., with increase in temperature, V_{OC} increases. However, in reality, the V_{OC} decreases with an increase in temperature and this is due to the fact that increase in temperature also increases the value of I_0 . The increase in I_0 with temperature is more rapid and as a result, the V_{OC} of a solar cell decreases with the temperature [4]. It is also evident that the V_{OC} depends on the value of η , the ideality factor of the diode. The value of η for an ideal diode is equal to unity ($\eta = 1.00$). But with current-transport dominated by recombination and generation (R&G), η value is equal to 2.00, indicating a helpful parameter to improve V_{OC} . But in real devices, I_L is drastically reduced and, hence, V_{OC} decreases [15].

I.5.3 Fill Factor (FF)

Fill factor (FF) determines the maximum power that can extracted from a solar cell. It depends upon V_{OC} and I_{SC} because at these two conditions, no power is generated from the solar cell [8, 11–14]. The fill factor (FF) is defined as the ratio of the maximum power (P_{max}) from the solar cell to the product of V_{OC} and I_{SC} and is given as:

$$FF = \frac{P_{max}}{V_{oc} I_{sc}} = \frac{P_{MP}}{V_{oc} I_{sc}} = \frac{V_{MP} I_{MP}}{V_{oc} I_{sc}}$$
(I.7)

Fill factor measures the "squareness" of solar cell and can also be calculated from the area of largest rectangle that can fit in the I-V curve of a solar cell. From Eq. I.7, the cell with larger V_{MP} will have higher value of FF [4].

I.5.4 Conversion Efficiency (E_{ff})

Conversion Efficiency of a solar cell is the ratio of energy output provided by the solar cell to the energy input taken for that output. However, the efficiency does not depend only on the energy input and output. It depends upon the temperature of solar cell, spectrum of the light, and intensity of the radiation. Hence, before calculating the efficiency, these parameters must be controlled [8, 11–14]. For example, for terrestrial solar cells, the efficiency is calculated at 25 °C temperature under AM1.5 conditions. Mathematically, the efficiency (E_{ff}) of a solar cell is the ratio of maximum power output to the power input:

$$E_{ff} = \frac{P_{max}}{P_{in}} = \frac{V_{MP} I_{MP}}{P_{in}} = \frac{V_{oc} I_{SC} FF}{P_{in}}$$
 (I.8)

When P_{in} is taken as the solar power incident on a unit area. The I_{SC} should be replaced by the current density (J_{SC}), giving

$$E_{ff} = \frac{V_{OC} J_{SC} FF}{P_{in}} \tag{I.9}$$

The standard AM1.5 condition provides the value of $P_{in} = 100 \text{ mW} cm^{-2}$ as the solar constant to evaluate the efficiency of the device.

I.5.5 Characteristic Resistance (R_{CH})

The output resistance of a solar cell at its MPP is called its characteristic resistance (R_{CH}). In other words, a solar cell operates at its MPP when its characteristic resistance (R_{CH}) is equal to the resistance of load (R_L) [3, 8, 10–14]. In order to understand the mechanism of parasitic loss in a solar cell, R_{CH} is an important parameter. The R_{CH} is equal to the inverse of slope of an I-V curve of a solar cell and is shown in Figure. I.5 [4].

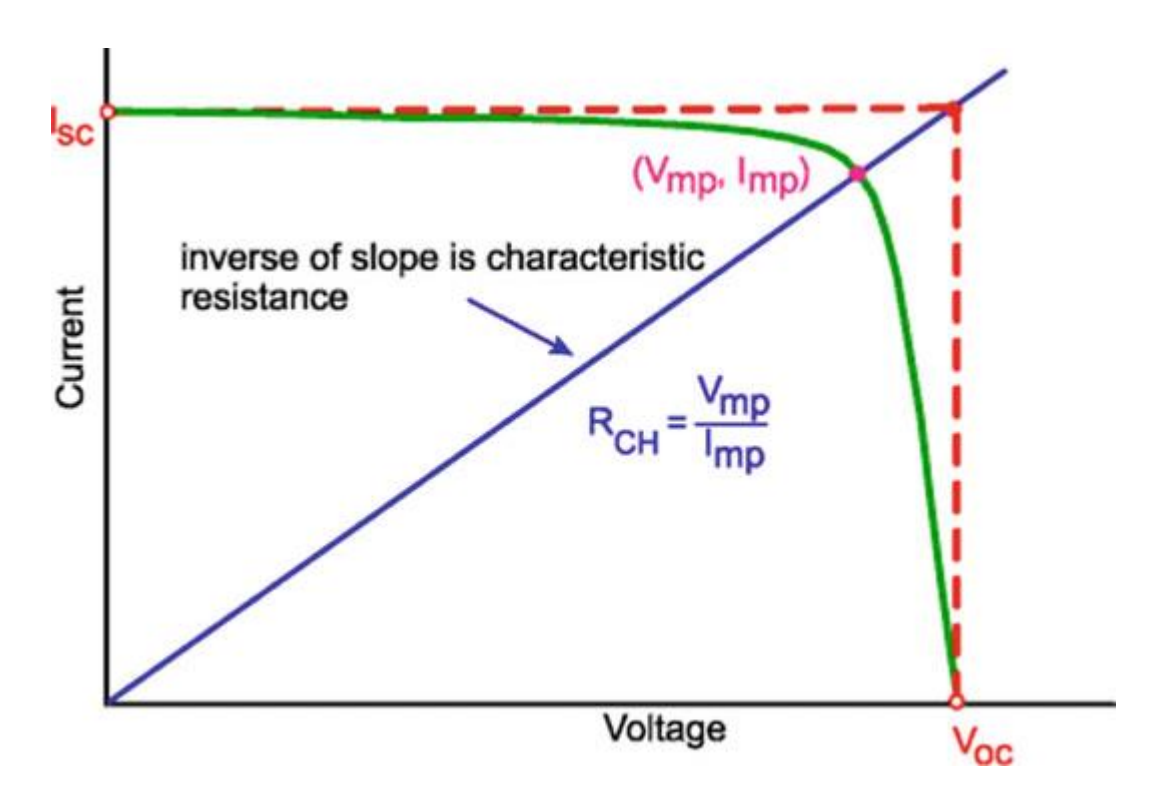


Figure I.5: Characteristic resistance of a solar cell [3, 4].

For most cells, R_{CH} is equal to [4]:

$$R_{CH} = \frac{V_{MP}}{I_{MP}} \approx \frac{V_{OC}}{I_{SC}} \tag{I.10}$$

Here, R_{CH} is expressed in Ω (ohms) when I_{MP} or I_{SC} is used, and it is expressed in Ω cm² (ohm cm²) when J_{MP} or J_{SC} is used [4].

I.5.6 Series (R_S) and Shunt (R_{SH}) Resistances

One of the characteristics of a solar cell that can be reduced but not entirely removed is series resistance (R_S). It mostly reduces the FF of a solar cell [8, 13, 14]. However, the high value of series resistance can also decrease the value of I_{SC} . The series resistance exists in a solar cell due to three main reasons: passage of current between base and emitter, resistance due to top and rear metal contacts, and resistance at contact between the semiconductor and metal [4].

Shunt resistance (R_{SH}) reduces the efficiency of a solar cell and causes significant power loss by providing an alternate path to the flow of current generated by light [8, 13, 14]. As a result, less current passes through the solar cell junction that reduces the output from the solar cell [4]. Figure I.6 represents the equivalent circuit diagram of a solar cell with series and shunt resistances.

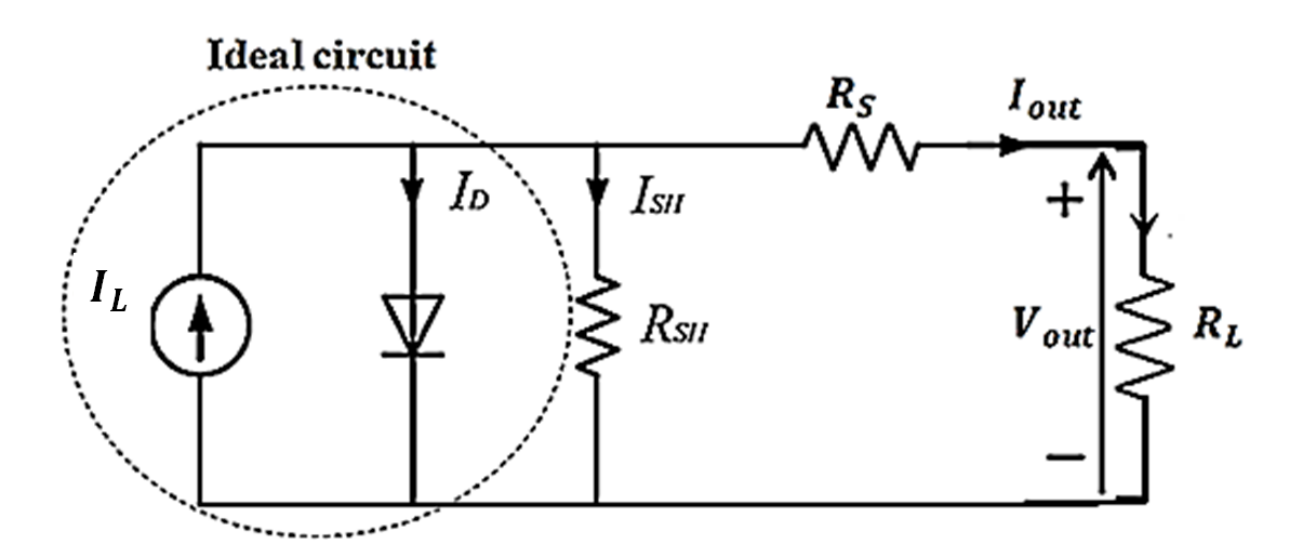


Figure I.6: A schematic diagram of the equivalent circuit of a solar cell.

The solar cell equation with series and shunt resistances is given as [15]:

$$I = I_L - \left[I_0\left(\exp\left(\frac{q(V + IR_S)}{\eta k_B T}\right) - 1\right) + \left(\frac{V + IR_S}{R_{Sh}}\right)\right] \cong I_{SC} - \left[I_0\left(\exp\left(\frac{q(V + IR_S)}{Ak_B T}\right) - 1\right) + \left(\frac{V + IR_S}{R_{Sh}}\right)\right]$$
(I.11)

I.5.7 Quantum Efficiency (QE)

Quantum efficiency (QE) is an important parameter to investigate the performance of a solar cell. The quantum efficiency of a solar cell can be defined as "the ratio of number of charge carriers collected by a solar cell to the number of photons of particular energy incident on it."

QE of a solar cell can be unity or we can say that a solar cell behaves as an ideal one when all the charge carriers produced by all the photons (of particular energy or wavelength) are collected in a solar cell [3, 16]. It is important to note that if the energy of a photons is less than the bandgap of the material, the quantum efficiency will always be zero. For an ideal solar cell, the gold square line shown in Figure I.7 represents the quantum efficiency [4].

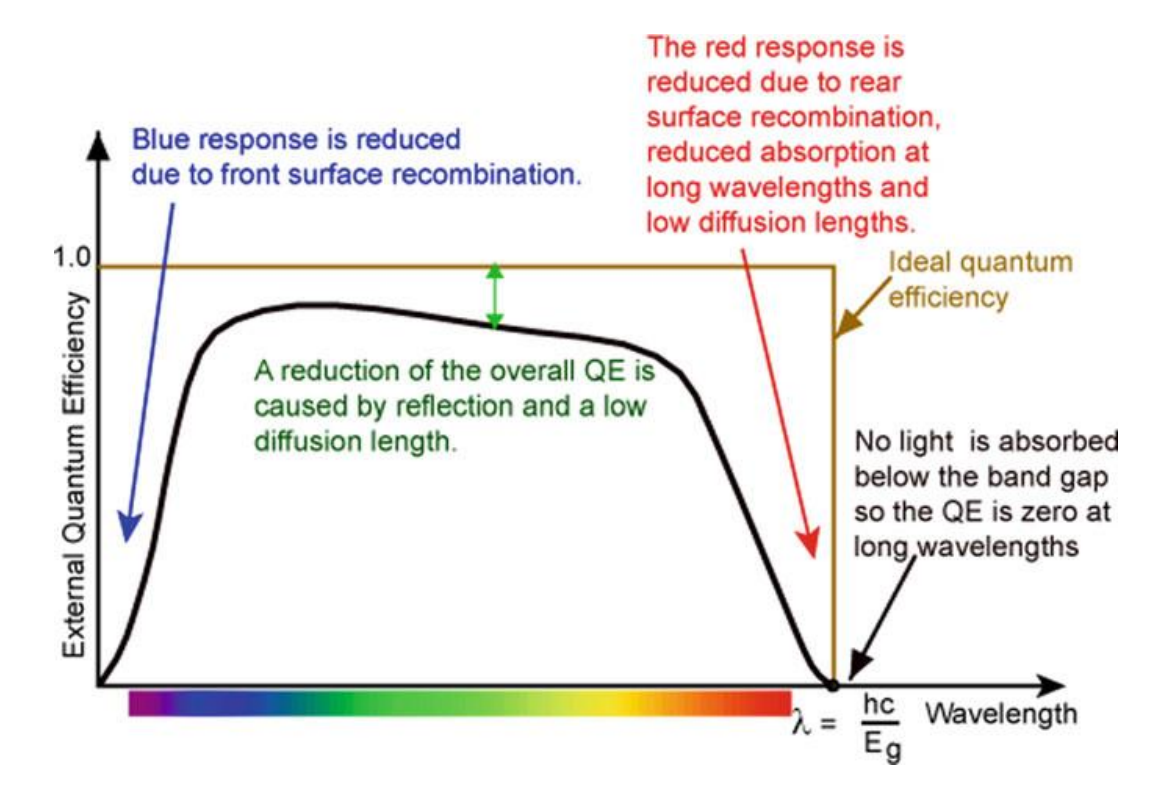


Figure I.7: Graphical representation of *QE* of a silicon solar cell [3, 4].

The entire light incident on a solar cell is not used for generating charge carriers. Some of the light is transmitted through the cell, and some part is reflected. Considering such optical loss of the energy, the quantum efficiency is further classified as external and internal quantum efficiency. The efficiency calculated after considering such optical losses is called external quantum efficiency (EQE). The internal quantum efficiency (IQE) is the quantum efficiency calculated for the photons that are neither reflected nor transmitted by the solar cell. Mostly, IQE is calculated for the solar cell. However, the EQE can be obtained from the IQE curve after measuring the transmission and reflection of the cell [4].

I.5.8 Spectral Response (SR)

Conceptually, the spectral response (SR) is very similar to the QE. However, the spectral response is the ratio of current produced by the solar cell to the power incident on the cell [17]. The choice of using SR or QE depends upon the application. The SR uses power of light at each wavelength, whereas QE uses number of photons incident on cell. The SR can be calculated from QE using equation [4]:

$$SR = \frac{q \lambda}{hc} QE \tag{I.12}$$

I.6 Solar Cells Generations

In the past decade, photovoltaics have become a major contributor to the ongoing energy transition. Advances relating to materials and manufacturing methods have had a significant role behind that development. However, there are still numerous challenges before photovoltaics can provide cleaner and low-cost energy. Research in this direction is focused on efficient photovoltaic devices such as multi-junction cells, graphene or intermediate band gap cells, and printable solar cell materials such as quantum dots [18, 19]. There are several technologies involved with the manufacturing process of photovoltaic cells, using material modification with different photoelectric conversion efficiencies in the cell components. Due to the emergence of many non-conventional manufacturing methods for fabricating functioning solar cells, photovoltaic technologies can be divided into four major generations, which is shown in Figure I.8 [19, 20]. The generations of various photovoltaic cells essentially tell the story of the stages of their past evolution. There are four main categories that are described as the generations of photovoltaic technology for the last few decades, since the invention of solar cells [21]:

- **First Generation:** This category includes photovoltaic cell technologies based on monocrystalline and polycrystalline silicon and gallium arsenide (GaAs).
- **Second Generation:** This generation includes the development of first-generation photovoltaic cell technology, as well as the development of thin film photovoltaic cell technology from "microcrystalline silicon (μ c-Si) and amorphous silicon (a-Si), copper indium gallium selenide (CIGS) and cadmium telluride/cadmium sulfide (CdTe/CdS) photovoltaic cells".

- Third Generation: This generation counts photovoltaic technologies that are based on more recent chemical compounds. In addition, technologies using nanocrystalline "films," quantum dots, dye-sensitized solar cells, solar cells based on organic polymers, multi-junction solar cells etc., also belong to this generation.
- **Fourth Generation:** This generation includes the low flexibility or low cost of thin film polymers along with the durability of "innovative inorganic nanostructures such as metal oxides and metal nanoparticles or organic-based nanomaterials such as graphene, carbon nanotubes and graphene derivatives" [21].

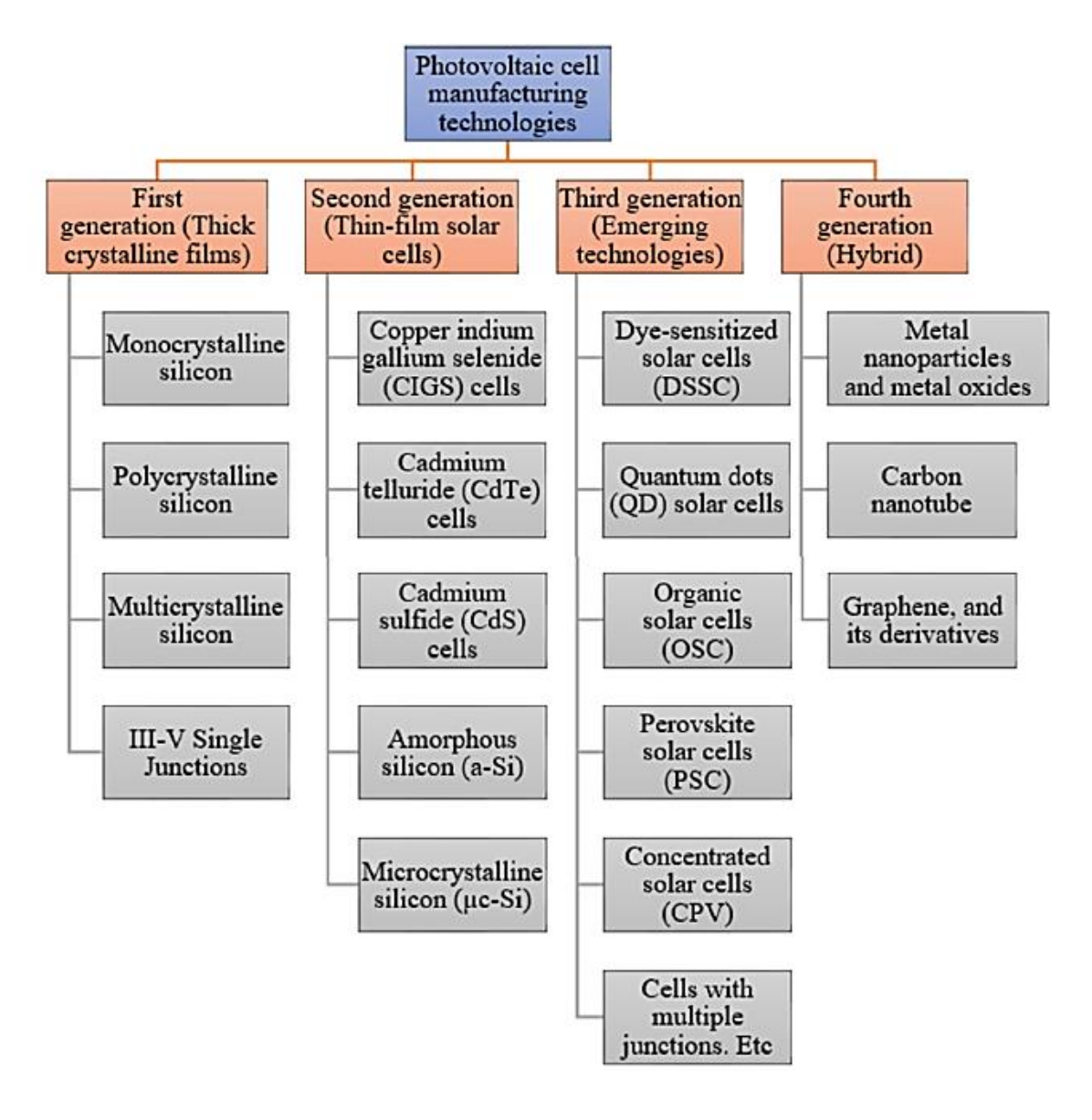


Figure I.8: Various solar cell types and current developments within this field [19, 22].

Examples of solar cell types for each generation along with average efficiencies are shown in Figure I.9 [19, 23].

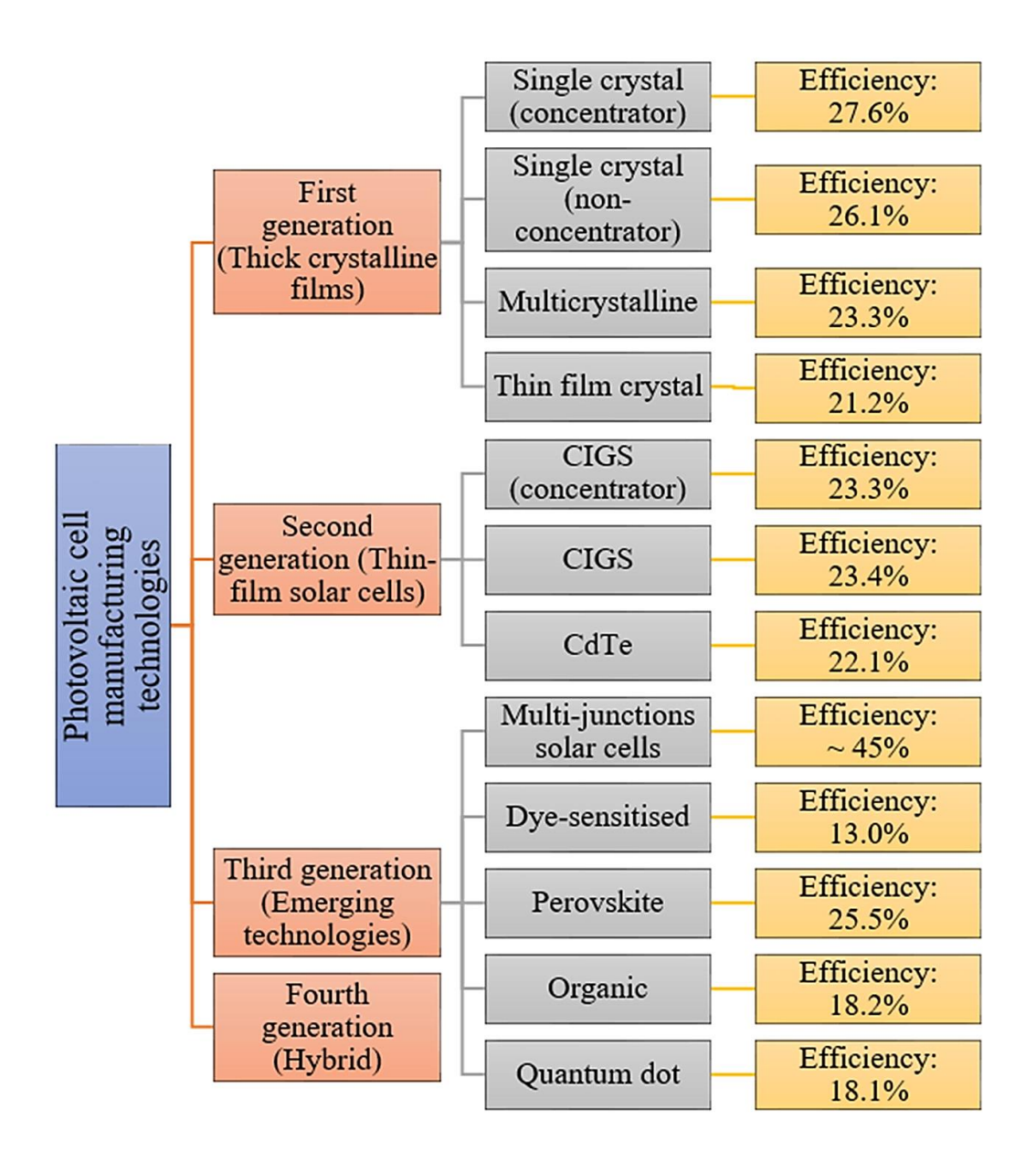


Figure I.9: Examples of photovoltaic cell efficiencies [19, 23].

I.6.1. First Generation of Photovoltaic Cells

Silicon-based PV cells were the first sector of photovoltaics to enter the market, using processing information and raw materials supplied by the industry of microelectronics. Solar cells based on silicon now comprise more than 80% of the world's installed capacity and have a 90% market share. Due to their relatively high efficiency, they are the most commonly used cells. The first generation of photovoltaic cells includes materials based on thick crystalline layers composed of Si silicon. This generation is based on mono-, poly-, and multicrystalline silicon, as well as single III-V junctions (GaAs) [19, 24, 25].

The III-V materials give the greatest photovoltaic conversion efficiency, achieving 29.1% with a GaAs single junction under single sunlight and 47.1% for a six-junction device under concentrated sunlight. These devices are also thinner (absorption layers typically being 2 to 5 μ m thick) and thus could be fabricated as lightweight, flexible devices capable of being placed on curved surfaces. The III-V devices have high stability and have a history of high performance for challenging applications such as space [19, 26].

Comparison of first-generation photovoltaic cells [19, 25]:

• Solar cells based on monocrystalline silicon (m-si)

Efficiency: 15 - 24%; Band gap: ~1.1 eV; Life span: 25 years; Advantages: Stability, high performance, long service life; Restrictions: High manufacturing cost, more temperature sensitivity, absorption problem, material loss.

• Solar cells based on polycrystalline silicon (p-si)

Efficiency: 10 - 18%; Band gap: ~1.7 eV; Life span: 14 years; Advantages: Manufacturing procedure is simple, profitable, decreases the waste of silicon, higher absorption compared to m-si; Restrictions: Lower efficiency, higher temperature sensitivity.

Solar cells based on GaAs

Efficiency: 28- 30%; Band gap: ~1.43 eV; Life span: 18 years; Advantages: High stability, lower temperature sensitivity, better absorption than m-si, high efficiency; Restrictions: Extremely expensive [25].

I.6.2 Second Generation of Photovoltaic Cells

The thin film photovoltaic cells based on CdTe, gallium selenide, and copper (CIGS) or amorphous silicon have been designed to be a lower-cost replacement for crystalline silicon solar cells. They offer improved mechanical properties that are ideal for flexible applications, but this comes with the risk of reduced efficiency. Whereas the first generation of solar cells was an example of microelectronics, the evolution of thin films required new methods of growing and opened the sector up to other areas, including electrochemistry [19, 27].

The second-generation photovoltaic cell comparison [19, 25]:

Solar cells based on amorphous silicon (a-si)

Efficiency: 5 - 12%; Band gap: ~1.7 eV; Life span: 15 years; Advantages: Less expensive, available in large quantities, non-toxic, high absorption coefficient; Restrictions: Lower efficiency, difficulty in selecting dopant materials, poor minority carrier lifetime.

Solar cells based on cadium telluride/cadium sulfide (CdTe/CdS)

Efficiency: 15 - 16%; Band gap: ~1.45 eV; Life span: 20 years; Advantages: High absorption rate, less material required for production; Restrictions: Lower efficiency, Cd being extremely toxic, Te being limited, more temperature-sensitive.

Solar cells based on copper indium gallium selenide (CIGS)

Efficiency: 20%; Band gap: ~1.7 eV; Life span: 12 years; Advantages: Less material required for production; Restrictions: Very high-priced, not stable, more temperature-sensitive, highly unreliable [25].

I.6.3 Third Generation of Photovoltaic Cells

The third generation of solar cells (including tandem, perovskite, dye-sensitized, organic, and emerging concepts) represent a wide range of approaches, from inexpensive low-efficiency systems (dye-sensitized, organic solar cells) to expensive high-efficiency systems (III-V multijunction cells) for applications that range from building integration to space applications. Third-generation photovoltaic cells are sometimes referred to as "emerging concepts" because of their poor market penetration, even though some of these have been studied for more than 25 years [19, 28].

The latest trends in silicon photovoltaic cell development are methods involving the generation of additional levels of energy in the semiconductor's band structure. The most advanced studies of manufacturing technology and efficiency improvements are now concentrated on third-generation solar cells. One of the current methods to increase the efficiency of PV cells is the introduction of additional energy levels in the semiconductor's band gap (IBSC: Intermediate Band Solar Cells and IPV: Impurity Photovoltaic cells) and the

Chapter I: Photovoltaic Solar Cells

increasing use of ion implantation in the manufacturing process. Other innovative third generation cells that are lesser-known commercial "emerging" technologies include [19, 29]:

- Organic materials (OSC) photovoltaic cells;
- Perovskites (PSC) photovoltaic cells;
- Dye-sensitized (DSSC) photovoltaic cells;
- Quantum dots (QD) photovoltaic cells; and
- Multi-junction photovoltaic cells [29].

Multi-junction (MJ) solar cells consist of plural p-n junctions fabricated from various semiconductor materials, with each junction producing an electric current in response to light of a different wavelength, thereby improving the conversion of incident sunlight into electricity and the efficiency of the device. The concept to use various materials with different band gaps has been suggested to utilize the maximum possible number of photons and is known as a tandem solar cell. An entire cell could be fabricated from the same or different materials, giving a broad spectrum of possible designs [30]. Usually, the cells are integrated monolithically and connected in series through a tunnel junction, and current matching between cells is obtained through adjusting each cell's band gap and thickness. Figure I.10 illustrates a scheme of an InGaP/(In)GaAs/Ge triple solar cell and presents crucial technologies to enhance efficiency of conversion [19, 30, 31].

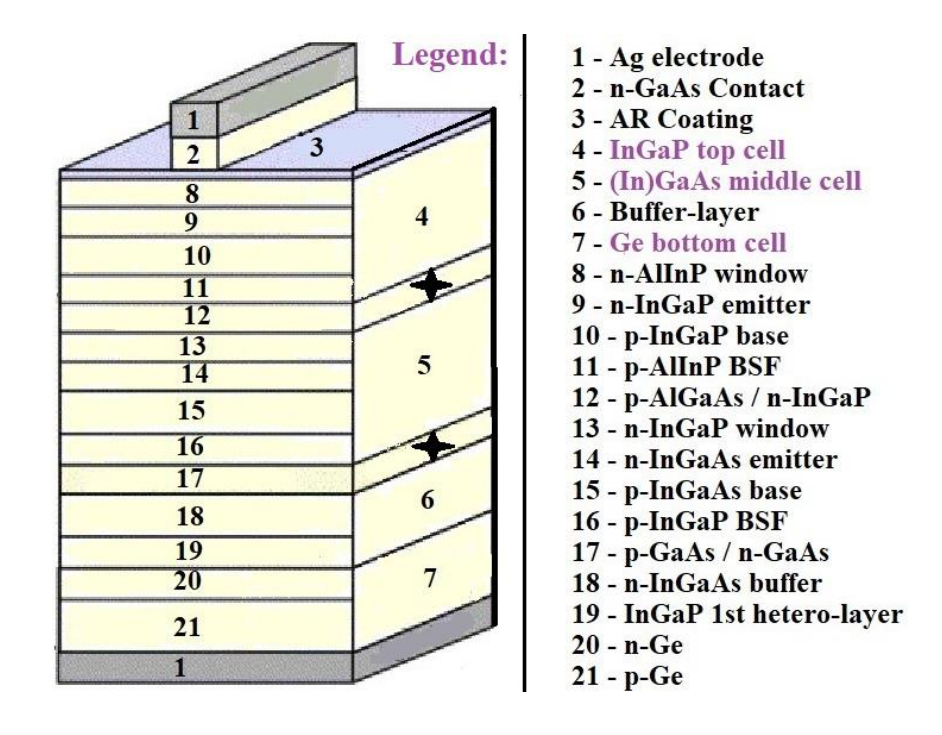


Figure I.10: Schematic illustration of a triple-junction cell and approaches for improving efficiency of the cell [19, 30, 31].

Third-generation photovoltaic cell comparison [19, 25]:

• Solar cells based on dye-sensitized photovoltaic cells

Efficiency: 5 - 20%; Advantages: Lower cost, low light and wider-angle operation, lower internal temperature operation, robustness, and extended lifetime; Restrictions: Problems with temperature stability, poisonous and volatile substances.

• Solar cells based on quantum dots

Efficiency: 11 - 17%; Advantages: Low production cost, low energy consumption; Restrictions: High toxicity in nature, degradation.

• Solar cells based on organic and polymeric photovoltaic cells

Efficiency: 9 - 11%; Advantages: Low processing cost, lighter weight, flexibility, thermal stability; Restrictions: Low efficiency.

• Solar cells based on perovskite

Efficiency: 21%; Advantages: Low-cost and simplified structure, light weight, flexibility, high efficiency, low manufacturing cost; Restrictions: Unstable.

• Multi-junction solar cells

Efficiency: 36% and higher; Advantages: High performance; Restrictions: Complex, expensive [25].

I.6.4 Fourth-generation of photovoltaic cells

Fourth-generation of photovoltaic cells are also known as hybrid inorganic cells because they combine the low cost and flexibility of polymer thin films, with the stability of organic nanostructures such as metal nanoparticles and metal oxides, carbon nanotubes, graphene, and their derivatives. These devices, often referred to as "nanophotovoltaics", could become the promising future of photovoltaics [32].

The technologies used for third- and fourth-generation cells are still in the prototyping stage. Production-scale prototypes have also been built and have been successful (10–17% efficiency). The third-generation multi-junction cells are already commercially available and have achieved exceptional conversion factors (from 40% to over 50%) that place this alternative as the best [19, 33].

I.7 Conclusion

This chapter has provided a comprehensive overview of photovoltaic solar cells, exploring their fundamental principles, operational mechanisms, and key performance parameters. The discussion began with an analysis of the solar spectrum, highlighting its impact on solar energy conversion. The role of the p-n junction diode in solar cell operation was examined, emphasizing charge carrier generation and transport under illumination. Essential photovoltaic parameters, including short-circuit current, open-circuit voltage, fill factor, and conversion efficiency, were detailed to illustrate the factors influencing solar cell performance. Additionally, the chapter reviewed the equivalent circuit model, series and shunt resistances, and quantum efficiency, all of which play crucial roles in optimizing solar cell operation.

Chapter I: Photovoltaic Solar Cells

Furthermore, advancements in photovoltaic technology were categorized into four generations, each representing significant progress in materials, efficiency, and manufacturing techniques. From first-generation crystalline silicon cells to the emerging fourth-generation hybrid and nanostructured materials, the evolution of solar cells continues to drive the development of more efficient and cost-effective energy solutions. Future advances aim to enhance efficiency, stability, and affordability, ensuring that solar energy becomes more accessible and widely adopted worldwide.

I.8 References

- [1] K. Zweibel, Harnessing Solar Power: The Photovoltaics Challenge, Springer US, Boston, MA, 1990. https://doi.org/10.1007/978-1-4899-6110-5.
- [2] A.S. Al-Ezzi, M.N.M. Ansari, Photovoltaic Solar Cells: A Review, Applied System Innovation 5 (2022) 67. https://doi.org/10.3390/asi5040067.
- [3] C.B. Honsberg, and S.G. Bowden, PV Education, (n.d.). https://www.pveducation.org/ (accessed February 6, 2025).
- [4] S. Arya, P. Mahajan, Solar Cells: Types and Applications, 1st ed. 2023 edition, Springer, Singapore, 2023. https://doi.org/10.1007/978-981-99-7333-0.
- [5] Y.-B. Hahn, T. Mahmoudi, Y. Wang, Next-Generation Solar Cells: Principles and Materials, Jenny Stanford Publishing, New York, 2023. https://doi.org/10.1201/9781003372387.
- [6] A. Kitai, Principles of Solar Cells, LEDs and Diodes: The role of the PN junction, 1st edition, Wiley-Blackwell, Chichester, 2011. http://dx.doi.org/10.1002/9781119974543
- [7] M.A. Green, Solar cells: operating principles, technology, and system applications, Prentice-Hall, Englewood Cliffs, NJ, 1982. https://www.scribd.com/document/706552586/Martin-a-Green-Solar-Cells-Operating-Principles-Technology-and-System-Applications-Prentice-Hall-1982
- [8] T. Markvart, L. Castañer, Chapter I-1-A Principles of Solar Cell Operation, in: S.A. Kalogirou (Ed.), McEvoy's Handbook of Photovoltaics (Third Edition), Academic Press, 2018: pp. 3–28. https://doi.org/10.1016/B978-0-12-809921-6.00001-X.
- [9] E.T. Hahsim, A.A. Abbood, Temperature Effect on Power Drop of Different Photovoltaic Modules, Journal of Engineering 22 (2016) 129–143. https://doi.org/10.31026/j.eng.2016.05.09.
- [10] K. Keshavani, J. Joshi, V. Trivedi, M. Bhavsar, Modelling and Simulation of Photovoltaic Array Using Matlab/Simulink, in: International Journal of Engineering Development and Research, 2014: pp. 3742–3751. https://www.semanticscholar.org/paper/Modelling-and-

- Simulation-of-Photovoltaic-Array-Keshavani-Ioshi/3284f89806d2d4758083edaefc8ba91478cb5dd3
- [11] S.J. Fonash, Solar Cell Device Physics, Elsevier, 2012. https://books.google.dz/books/about/Solar_Cell_Device_Physics.html?id=mqOJ_ijx2FM C&redir_esc=y.
- [12] R.C. Neville, Solar Energy Conversion: The Solar Cell, 2nd edition, Elsevier Science, Amsterdam; New York, 1995. https://www.amazon.com/Solar-Energy-Conversion-Cell/dp/0444898182.
- [13] J.L. Gray, The Physics of the Solar Cell, in: A. Luque, S. Hegedus (Eds.), Handbook of Photovoltaic Science and Engineering, 1st ed., Wiley, 2010: pp. 82–129. https://doi.org/10.1002/9780470974704.ch3.
- [14] L.M. Fraas, L.D. Partain, Solar cells and their applications, John Wiley & Sons, 2010. https://books.google.com/books?hl=en&lr=&id=ds7vnCgmSnMC&oi=fnd&pg=PP14&dq=info:pyTVoSwt1AEJ:scholar.google.com&ots=d-1z-GpxUf&sig=DzP5PcYRh-k4mszP3gTj6oX03a8 (accessed February 9, 2025).
- [15] I.M. Dharmadasa, Advances in Thin-Film Solar Cells, 2nd ed., Jenny Stanford Publishing, New York, 2018. https://doi.org/10.1201/9780429020841.
- [16] A. Fahrenbruch, R. Bube, Fundamentals Of Solar Cells: Photovoltaic Solar Energy Conversion, Academic Press, 2012. https://doi.org/10.1115/1.3267632.
- [17] B. Dale, F.P. Smith, Spectral Response of Solar Cells, Journal of Applied Physics 32 (1961) 1377–1381. https://doi.org/10.1063/1.1736237.
- [18] L. Tsakalakos, Nanotechnology for Photovoltaics, CRC Press, Boca Raton, 2010. https://doi.org/10.1201/9781420076752.
- [19] J. Pastuszak, P. Węgierek, Photovoltaic Cell Generations and Current Research Directions for Their Development, Materials 15 (2022) 5542. https://doi.org/10.3390/ma15165542.

- [20] S. Almosni, A. Delamarre, Z. Jehl, D. Suchet, L. Cojocaru, M. Giteau, B. Behaghel, A. Julian, C. Ibrahim, L. Tatry, H. Wang, T. Kubo, S. Uchida, H. Segawa, N. Miyashita, R. Tamaki, Y. Shoji, K. Yoshida, N. Ahsan, K. Watanabe, T. Inoue, M. Sugiyama, Y. Nakano, T. Hamamura, T. Toupance, C. Olivier, S. Chambon, L. Vignau, C. Geffroy, E. Cloutet, G. Hadziioannou, N. Cavassilas, P. Rale, A. Cattoni, S. Collin, F. Gibelli, M. Paire, L. Lombez, D. Aureau, M. Bouttemy, A. Etcheberry, Y. Okada, J.-F. Guillemoles, Material challenges for solar cells in the twenty-first century: directions in emerging technologies, Sci Technol Adv Mater 19 (2018) 336–369. https://doi.org/10.1080/14686996.2018.1433439.
- [21] A. Luque, S. Hegedus, Handbook of Photovoltaic Science and Engineering, 2nd ed, John Wiley & Sons, 2011. https://www.wiley.com/en-us/Handbook+of+Photovoltaic+Science+and+Engineering%2C+2nd+Edition-p-9780470721698.
- [22] M.V. Dambhare, B. Butey, S.V. Moharil, Solar photovoltaic technology: A review of different types of solar cells and its future trends, J. Phys.: Conf. Ser. 1913 (2021) 012053. https://doi.org/10.1088/1742-6596/1913/1/012053.
- [23] R.A. Marques Lameirinhas, J.P.N. Torres, J.P. de Melo Cunha, A Photovoltaic Technology Review: History, Fundamentals and Applications, Energies 15 (2022) 1823. https://doi.org/10.3390/en15051823.
- [24] A. Richter, M. Hermle, S.W. Glunz, Reassessment of the Limiting Efficiency for Crystalline Silicon Solar Cells, IEEE Journal of Photovoltaics 3 (2013) 1184–1191. https://doi.org/10.1109/JPHOTOV.2013.2270351.
- [25] Suman, P. Sharma, P. Goyal, Evolution of PV technology from conventional to nanomaterials, Materials Today: Proceedings 28 (2020) 1593–1597. https://doi.org/10.1016/j.matpr.2020.04.846.
- [26] S. Ghosh, R. Yadav, Future of photovoltaic technologies: A comprehensive review, Sustainable Energy Technologies and Assessments 47 (2021) 101410. https://doi.org/10.1016/j.seta.2021.101410.

- [27] A. Kuczyńska-Łażewska, E. Klugmann-Radziemska, A. Witkowska, Recovery of Valuable Materials and Methods for Their Management When Recycling Thin-Film CdTe Photovoltaic Modules, Materials 14 (2021) 7836. https://doi.org/10.3390/ma14247836.
- [28] W.A. Dunlap-Shohl, Y. Zhou, N.P. Padture, D.B. Mitzi, Synthetic Approaches for Halide Perovskite Thin Films, Chem Rev 119 (2019) 3193–3295. https://doi.org/10.1021/acs.chemrev.8b00318.
- [29] P. Peumans, A. Yakimov, S.R. Forrest, Small molecular weight organic thin-film photodetectors and solar cells, Journal of Applied Physics 93 (2003) 3693–3723. https://doi.org/10.1063/1.1534621.
- [30] M. Yamaguchi, T. Takamoto, K. Araki, N. Ekins-Daukes, Multi-junction III-V solar cells: current status and future potential, Solar Energy 79 (2005) 78–85. https://doi.org/10.1016/j.solener.2004.09.018.
- [31] H. Gao, R. Yang, Y. Zhang, Improving Radiation Resistance of GaInP/GaInAs/Ge Triple-Junction Solar Cells Using GaInP Back-Surface Field in the Middle Subcell, Materials 13 (2020) 1958. https://doi.org/10.3390/ma13081958.
- [32] C. Wu, K. Wang, M. Batmunkh, A.S.R. Bati, D. Yang, Y. Jiang, Y. Hou, J.G. Shapter, S. Priya, Multifunctional nanostructured materials for next generation photovoltaics, Nano Energy 70 (2020) 104480. https://doi.org/10.1016/j.nanoen.2020.104480.
- [33] N. Kant, P. Singh, Review of next generation photovoltaic solar cell technology and comparative materialistic development, Materials Today: Proceedings 56 (2022) 3460–3470. https://doi.org/10.1016/j.matpr.2021.11.116

Chapter II GaInP/GaAs Solar Cells

II.1 Introduction

Solar energy represents one of the most promising alternatives to traditional fossil fuels, driven by the urgent need for sustainable and renewable energy sources. Among the various photovoltaic technologies, GaInP/GaAs (Gallium Indium Phosphide/Gallium Arsenide) solar cells have emerged as a leading candidate for high-efficiency applications due to their exceptional performance characteristics. These cells are part of a class of multi-junction solar cells, where GaInP/GaAs forms the top two layers of a tandem cell structure, optimizing the absorption of the solar spectrum and significantly enhancing energy conversion efficiency.

The GaInP/GaAs tandem cell structure takes advantage of the distinct electronic properties of each semiconductor material. GaInP, with its direct bandgap of approximately 1.8-1.9 eV, absorbs high-energy photons, while GaAs, with a bandgap of about 1.42 eV, captures lower-energy photons that pass through the GaInP layer. This arrangement maximizes the spectrum of light absorbed and converted into electricity, leading to higher overall efficiencies compared to single-junction cells.

Through both numerical simulations and experimental work, several significant advancements have been made in the conversion efficiencies of GaInP/GaAs solar cells. For example, high-efficiency GaInP single-junction solar cells achieved 23.73% efficiency as reported by the work of H Charane et al. [1]. Quantum well-enhanced GaInP/GaAs cells reported efficiencies of 32.9% by integrating strain-balanced GaInAs/GaAsP quantum wells, marking a new record for tandem solar cells [2]. Improved GaInP/GaAs tandem solar cells with enhanced efficiency were developed, achieving a simulated efficiency around 30% [3], [4]. Further advancements in quantum well technology for GaInP/GaAs cells have shown simulated efficiencies exceeding 33% under standard conditions [5]. Further theoretical predictions indicate potential efficiencies up to 35.15% as reported by Kharchich et al. [6], and up to 43.55% as reported by the work of Sabri et al. [7]. These advancements highlight the ongoing improvements in material science and cell architecture that continue to push the boundaries of solar cell efficiency. GaInP/GaAs solar cells represent a pinnacle of photovoltaic technology, combining high efficiency with robust performance. As research and development continue to advance, these cells are controlled to play a crucial role in the future of solar energy, both on Earth and beyond.

This chapter explores the foundational principles, materials, and recent advancements that underline the capabilities of GaInP/GaAs solar cells, emphasizing their role in the future of renewable energy technologies.

II.2 Overview of III-V Compound Semiconductors for Photovoltaics and High-Efficiency Solar Cells

III-V compound semiconductors, composed of elements from groups III and V of the periodic table (Figure II.1), are vital for photovoltaics and high-efficiency solar cells due to their superior electronic and optical properties. Materials such as Gallium Arsenide (GaAs), Indium Phosphide (InP), Gallium Indium Phosphide (GaInP), Gallium Nitride (GaN), Indium Gallium Arsenide (InGaAs), and Indium Gallium Nitride (InGaN) are particularly renowned for their unique electronic characteristics and their use in high-performance optoelectronic devices. These compounds typically include elements like gallium (Ga), indium (In), phosphorus (P), and arsenic (As), among others, which contribute to their exceptional performance in these applications [8-13].

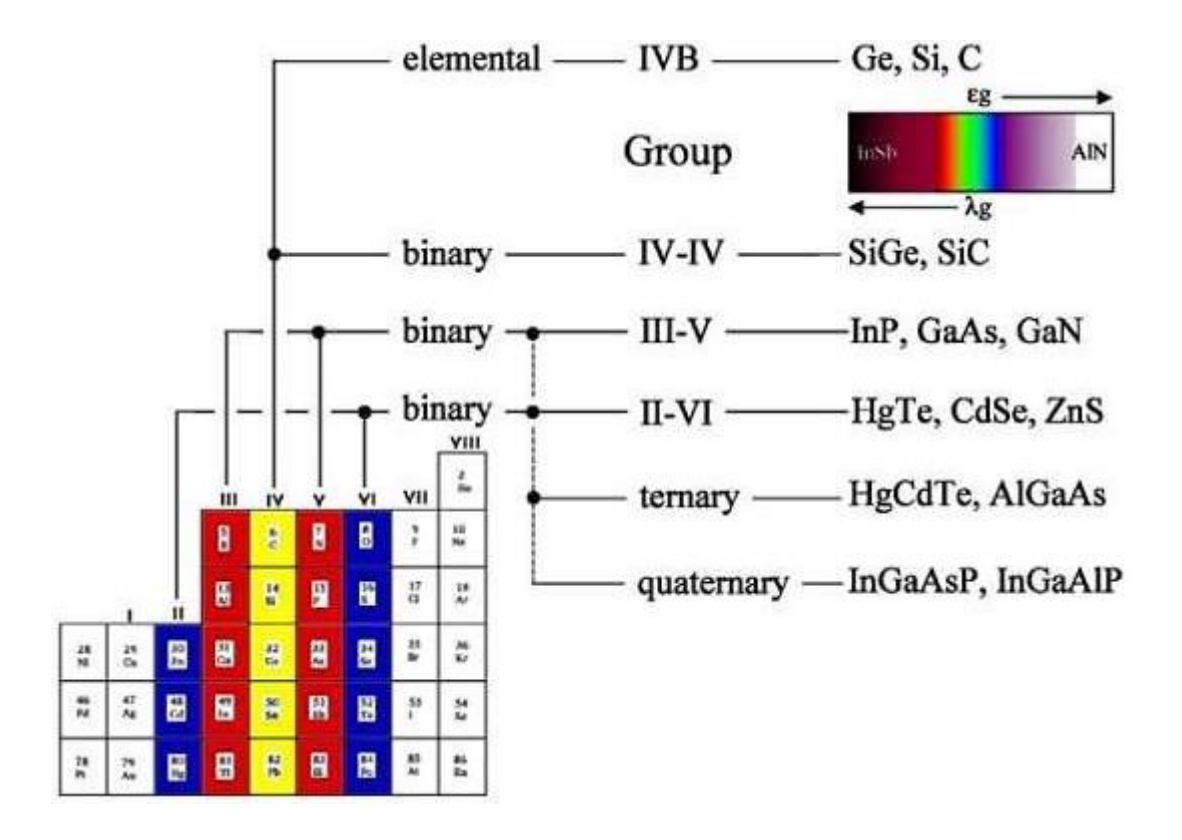


Figure II.1: Diagram illustrating various compound semiconductors [14].

III-V compound semiconductors, such as Gallium Arsenide (GaAs) and Indium Phosphide (InP), are well-known for their direct bandgaps, high absorption coefficients, and high electron mobility. These properties make them highly efficient in absorbing and emitting light, leading to better photon absorption and electron-hole pair generation, which is crucial for high-performance solar cells. The high absorption coefficients of these materials allow for effective sunlight absorption in thin layers, reducing material usage and manufacturing costs. Additionally, their high electron mobility enhances electrical conductivity and overall solar cell efficiency [8,15-19].

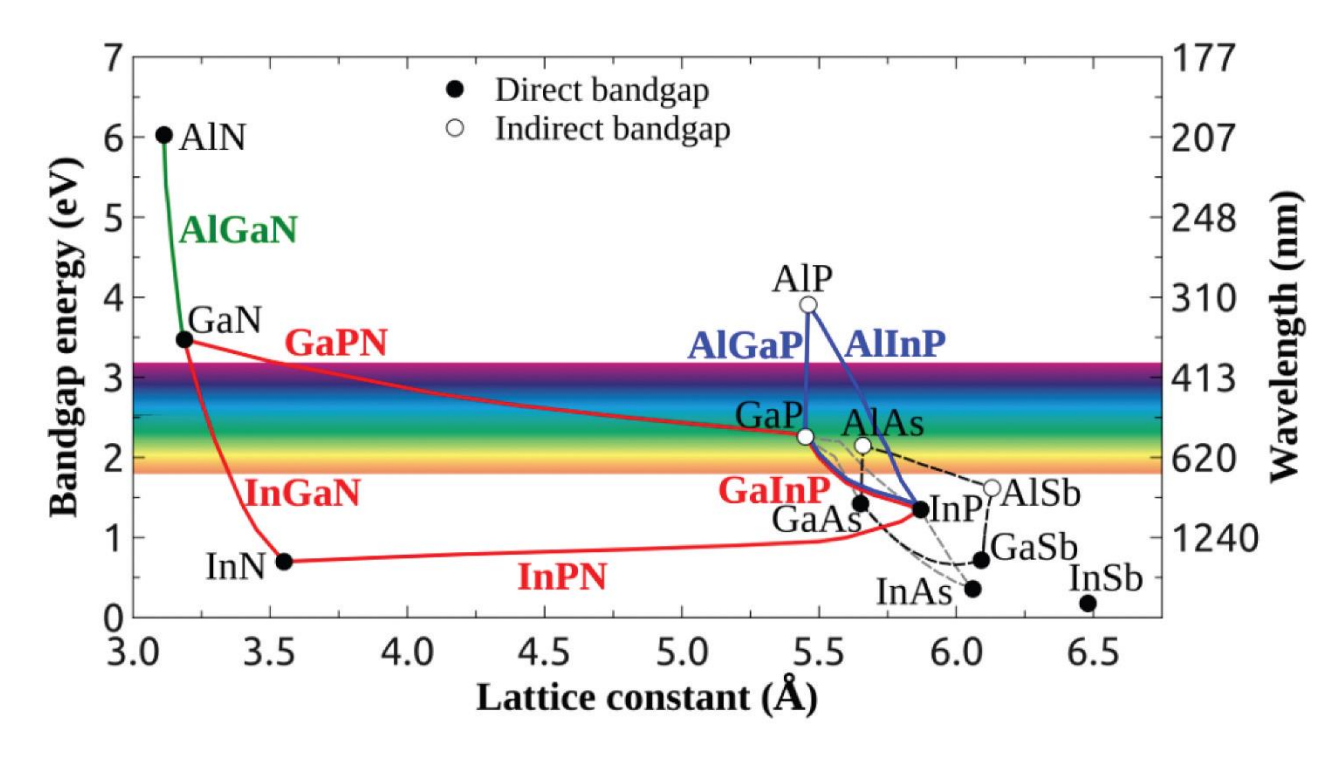


Figure II.2. Bandgap energy as a function of lattice constant for different III-V materials [19].

III–V semiconductors can be binary, ternary, or quaternary alloys, formed by two, three, or four chemical elements, respectively. The concentration of pairs of elements in ternary or quaternary alloys can be varied to adjust the bandgap energy and optical properties, such as the refractive index and absorption coefficient. In Figure II.2, we present the bandgap energy as a function of the lattice constant for various III–V compounds. The wavelength equivalent of the bandgap energy is displayed on the right vertical axis. Binary compounds are represented in the graph by dots. The lines connecting two dots represent ternary compounds formed from the corresponding binary compounds. The areas subtended by the lines of the same color represent quaternary compounds formed from the four binaries (red for InGaPN, blue for AlGaInP, black

for AlGaAsSb and grey for InGaAsP). The mutual concentrations of binaries in a ternary alloy provide a degree of freedom that can be varied to modify the alloy's optical properties. The concentration dependence can be schematically represented as $A_xB_{1-x}C$ where A, B, and C are single elements from the groups III and V of the periodic table, and x is the content or fraction of the element A. In this regard, quaternary alloys have two degrees of freedom, and therefore provide more flexibility in achieving desired optical properties. They can be represented as $A_xB_{1-x}C_yD_{1-y}$. Vegard's law provides a description of the desired bandgap energy, parameterized by the relative concentration of the III–V elements:

$$E_g(A_x B_{1-x}C) = x E_g(AC) + (1-x) E_g(BC)$$
 (II.1)

where E_g corresponds to the bandgap energy and A, B, and C are the III-V single elements [20,21].

Other material properties, like the refractive index, can also be calculated by this law. However, for some compositions or properties, a quadratic dependence on the concentration parameter x, known as the bowing parameter, is required [20]. In a similar way, Vegard's law for a quaternary compound takes the form [23]:

$$E_{g}(A_{x}B_{1-x}C_{y}D_{1-y}) = xyE_{g}(AC) + x(1-y)E_{g}(AD) + (1-x)yE_{g}(BC) + (1-x)(1-y)E_{\sigma}(BD).$$
(II.2)

Epitaxial growth of III–V semiconductors provides high-quality films having low defect density, which is crucial for quantum and nonlinear photonic applications [23].

The ternary and quaternary alloys can be grown on binary substrates or on a previously grown epitaxial layer (epilayer). However, the lattice constant of the new layer must be matched to the previous one. Lattice mismatch leads to structural imperfections in the epilayers, which can act as recombination and scattering centers. The presence of such defects can result in significant scattering losses, hampering the integrated optical device's performance [19].

If the two materials lie on the same vertical line on the graphic of Figure II.2, they can be grown lattice-matched. $Al_xGa_{1-x}As$, for instance, can be grown lattice-matched on GaAs with all possible concentrations of aluminium. Substrates also play a crucial role in epitaxial growth. If the substrate is the same as the growth material, the growth is called homoepitaxy. Conversely, if the growth material is different from the substrate, the growth is referred to as heteroepitaxy [24]. The presence of defects in heteroepitaxial growth from lattice and thermal mismatches

presents a significant challenge. Therefore, buffer layers are often used to optimize the growth of high-quality heteroepitaxial thin films [24].

Various epitaxial growth techniques are utilized for III-V semiconductors, such as molecular beam epitaxy (MBE) [25], metal-organic chemical vapor deposition (MOCVD) [26], and liquid phase epitaxy (LPE) [24]. MBE has a thickness precision at the angstrom level. A molecular beam is focused at a heated substrate and deposits atom-by-atom under controlled growth dynamics. It is capable of growing sharp interfaces and is widely used for electronic and optical devices. However, this growth technique is very costly and offers a slow growth rate, which limits its applicability and availability. MOCVD provides several advantages in this aspect. In particular, MOCVD provides a faster growth rate and lower cost. MOCVD is a chemical vapor deposition technique, which uses a flow of a gas-phase mixture containing precursors over a heated substrate for layer-by-layer deposition. This technique is capable of depositing a controlled thin layer with higher wafer throughput. It is widely used for integrated circuit applications. Finally, LPE is a low-cost deposition technique, which deposits material from a supersaturated solution. However, it is not capable of forming sharp junctions between two material layers. More recently, other cost-effective, large-area, and faster growth techniques have been explored for III-V semiconductors such as hybrid vapor phase epitaxy (HVPE) [27], close-spaced vapor transport (CSVT) [28], and thin-film vapor-liquidsolid (TF-VLS) growth [29,30]. The ongoing development of these techniques provides a pathway towards the commercialization of a cost-effective approach for III-V semiconductors for photonics [19].

In photovoltaics, III-V semiconductors are pivotal in multi-junction solar cells, which layer different semiconductors to capture a broad spectrum of solar energy, achieving efficiencies over 40% in labs. They are also preferred in space applications for their efficiency and radiation resistance, and in concentrated photovoltaics (CPV), where sunlight is concentrated onto a small, high-efficiency cell to reduce costs. Advances included the development of materials like Gallium Nitride (GaN) and Indium Gallium Nitride (InGaN), which offer tunable bandgaps and potential for third-generation solar cells, along with high-throughput manufacturing processes like metal-organic chemical vapor deposition (MOCVD) and molecular beam epitaxy (MBE). Future directions focus on reducing manufacturing costs, enhancing durability and stability under real-world conditions, and integrating III-V semiconductors with emerging technologies like perovskites and organic photovoltaics to create hybrid solar cells with unprecedented efficiencies [31-34].

II.3 Gallium Arsenide and Gallium Indium Phosphide for photovoltaics and high-efficiency solar cells

Both GaAs and GaInP offer distinct advantages over silicon (Si) in solar cell applications, primarily due to their efficient absorption of a broader range of solar spectrum wavelengths. This characteristic is crucial for achieving high conversion efficiencies, especially under concentrated sunlight conditions [35,36].

II.3.1 Gallium Arsenide (GaAs): is a typical III-V semiconductor material, composed of gallium and arsenic atoms in a 1:1 ratio, forming a zinc blende crystalline structure. GaAs has a direct bandgap of about 1.42 eV at room temperature, ideal for solar cells as it efficiently absorbs sunlight with a thinner layer compared to indirect bandgap materials like silicon. Its high electron mobility (about 8500 cm²/V·s) enables efficient charge carrier transport, while its thermal stability and radiation resistance make it suitable for space and high-temperature applications. GaAs can be used in thin-film solar cells, which are lightweight and flexible, beneficial for aerospace and portable devices. The advantages of GaAs in photovoltaics include higher efficiency, thin-film capability, durability in harsh environments, and its potential in multi-junction cells. GaAs is also suitable for applications in high-speed electronic devices and lasers. Among all types of single junction solar cells, GaAs solar cells experimentally demonstrate the highest power conversion efficiency and approach the Shockley-Queisser (SQ) limit (Figure II.3) [37, 38].

The GaAs single-junction solar cells have achieved a record conversion over 28%. More precisely, Alta Devices Inc. has reported a certified world record efficiency of 28.8% for single junction GaAs solar cells under AM1.5G illumination [37, 38]. The multi-junction GaAs solar cells exhibited conversion efficiencies exceeding 40%. Despite its higher cost and toxicity concerns, GaAs remains a key material in advanced solar technologies and space applications due to its efficiency, durability, and resistance to extreme conditions. [40,41]

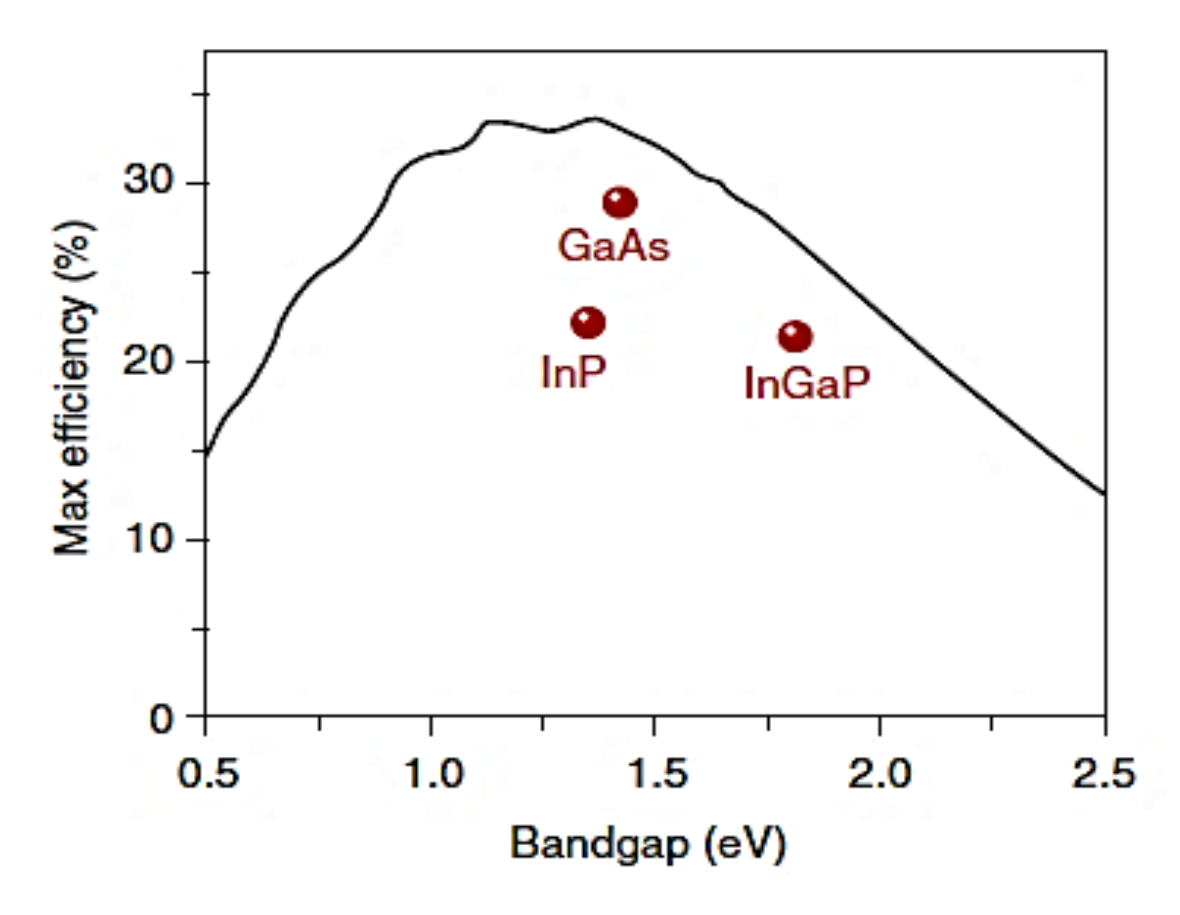


Figure II.3 Theoretical Shockley–Queisser (SQ) detailed balance efficiency limit as a function of bandgap for single junction solar cells under AM1.5G illumination [39]. The points represent the record efficiencies for the typical III–V cells including GaAs, InP, and InGaP [37, 38].

II.3.2 Indium Phosphide: Crystalline indium phosphide (InP) is another important III-V compound semiconductor for photovoltaic (PV) devices, whose bandgap of 1.35 eV lies close to the optimum for single junction solar cells. Even though the current efficiency of InP solar cells is less than that demonstrated for GaAs ones due to their lower open-circuit voltages and fill factors, they still offer a suitable option for both space and terrestrial PV applications, especially for the multijunction (MJ) solar system. In addition, the inherently high resistance of InP to radiation damage gives it a special advantage for space applications compared to GaAs or silicon materials [42]. There has been significant interest in the development of InP solar cell technology for several years after the discovery of its high radiation resistance during the middle 1980s [43]. Nowadays, an efficiency of 24.2% has been reported for a 1 cm² InP cell fabricated and measured at the US National Renewable Energy Laboratory (NREL) [44, 37].

II.3.3 Gallium Indium Phosphide (GaInP): Indium gallium phosphide $(In_xGa_{1-x}P; 0 < x < 1)$, a pseudo-binary III-V alloy with tunable band gaps in the range of 1.3-2.3 eV and strong visible light absorption, is a promising material for high efficiency solar cells [45], [46], [47]. Over the past few decades, many studies have been focused on exploring and enhancing the photovoltaic performance of $In_xGa_{1-x}P$ -based solar cells. The reported photoelectric conversion efficiencies (PCEs) of InGaP-based single-junction cells are around 21% [48] or 23.73% as reported by the work of H Charane et al. [1]. Double-junction cells based on $In_{0.65}Ga_{0.35}P$ and $In_{0.49}Ga_{0.51}P$ have been reported with PCE of 25.5% and over 30%, respectively [49,50]. For InGaP-based triple-junction cells, the reported PCEs can be even higher than 40% [49,50]. Considering the rich chemical compositions of $In_xGa_{1-x}P$ alloys, it is possible to optimize the photovoltaic performance by the tuning of compositions [50]. In general, $In_xGa_{1-x}P$ alloys could be crystallized in zinc blende (ZB) or wurtzite (WT) structure; and it could be also easily formed in disordered structures [50].

The bandgap of GaInP, particularly at a composition of Ga_{0.5}In_{0.5}P with a value around 1.9 eV, is optimal for top cells in multi-junction solar cells, enabling efficient absorption of the visible spectrum of sunlight. GaInP is frequently used alongside other III-V materials like Gallium Arsenide (GaAs) in these cells, achieving efficiencies exceeding 40% under concentrated sunlight conditions [51-54]. Its direct bandgap makes it ideal for LEDs and laser diodes, especially in the red and yellow wavelengths, while its high electron mobility enhances performance in high-speed, high-frequency devices. The precise control of Ga and In composition during growth processes like Metal-Organic Chemical Vapor Deposition (MOCVD) and Molecular Beam Epitaxy (MBE) allows fine-tuning of its properties for specific applications. Efforts to integrate GaInP with other semiconductors, especially silicon, aim to combine its superior optoelectronic properties with the cost-effectiveness and scalability of silicon-based technologies. Challenges such as lattice mismatch with other materials like GaAs and silicon can introduce defects that impact performance, but advances in growth techniques and buffer layers help mitigate these issues. Ongoing research focuses on improving the efficiency and stability of GaInP-based devices, with future advancements to expand its application in next-generation solar cells, particularly in perovskite tandem solar cells, through several developments [55-61].

II.4 Multi-Junction Solar Cells

II.4.1 Single Junction Solar Cells:

According to the Shockley-Queisser (SQ) theory [39], the limiting PV energy conversion efficiency for a single junction solar cell is 33.7% with an optimum semiconductor bandgap of 1.34 eV. The previous Figure II.3 shows the maximum theoretical efficiency of the single p-n junction solar cell with different bandgap materials and some of the record efficiencies under the standard AM1.5G solar spectrum illumination [38, 39]. In order to approach the thermodynamic efficiency limits, solar cells should employ perfect semiconducting materials, as well as ideal electronic and optical structures to capture as many photons as possible and effectively convert them into free carriers that can generate electricity [37, 62].

II.4.2 InGaP/GaAs Double Junction Solar Cells

As shown in Figure II.4 (a), single junction solar cells can only have a maximum work condition when absorbing a certain wavelength of photons, the energy of which is equal to the bandgap ($h\nu = E_g$)[37]. For incident light with a photon energy higher than the cell bandgap $(hv > E_a)$, only part of the photon energy can be converted to electrical energy and the remaining excess energy $(h\nu - E_a)$ is wasted as thermalization loss. On the other hand, photons with energies lower than the bandgap ($hv < E_g$) cannot be absorbed and converted into electricity. Since photovoltaic (PV) cells are operated under broadband solar irradiation with photons at wavelengths from ultraviolet to infrared (300-1700 nm), such thermalization loss and sub-bandgap transparency result in low efficiencies in single junction solar cells. To overcome this obstacle of energy loss in solar cells, multi-junction PV structures that comprise sub-cells with different bandgaps are developed [37]. Figure II.4 (b) schematically presents the operation principal of a typical multi-junction solar cell, in which the broadband sunlight penetrates into multiple cells, with high-energy photons being absorbed by the top cells with large bandgaps and low-energy photons absorbed by the corresponding lower cells with small bandgaps. Conventional multi-junction solar cells are formed by epitaxial growth methods, with each subcell being electrically connected in series. To obtain MJ solar cells with ideal efficiencies, issues including lattice matching and current matching among the subcell junctions are to be considered [37]. Double junction (2J) AlGaAs/GaAs solar cells were first developed in early days, and efficiencies less than 20.2% were achieved due to low performance and unstable tunnel

junctions, and the defects related to the oxygen in the AlGaAs materials [63]. Thus, a tandem combination of InGaP material for the top cell with GaAs cell in the bottom was proposed by Olson et al. [64]. With the improved performance on the tunnel junction between the subcells and top cell of the InGaP layer in the epitaxial growth process, Takamoto et al. achieved InGaP/GaAs tandem cells with an efficiency over 30% under AM1.5G illumination [65, 66]. In 2013, Alta Device Inc. reported a 30.8% efficiency 2J InGaP/GaAs solar cell [67]. In the same year, NREL achieved a new record of 31.1% under AM1.5G illumination with improved voltage in the bottom cell, mainly due to the enhanced photon recycling effect with a gold back mirror contact [68].

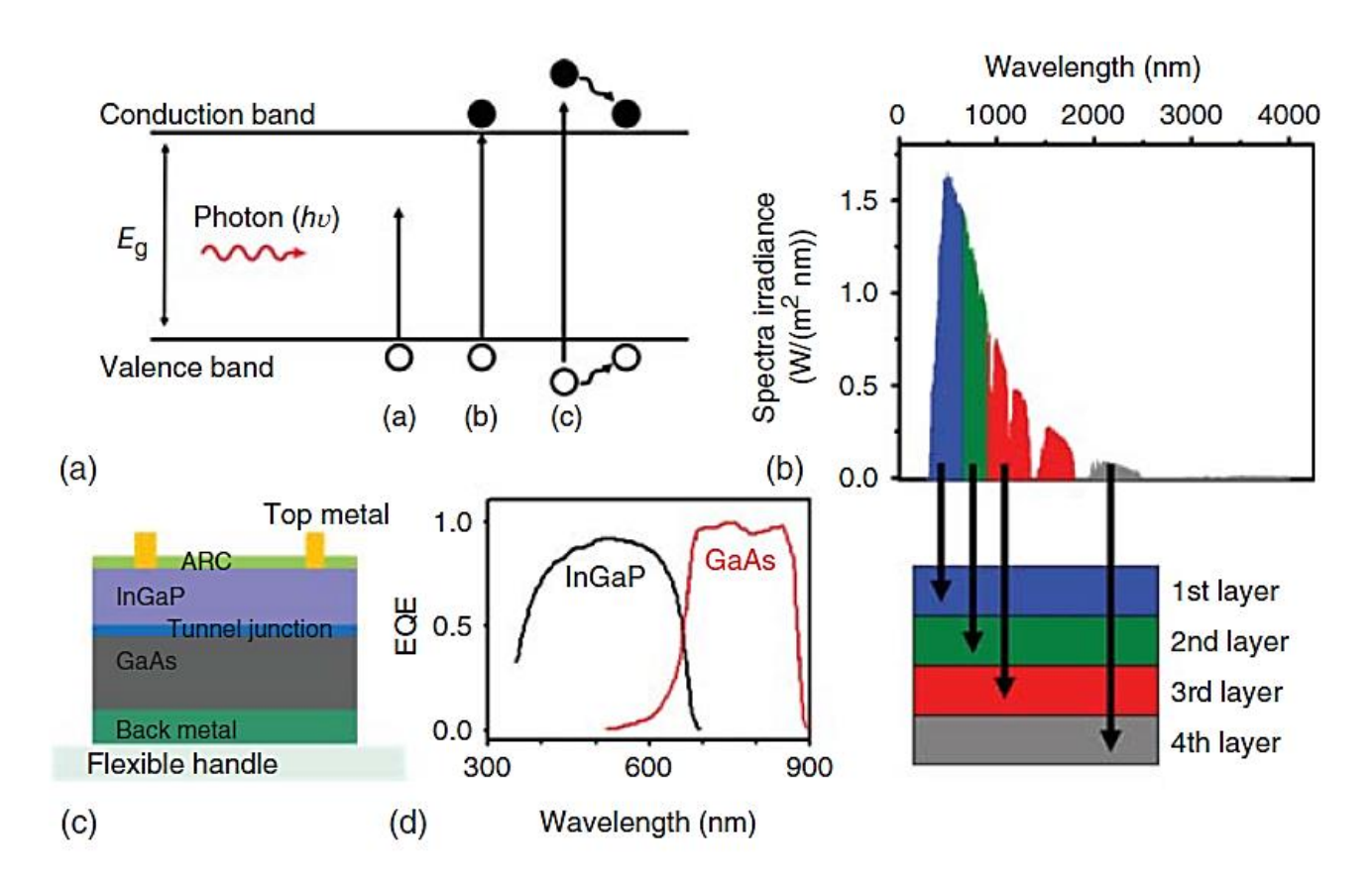


Figure II.4 (a) Schematic illustration of the electron-hole pairs generation process in the bandgap material (E_g) excited by light photons with different energies (hv). (b) Schematic illustration of the absorption of solar spectrum for each subcell in multijunction (MJ) solar cells. (c) Schematic illustration of flexible InGaP/GaAs tandem solar cells, (d) and the corresponding EQE spectrum of each subcell [37].

Recent works in both simulation and experimental studies have reported impressive conversion efficiencies for GaInP/GaAs dual junction solar cells. One notable advance is the development

of a tandem solar cell with strain-balanced GaInAs/GaAsP quantum wells, which demonstrated a record efficiency of **32.9%** under one-sun illumination [69]. Another significant contribution of Makambo. et al. presented a numerical simulation of a dual-junction tandem GaInP/GaAs cell, achieving an efficiency of **36.86%** under AM 1.5 G solar spectrum [70]. The research highlighted the importance of optimizing the top GaInP layer thickness and current matching between the top and bottom cells to achieve these high efficiencies.

The external quantum efficiency (EQE) spectra of each subcell in a typical InGaP/GaAs cell are shown in Figure II.4 (d), indicating the fraction of the incident light of given wavelengths that are converted into electricity [68]. Furthermore, the InGaP/GaAs cells have great potential for future space applications and have shown superior radiation-resistant properties in comparison to single junction solar cells [71]. The 2J solar cells serve as a starter for MJ cell research, and then triple, quadruple, and even more than four junction (4J)-based cells have been designed to further make the best use of the entire solar spectrum. With the development of material properties and advanced concept designs, efficiency record-breaking has been occurring continuously recently, with an absolute efficiency increase of about 1% each year [72], [37].

II.5. Bandgap Engineering in GaInP/GaAs Solar Cells

Bandgap engineering is a critical technique in optimizing the performance of GaInP/GaAs solar cells. By precisely tuning the bandgap of the materials, researchers can maximize the absorption of the solar spectrum, leading to higher conversion efficiencies. GaInP, with its adjustable bandgap, can be optimized to absorb higher-energy photons, while GaAs absorbs lower-energy photons, ensuring efficient use of the solar spectrum. Figure II.5 illustrates the layered structure of a GaInP/GaAs tandem solar cell. The diagram shows several key components that are vital for the cell's efficiency [73]:

- Anti-Reflective Coating (ARC): The top layer is a ZnS/MgF₂ anti-reflective coating,
 which minimizes reflection losses and enhances light absorption.
- **Top Contact**: Above the ARC is the Au top contact, which facilitates efficient current collection.
- **n**⁺ **GaAs Contact**: This layer ensures effective electron flow from the cell.

- **n**⁺ **GaInP Emitter and p GaInP Base**: These layers form the first junction, optimized for high-energy photon absorption. The bandgap of GaInP is personalised to maximize the absorption of photons with energies greater than 1.9 eV.
- Tunneling Interconnect: This connects the two sub-cells and allows for efficient charge carrier transport.
- **p**⁺ **GaInP Back Surface Field (BSF)**: Enhances carrier collection by reducing recombination at the rear surface.
- n⁺ GaInP Window and p GaAs Base: These layers form the second junction, optimized for lower-energy photon absorption. The GaAs bandgap is around 1.42 eV, which is ideal for absorbing the remaining lower-energy photons.
- **p**⁺ **GaInP Emitter and Au Back Contact**: Ensures efficient hole collection and minimal recombination losses.

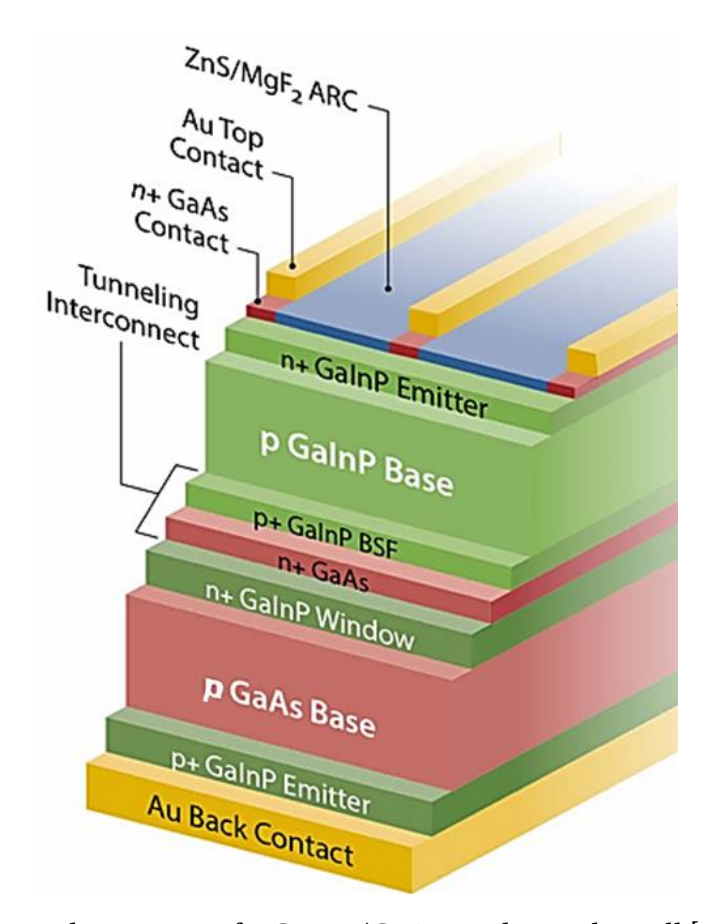


Figure II.5: The layered structure of a GaInP/GaAs tandem solar cell [73]

Recent advancements in growth techniques, such as metamorphic and lattice-matched structures, have enabled the integration of GaInP and GaAs layers with minimal defects [73]. This precise engineering minimizes lattice mismatch, which could otherwise introduce

dislocations and defects that degrade performance. Techniques like hydride vapor phase epitaxy (HVPE) have been instrumental in achieving high-quality layers. These advancements have led to the development of high-efficiency multijunction cells that can achieve efficiencies exceeding 30% under concentrated sunlight. The intricate layering and precise engineering of these materials are key to achieving such high performance with the complex design of tandem solar cells [73].

Carrier transport mechanisms in this tandem solar cell (**Figure II.5**) involve the generation, separation, and collection of electron-hole pairs. When sunlight enters the cell, it first passes through the ZnS/MgF_2 anti-reflective coating (ARC), which minimizes reflection losses and enhances light absorption. Photons are absorbed in the n^+ -GaInP emitter and p-GaInP base, generating electron-hole pairs. The built-in electric field at the n-p junction of the GaInP layers drives electrons towards the n^+ GaInP emitter and holes towards the p GaInP base. The tunneling interconnect facilitates the transfer of carriers between the GaInP and GaAs sub-cells. In the GaAs sub-cell, photons are absorbed in the n^+ -GaInP window and p- GaAs base, generating additional electron-hole pairs. The electric field at the GaAs n-p junction drives electrons towards the n^+ GaInP window and holes towards the p^+ GaInP emitter. Finally, the electrons and holes are collected at the Au top contact and Au back contact, respectively, generating a current. The tandem structure allows for the absorption of a broader spectrum of sunlight, enhancing the overall efficiency of the solar cell [74, 75].

II.6 Multi-junction approach

The multi-junction approach involves directing incident photons onto a junction tuned to the photon's energy. The simplest approach is to use an optically dispersive element like a prism to distribute photons with different energies to different locations. However, the approach illustrated in Figure II.6 (a) is often undesirable due to its mechanical and optical complexities. A more preferable approach is to arrange cells in a stacked configuration; as illustrated in Figure II.6 (b), with sunlight hitting the highest band gap first, and then going to the progressively lower band gap junctions. This arrangement avoids the need for a separate optical element and can be mechanically assembled into a compact package called a mechanical stack [76].

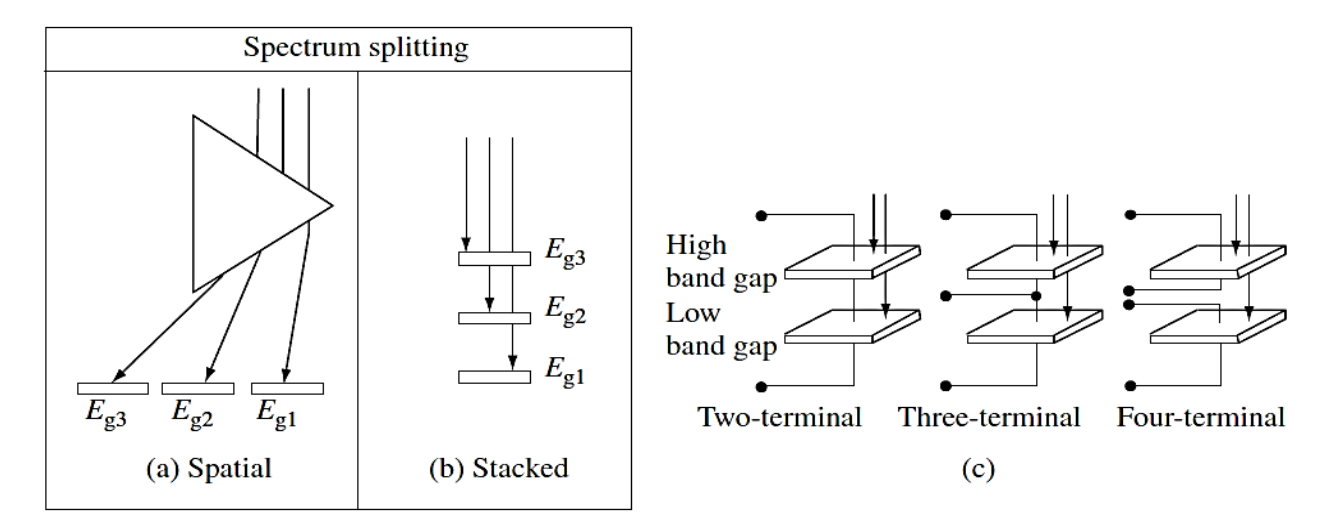


Figure II.6: Schematic comparison of (a) spatial-configuration approaches and (b) stacked configuration approaches to distributing light to subcells of different band gaps. (c) Illustration of two-, three-, and four-terminal connection to a two-junction cell. The figure shows the subcells as mechanically separate, but the two- and three-terminal devices can be monolithic [76].

Consequently, the sunlight strikes the highest band gap first, and then goes to the progressively lower band gap junctions. This arrangement makes use of the fact that junctions act as low-pass photon energy filters, transmitting only the sub-band gap light. Thus, in Figure II.6 (b), photons with $hv > E_{g3}$ get absorbed by that junction, photons with $E_{g2} < hv < E_{g3}$ get absorbed by the E_{g2} junction, and so on; in other words, the junctions themselves act as optical elements to distribute the spectrum to the appropriate junctions for multijunction photoconversion. The band gaps must decrease from top to bottom of the stack. The stacked configuration requires, of course, that all the junctions in the stack except the bottom one be transparent to light below their band gaps [76].

These configurations, which provide for varying degrees of electrical isolation of the subcells, are illustrated in Figure II.6 (c) for a two-junction stack. The two-terminal series-connected configuration provides the most restrictions for interconnection of the devices. This configuration requires that the subcells be of the same polarity and that the photocurrents of the subcells be closely matched, since in this series connection the subcell with the least photocurrent limits the current generated by the entire device [76]. In the three-terminal configuration the subcells are not electrically isolated; the bottom of each cell is electrically

connected to the top of the cell beneath it. The fabrication of a monolithic three-terminal device is relatively straightforward, although more complex than the fabrication of a two-terminal device. The semiconductor structure must be designed to provide a layer for contact to the intermediate terminal, and to accommodate the processing steps necessary to put the intermediate terminal in place. With this intermediate terminal, the different subcells in the stack do not have to have the same photocurrents. Furthermore, in this three-terminal configuration, the different subcells in the stack may have different polarities, for example, p/n for the top cell and n/p for the bottom cell [76]. In the four-terminal configuration, each subcell has its own two terminals and is electrically isolated from the other subcells. This configuration has the advantage that it sets no constraints on the polarities (p/n vs. n/p) of the subcells, or on their currents or voltages. However, the terminals and the electrical isolation between subcells in the four-terminal configuration would be very difficult to accomplish monolithically, because it requires a complicated cell structure and processing [76].

Since the sub-cells are series-connected in the two-terminal multi-junction solar cell, the overall current I_{MJSC} is limited by the sub-cell that photo-generates the lowest current according to Eq. II.3 for a two-junction stack (tandem or double junction):

$$I_{MJSC} = Min (I_{Top}, I_{Bottom})$$
 (II.3)

On the other part, the multi-junction voltage is the sum of all sub-cells voltages minus the voltage of the tunnel diode because they are in reverse bias (see Eq. II.4) [77].

$$V_{MJSC} = \sum_{i} V_{i} - \sum_{Tunnel\ diode} = V_{top} + V_{Bottom} - (V_{TD})$$
 (II.4)

One of the advantages of this configuration, is the low photo-generated current (compared to single junction) hence the reduced series resistance effects especially at high light intensity levels [77].

II.7 Conclusion

Solar energy has emerged as a foundation for sustainable development, offering a clean and renewable alternative to fossil fuels. Among the cutting-edge advancements in photovoltaic technology, GaInP/GaAs (Gallium Indium Phosphide/Gallium Arsenide) solar cells stand out for their exceptional energy conversion efficiencies. These cells leverage the unique electronic and optical properties of III-V semiconductors to optimize the absorption of the solar spectrum. The tandem structure of GaInP/GaAs solar cells integrates materials with complementary bandgaps—GaInP for high-energy photons and GaAs for lower-energy photons—thereby

Chapter II: GaInP/GaAs Solar Cells

capturing a broad range of sunlight. Recent innovations, including strain-balanced quantum wells and advanced epitaxial growth techniques, have pushed the efficiency of these cells to record-breaking levels, making them pivotal in high-performance terrestrial and space applications. Through a combination of advanced material engineering and optimized cell architectures, these devices demonstrate not only high performance under standard conditions but also robustness in extreme environments, paving the way for their integration into next-generation solar technologies such as hybrid and multi-junction systems. This chapter explored the foundational principles, materials, and recent advancements that underline the capabilities of these solar cells, emphasizing their role in the future of renewable energy technologies.

II.8 References:

- [1] H. Charane, A. Mahrane, A. Mesrane, H. Mazouz, Study and simulation of GaInP single junction solar cell, Eng. Res. Express 6 (2024) 015076. https://doi.org/10.1088/2631-8695/ad2244.
- [2] M.A. Steiner, R.M. France, J. Buencuerpo, J.F. Geisz, M.P. Nielsen, A. Pusch, W.J. Olavarria, M. Young, N.J. Ekins-Daukes, 32.9% efficient tandem solar cell with strain-balanced GaInAs/GaAsP quantum wells, in: 2021 IEEE 48th Photovoltaic Specialists Conference (PVSC), 2021: pp. 1084–1085. https://doi.org/10.1109/PVSC43889.2021.9518819.
- [3] A. Bakour, A. Saadoune, I. Bouchama, F. Dhiabi, S. Boudour, M.A. Saeed, Effect and optimization of ZnO layer on the performance of GaInP/GaAs tandem solar cell, Micro and Nanostructures 168 (2022) 207294. https://doi.org/10.1016/j.micrna.2022.207294.
- [4] G.S. Sahoo, G.P. Mishra, Design and modeling of an efficient metamorphic dual-junction InGaP/GaAs solar cell, Opt Quant Electron 48 (2016) 420. https://doi.org/10.1007/s11082-016-0691-y.
- [5] M. Steiner, III-V PV Cell Core Capability (Final Technical Report), 2023. https://doi.org/10.2172/1959068.
- [6] F.Z. Kharchich, A. Khamlichi, Optimizing efficiency of InGaP/GaAs dual-junction solar cells with double tunnel junction and bottom back surface field layers, Optik 272 (2023) 170196. https://doi.org/10.1016/j.ijleo.2022.170196.
- [7] S. Sabri, R. Malek, K. Kassmi, Improvement Efficiency of Solar Cells Using III-V Dual Junction: InGap/GaAs, Key Engineering Materials 954 (2023) 97–109. https://doi.org/10.4028/p-Xlwk3B.
- [8] K. Tanabe, A Review of Ultrahigh Efficiency III-V Semiconductor Compound Solar Cells: Multijunction Tandem, Lower Dimensional, Photonic Up/Down Conversion and Plasmonic Nanometallic Structures, Energies 2 (2009) 504–530. https://doi.org/10.3390/en20300504.

- [9] J. Li, A. Aierken, Y. Liu, Y. Zhuang, X. Yang, J.H. Mo, R.K. Fan, Q.Y. Chen, S.Y. Zhang, Y.M. Huang, Q. Zhang, A Brief Review of High Efficiency III-V Solar Cells for Space Application, Front. Phys. 8 (2021). https://doi.org/10.3389/fphy.2020.631925.
- [10] R. Hasan, A.A. Navid, P. Banerjee, J. Kadir, Design and Performance of InGaAs/GaAs Based Tandem Solar Cells, American Journal of Engineering Research (2016). https://doi.org/10.1007/978-981-33-4909-4_19
- [11] F. Chancerel, P. Regreny, J.L. Leclercq, M. Volatier, A. Jaouad, M. Darnon, S. Fafard, M. Gendry, V. Aimez, Comparison of the performances of various InGaAs-based solar cells for concentrated photovoltaic applications, (2020). https://hal.science/hal-02991192 (accessed December 28, 2024).
- [12] L. Zhu, Y. Wang, X. Pan, H. Akiyama, Theoretical modeling and ultra-thin design for multi-junction solar cells with a light-trapping front surface and its application to InGaP/GaAs/InGaAs 3-junction, Opt. Express, OE 30 (2022) 35202–35218. https://doi.org/10.1364/OE.466168.
- [13] M. Yamaguchi, High-Efficiency GaAs-Based Solar Cells, in: M. Muzibur Rahman, A. Mohammed Asiri, A. Khan, Inamuddin, T. Tabbakh (Eds.), IntechOpen, 2021. https://doi.org/10.5772/intechopen.94365.
- [14] A. Owens, A. Peacock, Compound semiconductor radiation detectors, Nuclear Instruments and Methods in Physics Research Section A: Accelerators, Spectrometers, Detectors and Associated Equipment 531 (2004) 18–37. https://doi.org/10.1016/j.nima.2004.05.071.
- [15] T.S. Kim, H.J. Kim, D.-M. Geum, J.-H. Han, I.S. Kim, N. Hong, G.H. Ryu, J. Kang, W.J. Choi, K.J. Yu, Ultra-Lightweight, Flexible InGaP/GaAs Tandem Solar Cells with a Dual-Function Encapsulation Layer, ACS Appl Mater Interfaces 13 (2021) 13248–13253. https://doi.org/10.1021/acsami.1c00006.
- [16] A. Kowsar, S.C. Debnath, M. Shafayet-Ul-Islam, M.J. Hossain, M. Hossain, A.K. Chowdhury, G. Hashmi, S.F.U. Farhad, Progress in multijunction solar cells, (2024). https://doi.org/10.48550/arXiv.2405.01550.

- [17] F. Dimroth, High-efficiency solar cells from III-V compound semiconductors, Physica Status Solidi c 3 (2006) 373–379. https://doi.org/10.1002/pssc.200564172.
- [18] S. Boyer-Richard, F. Fan, A. Beck, C. Levallois, K. Tavernier, T. Rohel, R. Bernard, A. Létoublon, C. Cornet, O. Durand, Investigation of III-V GaP solar cell on silicon substrate, EPJ Photovolt. 14 (2023) 31. https://doi.org/10.1051/epjpv/2023020.
- [19] K. Vyas, D.H.G. Espinosa, D. Hutama, S.K. Jain, R. Mahjoub, E. Mobini, K.M. Awan, J. Lundeen, K. Dolgaleva, Group III-V semiconductors as promising nonlinear integrated photonic platforms, Advances in Physics: X 7 (2022) 2097020. https://doi.org/10.1080/23746149.2022.2097020.
- [20] S. Adachi, GaAs, AlAs, and AlxGa1–xAs: Material parameters for use in research and device applications, Journal of Applied Physics 58 (1985) R1–R29. https://doi.org/10.1063/1.336070.
- [21] A.R. Denton, N.W. Ashcroft, Vegard's law, Phys. Rev. A 43 (1991) 3161–3164. https://doi.org/10.1103/PhysRevA.43.3161.
- [22] R.E. Nahory, M.A. Pollack, W.D. Johnston Jr., R.L. Barns, Band gap versus composition and demonstration of Vegard's law for In1–xGaxAsyP1–y lattice matched to InP, Applied Physics Letters 33 (1978) 659–661. https://doi.org/10.1063/1.90455.
- [23] Y. Hu, D. Liang, K. Mukherjee, Y. Li, C. Zhang, G. Kurczveil, X. Huang, R.G. Beausoleil, III/Von-Si MQW lasers by using a novel photonic integration method of regrowth on a bonding template, Light Sci Appl 8 (2019) 93. https://doi.org/10.1038/s41377-019-0202-6.
- [24] D.M. Hansen, T.F. Kuech, Epitaxial Technology for Integrated Circuit Manufacturing, in: R.A. Meyers (Ed.), Encyclopedia of Physical Science and Technology (Third Edition), Academic Press, New York, 2003: pp. 641–652. https://doi.org/10.1016/B0-12-227410-5/00232-5.
- [25] S.K. Jain, M.X. Low, P. Vashishtha, S. Nirantar, L. Zhu, C. Ton-That, T. Ahmed, S. Sriram, S. Walia, G. Gupta, M. Bhaskaran, Influence of Temperature on Photodetection Properties of

- Honeycomb-like GaN Nanostructures, Advanced Materials Interfaces 8 (2021) 2100593. https://doi.org/10.1002/admi.202100593.
- [26] E. Gastellóu, G. García, A.M. Herrera, C. Morales, R. García, G.A. Hirata, M. Robles, J.A. Rodríguez, I.E. García, Brief Review of Growth Techniques for Obtaining of III-V Semiconductor Compounds, EJENG 4 (2019) 17–21. https://doi.org/10.24018/ejeng.2019.4.9.1477.
- [27] J. Simon, K.L. Schulte, K.A.W. Horowitz, T. Remo, D.L. Young, A.J. Ptak, III-V-Based Optoelectronics with Low-Cost Dynamic Hydride Vapor Phase Epitaxy, Crystals 9 (2019) 3. https://doi.org/10.3390/cryst9010003.
- [28] C.J. Funch, A.L. Greenaway, J.W. Boucher, R. Weiss, A. Welsh, S. Aloni, S.W. Boettcher, Close-spaced vapor transport reactor for III-V growth using HCl as the transport agent, Journal of Crystal Growth 506 (2019) 147–155. https://doi.org/10.1016/j.jcrysgro.2018.10.031.
- [29] R. Kapadia, Z. Yu, H.-H.H. Wang, M. Zheng, C. Battaglia, M. Hettick, D. Kiriya, K. Takei, P. Lobaccaro, J.W. Beeman, J.W. Ager, R. Maboudian, D.C. Chrzan, A. Javey, A direct thin-film path towards low-cost large-area III-V photovoltaics, Sci Rep 3 (2013) 2275. https://doi.org/10.1038/srep02275.
- [30] A.L. Greenaway, J.W. Boucher, S.Z. Oener, C.J. Funch, S.W. Boettcher, Low-Cost Approaches to III-V Semiconductor Growth for Photovoltaic Applications, ACS Energy Lett. 2 (2017) 2270–2282. https://doi.org/10.1021/acsenergylett.7b00633.
- [31] K. Ali, A. Khalid, M.R. Ahmad, H.M. Khan, I. Ali, S.K. Sharma, Multi-junction (III-V) Solar Cells: From Basics to Advanced Materials Choices, in: S.K. Sharma, K. Ali (Eds.), Solar Cells: From Materials to Device Technology, Springer International Publishing, Cham, 2020: pp. 325–350. https://doi.org/10.1007/978-3-030-36354-3_13.
- [32] S.P. Philipps, F. Dimroth, A.W. Bett, Chapter I-4-B High-Efficiency III-V Multijunction Solar Cells, in: S.A. Kalogirou (Ed.), McEvoy's Handbook of Photovoltaics (Third Edition), Academic Press, 2018: pp. 439–472. https://doi.org/10.1016/B978-0-12-809921-6.00012-4.

- [33] M. Yamaguchi, F. Dimroth, J.F. Geisz, N.J. Ekins-Daukes, Multi-junction solar cells paving the way for super high-efficiency, Journal of Applied Physics 129 (2021) 240901. https://doi.org/10.1063/5.0048653.
- [34] S.P. Philipps, A.W. Bett, III-V Multi-junction solar cells and concentrating photovoltaic (CPV) systems, Advanced Optical Technologies 3 (2014) 469–478. https://doi.org/10.1515/aot-2014-0051.
- [35] M. Hinojosa, I. Lombardero, C. Algora, I. García, Improved GaInP/GaAs/GaInAs inverted metamorphic triple-junction solar cells by reduction of Zn diffusion in the top subcell, Solar Energy Materials and Solar Cells 248 (2022) 112000. https://doi.org/10.1016/j.solmat.2022.112000.
- [36] S. Essig, J. Benick, M. Schachtner, A. Wekkeli, M. Hermle, F. Dimroth, Wafer-Bonded GaInP/GaAs//Si Solar Cells With 30% Efficiency Under Concentrated Sunlight, IEEE Journal of Photovoltaics 5 (2015) 977–981. https://doi.org/10.1109/JPHOTOV.2015.2400212.
- [37] Z. Ma, D. Liu, Inorganic Flexible Optoelectronics: Materials and Applications, Blackwell Verlag GmbH, Weinheim, Germany, 2019. https://www.wiley.com/en-us/Inorganic+Flexible+Optoelectronics%3A+Materials+and+Applications-p-9783527812981
- [38] M.A. Green, Y. Hishikawa, W. Warta, E.D. Dunlop, D.H. Levi, J. Hohl-Ebinger, A.W.H. Ho-Baillie, Solar cell efficiency tables (version 50), Progress in Photovoltaics: Research and Applications 25 (2017) 668–676. https://doi.org/10.1002/pip.2909.
- [39] W. Shockley, H.J. Queisser, Detailed Balance Limit of Efficiency of p-n Junction Solar Cells, Journal of Applied Physics 32 (1961) 510–519. https://doi.org/10.1063/1.1736034.
- [40] N. Papež, R. Dallaev, Ş. Țălu, J. Kaštyl, Overview of the Current State of Gallium Arsenide-Based Solar Cells, Materials (Basel) 14 (2021) 3075. https://doi.org/10.3390/ma14113075.
- [41] H. Helmers, E. Lopez, O. Höhn, D. Lackner, J. Schön, M. Schauerte, M. Schachtner, F. Dimroth, A.W. Bett, 68.9% Efficient GaAs-Based Photonic Power Conversion Enabled by

- Photon Recycling and Optical Resonance, Physica Status Solidi (RRL) Rapid Research Letters 15 (2021) 2100113. https://doi.org/10.1002/pssr.202100113.
- [42] K. Ando, M. Yamaguchi, Radiation resistance of InP solar cells under light illumination, Applied Physics Letters 47 (1985) 846–848. https://doi.org/10.1063/1.96005.
- [43] T.J. Coutts, S. Naseem, High efficiency indium tin oxide/indium phosphide solar cells, Applied Physics Letters 46 (1985) 164–166. https://doi.org/10.1063/1.95723.
- [44] M. Wanlass, Systems and Methods for Advanced Ultra-High-Performance InP Solar Cells, (2017). https://research-hub.nrel.gov/en/publications/systems-and-methods-for-advanced-ultra-high-performance-inp-solar (accessed December 28, 2024).
- [45] A. Laugier, J. Chevallier, About the band structure of $Ga_xIn_{1-x}P$ alloys, Solid State Communications 10 (1972) 353–356. https://doi.org/10.1016/0038-1098(72)90440-1.
- [46] G.S. Sahoo, P.P. Nayak, G.P. Mishra, An ARC less InGaP/GaAs DJ solar cell with hetero tunnel junction, Superlattices and Microstructures 95 (2016) 115–127. https://doi.org/10.1016/j.spmi.2016.04.045.
- [47] T. Suzuki, A. Gomyo, S. Iijima, Sublattice ordering in GaInP and AlGaInP: Effects of substrate orientations, Journal of Crystal Growth 99 (1990) 60–67. https://doi.org/10.1016/0022-0248(90)90484-3.
- [48] D. Kriegner, J.M. Persson, T. Etzelstorfer, D. Jacobsson, J. Wallentin, J.B. Wagner, K. Deppert, M.T. Borgström, J. Stangl, Structural investigation of GaInP nanowires using X-ray diffraction, Thin Solid Films 543 (2013) 100–105. https://doi.org/10.1016/j.tsf.2013.02.112.
- [49] P.P. Nayak, J.P. Dutta, G.P. Mishra, Efficient InGaP/GaAs DJ solar cell with double back surface field layer, Engineering Science and Technology, an International Journal 18 (2015) 325–335. https://doi.org/10.1016/j.jestch.2015.01.004.
- [50] P. Xue, Y. Wang, E. Tikhonov, Exploring the stable structures and photovoltaic properties of an ideal pseudo-binary alloy: Indium gallium phosphide, Computational Materials Science 209 (2022) 111351. https://doi.org/10.1016/j.commatsci.2022.111351.

- [51] H. Hamada, Characterization of Gallium Indium Phosphide and Progress of Aluminum Gallium Indium Phosphide System Quantum-Well Laser Diode, Materials 10 (2017) 875. https://doi.org/10.3390/ma10080875.
- [52] C. Zhang, J. Zhang, X. Ma, Q. Feng, High-Efficiency III-V Single-Junction and Multi-junction Solar Cells, in: C. Zhang, J. Zhang, X. Ma, Q. Feng (Eds.), Semiconductor Photovoltaic Cells, Springer, Singapore, 2021: pp. 127–175. https://doi.org/10.1007/978-981-15-9480-9_4.
- [53] L. Benbahouche, S.H. Idjdarene, An Improved Performance and High Efficiency DJ III-V Tandem Solar Cell with the Impact of Quantum Tunneling, Appl. Sol. Energy 58 (2022) 739–750. https://doi.org/10.3103/S0003701X22060068.
- [54] S. Essig, S. Ward, M.A. Steiner, D.J. Friedman, J.F. Geisz, P. Stradins, D.L. Young, Progress Towards a 30% Efficient GaInP/Si Tandem Solar Cell, Energy Procedia 77 (2015) 464–469. https://doi.org/10.1016/j.egypro.2015.07.066.
- [55] R.R. King, D.C. Law, K.M. Edmondson, C.M. Fetzer, G.S. Kinsey, H. Yoon, R.A. Sherif, N.H. Karam, 40% efficient metamorphic GaInP/GaInAs/Ge multijunction solar cells, Applied Physics Letters 90 (2007) 183516. https://doi.org/10.1063/1.2734507.
- [56] A. Tukiainen, A. Aho, G. Gori, V. Polojärvi, M. Casale, E. Greco, R. Isoaho, T. Aho, M. Raappana, R. Campesato, M. Guina, High-efficiency GaInP/GaAs/GaInNAs solar cells grown by combined MBE-MOCVD technique, Progress in Photovoltaics: Research and Applications 24 (2016) 914–919. https://doi.org/10.1002/pip.2784.
- [57] S.P. Tobin, S.M. Vernon, C. Bajgar, S. Wojtczuk, M.R. Melloch, A. Keshavarzi, T.B. Stellwag, S. Venkatensan, M. Lundstrom, K.A. Emery, Assessment of MOCVD- and MBE-growth GaAs for high-efficiency solar cell applications, IEEE Transactions on Electron Devices 37 (1990) 469–477. https://doi.org/10.1109/16.46385.
- [58] R.-H. Horng, Y.-C. Kao, A. Sood, P.-L. Liu, W.-C. Wang, Y.-J. Teseng, GaInP/GaAs/poly-Si Multi-Junction Solar Cells by in Metal Balls Bonding, Crystals 11 (2021) 726. https://doi.org/10.3390/cryst11070726.

- [59] A.S. Gudovskikh, J.P. Kleider, N.A. Kalyuzhnyy, V.M. Lantratov, S.A. Mintairov, Band structure at heterojunction interfaces of GaInP solar cells, Solar Energy Materials and Solar Cells 94 (2010) 1953–1958. https://doi.org/10.1016/j.solmat.2010.06.027.
- [60] M.A. Zare Pour, O. Romanyuk, D.C. Moritz, A. Paszuk, C. Maheu, S. Shekarabi, K.D. Hanke, D. Ostheimer, T. Mayer, J.P. Hofmann, W. Jaegermann, T. Hannappel, Band energy diagrams of n-GaInP/n-AlInP(100) surfaces and heterointerfaces studied by X-ray photoelectron spectroscopy, Surfaces and Interfaces 34 (2022) 102384. https://doi.org/10.1016/j.surfin.2022.102384.
- [61] J. Lim, N.-G. Park, S.I. Seok, M. Saliba, All-perovskite tandem solar cells: from fundamentals to technological progress, Energy Environ. Sci. 17 (2024) 4390–4425. https://doi.org/10.1039/D3EE03638C.
- [62] A. Polman, M. Knight, E.C. Garnett, B. Ehrler, W.C. Sinke, Photovoltaic materials: Present efficiencies and future challenges, Science 352 (2016) aad4424. https://doi.org/10.1126/science.aad4424.
- [63] H. Sugiura, C. Amano, A. Yamamoto, M. Yamaguchi, Double Heterostructure GaAs Tunnel Junction for a AlGaAs/GaAs Tandem Solar Cell, Jpn. J. Appl. Phys. 27 (1988) 269. https://doi.org/10.1143/JJAP.27.269.
- [64] J.M. Olson, S.R. Kurtz, A.E. Kibbler, P. Faine, A 27.3% Efficient Ga0.5In0.5P/GaAs Tandem Solar Cell, Applied Physics Letters 56 (1990) 623–625. https://doi.org/10.1063/1.102717.
- [65] T. Takamoto, E. Ikeda, H. Kurita, M. Ohmori, Over 30% efficient InGaP/GaAs tandem solar cells, Applied Physics Letters 70 (1997) 381–383. https://doi.org/10.1063/1.118419.
- [66] T. Takamoto, E. Ikeda, H. Kurita, M. Ohmori, M. Yamaguchi, M.-J. Yang, Two-Terminal Monolithic In0.5Ga0.5P/GaAs Tandem Solar Cells with a High Conversion Efficiency of Over 30%, Jpn. J. Appl. Phys. 36 (1997) 6215. https://doi.org/10.1143/JJAP.36.6215.
- [67] B.M. Kayes, L. Zhang, R. Twist, I.-K. Ding, G.S. Higashi, Flexible Thin-Film Tandem Solar Cells With >30% Efficiency, IEEE J. Photovoltaics 4 (2014) 729–733. https://doi.org/10.1109/JPHOTOV.2014.2299395.

- [68] N.R.E. Laboratory, NREL reports world record 31.1 percent efficiency for III-V solar cell, (n.d.). https://phys.org/news/2013-06-nrel-world-percent-efficiency-iii-v.html
- [69] M.A. Steiner, R.M. France, J. Buencuerpo, J.F. Geisz, M.P. Nielsen, A. Pusch, W.J. Olavarria, M. Young, N.J. Ekins-Daukes, 32.9% efficient tandem solar cell with strain-balanced GaInAs/GaAsP quantum wells, in: 2021 IEEE 48th Photovoltaic Specialists Conference (PVSC), IEEE, Fort Lauderdale, FL, USA, 2021: pp. 1084–1085. https://doi.org/10.1109/PVSC43889.2021.9518819.
- [70] J.B. Makambo, P.E. Imoisili, T.C. Jen, Efficiency Assessment of GaInp/GaAs Tandem Solar Cells: Analytical Investigation and Numerical Simulation, Key Engineering Materials 997 (2024) 53–60. https://doi.org/10.4028/p-MO0K11.
- [71] M. Yamaguchi, T. Okuda, S.J. Taylor, T. Takamoto, E. Ikeda, H. Kurita, Superior radiation-resistant properties of InGaP/GaAs tandem solar cells, Applied Physics Letters 70 (1997) 1566–1568. https://doi.org/10.1063/1.118618.
- [72] D. Shahrjerdi, S.W. Bedell, C. Bayram, C.C. Lubguban, K. Fogel, P. Lauro, J.A. Ott, M. Hopstaken, M. Gayness, D. Sadana, Ultralight High-Efficiency Flexible InGaP/(In)GaAs Tandem Solar Cells on Plastic, Advanced Energy Materials 3 (2013) 566–571. https://doi.org/10.1002/aenm.201200827.
- [73] K. Schulte, J. Simon, A. Ptak, Multijunction GaInP/GaAs Solar Cells Grown by Hydride Vapor Phase Epitaxy, MRS Spring Meeting & Exhibit, 2-6 April (2018) Phoenix, Arizona. https://research-hub.nrel.gov/en/publications/multijunction-gainpgaas-solar-cells-grown-by-hydride-vapor-phase-
- [74] P. Dai, S.L. Lu, M. Arimochi, S. Uchida, T. Watanabe, X.D. Luo, H. Yang, Carriers transport properties in GaInP solar cells grown by molecular beam epitaxy, Solid State Communications 200 (2014) 9–13. https://doi.org/10.1016/j.ssc.2014.09.012.
- [75] S. SaeidNahaei, H.-J. Jo, S.J. Lee, J.S. Kim, S.J. Lee, Y. Kim, Investigation of the Carrier Movement through the Tunneling Junction in the InGaP/GaAs Dual Junction Solar Cell Using the Electrically and Optically Biased Photoreflectance Spectroscopy, Energies 14 (2021) 638. https://doi.org/10.3390/en14030638.

Chapter II: GaInP/GaAs Solar Cells

- [76] D.J. Friedman, J.M. Olson, S. Kurtz, High-Efficiency III-V Multijunction Solar Cells, in: Handbook of Photovoltaic Science and Engineering, John Wiley & Sons, Ltd, 2010: pp. 314–364. https://doi.org/10.1002/9780470974704.ch8.
- [77] K. Medjoubi, Investigation of new solar cell technology III-V//Si behavior under irradiations for space applications, phdthesis, Institut Polytechnique de Paris, 2021. https://theses.hal.science/tel-03220969

Chapter III Study of Multilayer Solar Cells Based on GaInP/GaAs Heterojunction

III.1 Introduction

Multi-layer solar cells based on the GaInP/GaAs heterojunction offer several advantages due to the unique electronic properties of the semiconductor materials GaInP and GaAs, such as high absorption coefficients and the ability to tune the energy bandgap E_g . Additionally, the excellent lattice matching between GaInP and GaAs when integrated into a multi-layer structure allows for better utilization of the solar spectrum, facilitating the enhancement of the photovoltaic conversion efficiency of the resulting solar cell [1-3].

In this chapter, we will study multi-layer solar cells based on the GaInP/GaAs heterojunction, considering two types of solar cells: a single-junction and a dual-junction tandem cell. In this study, we assume that the cells are exposed to standard solar irradiation AM1.5 with optical power of $P_{opt} = 0.099271 \, W/cm^2$ at an ambient temperature of T = 300K. The research primarily involves numerical simulations of the considered cells using the Solis-1D simulation software, which enables the calculation of their electrical properties, such as the current density-voltage (J - V) and the power -voltage (P - V) characteristics. From these results, we derive the photovoltaic output parameters of the cells, including short-circuit current density (J_{sc}) , open-circuit voltage (V_{oc}) , maximum output power (P_{max}) , fill factor (FF) and photovoltaic conversion efficiency (E_{ff}) .

By analyzing the effects of varying thickness and doping concentrations in different layers, we aim to optimize the photovoltaic conversion efficiency of both the single-junction and dual-junction tandem cells.

III.2. 1D Semiconductor Device Simulator: Solis

Solis (Semiconductor One-dimensional Lateral and Interfacial Simulator) is a sophisticated one-dimensional semiconductor device simulator designed with a high-performance, modular computational engine coded in C++. It features a user-friendly interface developed in C, which operates independently from the simulation engine. Solis utilizes the drift-diffusion model to simulate both graded and abrupt heterostructures—ideal for applications such as solar cells and detectors—while accounting for various recombination mechanisms, including Auger, radiative, and Shockley-Read-Hall (SRH). It also models donor-like and acceptor-like traps, incomplete dopant ionization, Schottky rectifying contacts, and

spontaneous and piezoelectric polarization in III-N materials. Moreover, Solis supports photogeneration using the AM1.5 solar spectrum or any user-defined spectrum. The simulator provides outputs such as current-voltage and capacitance-voltage characteristics, quantum efficiency, band diagrams, and spatial distributions of carrier densities, ionized dopants and traps, generation/recombination rates, and electric fields [4].

Solis offers advanced capabilities that set it apart from earlier one-dimensional simulators like PC1D and AMPS-1D. It supports spontaneous and piezoelectric polarizations, a crucial feature for wurtzite-structured semiconductor materials such as gallium nitride and its related alloys. Additionally, it provides a more detailed approach to modeling Schottky contacts and heterostructures while enabling integrated simulation of graded semiconductor devices [4].

III.2.1 Modeling, numerical methods, and implementation

The Solis simulation engine employs the drift-diffusion model, widely recognized as the standard physical framework for analyzing and determining the electrical characteristics of semiconductor devices [5]. Solis utilizes both the coupled Newton method and the decoupled Gummel method to efficiently solve the model equations [4].

The drift-diffusion model consists of the Poisson equation along with two current continuity equations, presented in a one-dimensional (x) and normalized format in Eqs. (III.1) -(III.3). The Poisson equation is normalized by setting its factor to unity, employing the Debye length as the reference parameter for position normalization [4].

$$\frac{d}{dx} \left(\varepsilon(x) \frac{d\psi(x)}{dx} + P(x) \right) = n(x) - p(x) + N_A^-(x) - N_D^+(x) + \sum_t N_{tA}^-(x) - \sum_t N_{tD}^+(x)$$
 (III.1)

$$\begin{cases} \frac{dJ_n}{dx} = -GR(x)/\gamma^2 \\ \frac{dJ_p}{dx} = +GR(x)/\gamma^2 \end{cases}$$
(III.2)

$$\begin{cases} J_n(x) = -n(x)\mu_n \frac{d\phi_n(x)}{dx} \\ J_p(x) = +p(x)\mu_p \frac{d\phi_p(x)}{dx} \end{cases}$$
(III.3)

with the electrostatic potential ψ , the spontaneous and piezoelectric polarization P (if any), the permittivity ε , the free electron concentration n, the free hole concentration p, the ionized donor N_D^+ and ionized acceptor concentration N_A^- , and the ionized donor- N_{tD}^+ and acceptor-like trap concentration N_{tA}^- . The concentrations can vary with the position coordinate x. J_n and J_p are the

electron and hole current densities, and GR is the net generation term. γ^2 is a normalization parameter (the continuity factor shown in Table III.1). μ_n and μ_p are the electron and hole mobilities, while ϕ_n and ϕ_p are the normalized quasi-Fermi levels [4].

Table III.1: The normalization factors employed in the drift-diffusion model [4].

Parameter	Normalization factor		
Permittivity	ϵ_0		
Potential	Thermal voltage, kT/q		
Energy	Thermal energy, kT		
Carrier concentration	$N = 10^{22} \mathrm{m}^{-3}$		
Space	Debye length, $L = \sqrt{\varepsilon_0 kT/(q^2 N)}$		
Mobility	$\mu_0 = 0.1 \mathrm{m}^2/\mathrm{V}\text{-s}$		
Recombination	$\beta_0 = 10^{-20} \mathrm{m}^3/\mathrm{s}$		
Continuity factor	$\gamma^2 = \mu_0 kT / \left(\beta_0 q N L^2\right)$		

All the parameters in these equations are dimensionless, meaning they are normalized using the normalization parameters defined in Table III.1. The currents are expressed in terms of quasi-Fermi levels for simplicity and include both drift and diffusion components. The net generation term GR(x) accounts for light-induced carrier generation (photogeneration) and various recombination processes, including nonradiative Shockley-Read-Hall (SRH), radiative, and Auger mechanisms [4].

The drift-diffusion model as defined in Eqs. (III.1) -(III.3) is solved to determine the potential $\psi(x)$ and the quasi-Fermi levels $\phi_n(x)$ and $\phi_p(x)$. The other quantities are then calculated using these fundamental parameters. The Scharfetter-Gummel discretization scheme [6] is used to ensure the numerical stability needed in this partial differential equation (PDE) system.

The discretized system of partial differential equations (PDEs) is subsequently solved using two different methods available in Solis, providing full flexibility in the solution process.

- The Gummel iterative decoupled method. In this method, the three equations are solved iteratively until convergence: Starting with initial guess vectors $\psi(x)$, $\phi_n(x)$, and $\phi_p(x)$, Solis solves the discretized Poisson system using the Newton-Raphson method and determines the new value of the potential vector $\psi(x)$, which is then used to solve the electron continuity

equation and determine the $\phi_n(x)$ vector. $\psi(x)$ and $\phi_n(x)$ are then used to solve the hole continuity equation to obtain the $\phi_p(x)$ vector, and the process iterates until convergence. A damping strategy is implemented in Solis to ensure convergence in most cases, since this method can converge slowly for problems where the three drift-diffusion equations are highly coupled [4].

- The Newton method solves the full discretized nonlinear drift-diffusion PDE system simultaneously using the Newton-Raphson method. This method is suitable for highly coupled cases and can converge fast, providing that a good starting solution is given. Solis provides a starting point for the solver to speed up the convergence, and can also use the Gummel method to refine the initial guess [4].

Solis can handle both Dirichlet and Neumann boundary conditions. The device contacts can be nonideal ohmic or rectifying (Schottky). The numerical parameters, such as the starting initial guess, the damping parameter and tolerance, and the boundary conditions, can be set by the user to handle specific structures, even if Solis automatically adapts these parameters for convergence. Solis has been developed with modularity, versatility, and performance as the main criteria and guidelines. Its general architecture is shown in Figure III.1, and its main components are [4]:

- The simulator driver, soliscomp.exe (or soliscomp under Linux), controlling the simulator engine. The driver and the simulation engine are developed in standard C++, implementing the numerical methods described above and handling the whole simulation process: input file format and device definition, memory management, data input and output, and solving procedures. The simulator driver also controls the embedded Lua scripting engine that can be used to implement user-defined physical models and parameters, permitting advanced control of the simulation process. The simulator driver is a command-line executable with a device input in a simple and clean text format. It can be easily controlled and automated by any language (and thus the embedded Lua interpreter), giving the user unprecedented flexibility and control over the simulation.
- A graphical device editor, solisdevice.exe (or solisdevice under Linux), implemented in C. This tool provides an easy-to-use graphical frontend to Solis.
- An advanced code editor, solisedit.exe (or solisedit under Linux), implemented in C, to edit the device structure using the straightforward Solis syntax. This editor offers all the functionality found in modern editors and can be used as a general code editor.

- A data plotter, solisplot.exe (under Windows) or solisplot (under Linux), implemented in C and C++. This tool is used by Solis to plot the simulation results but could also be used as a standalone data plotter.
- An advanced scientific calculator, soliscalc, implemented in C.

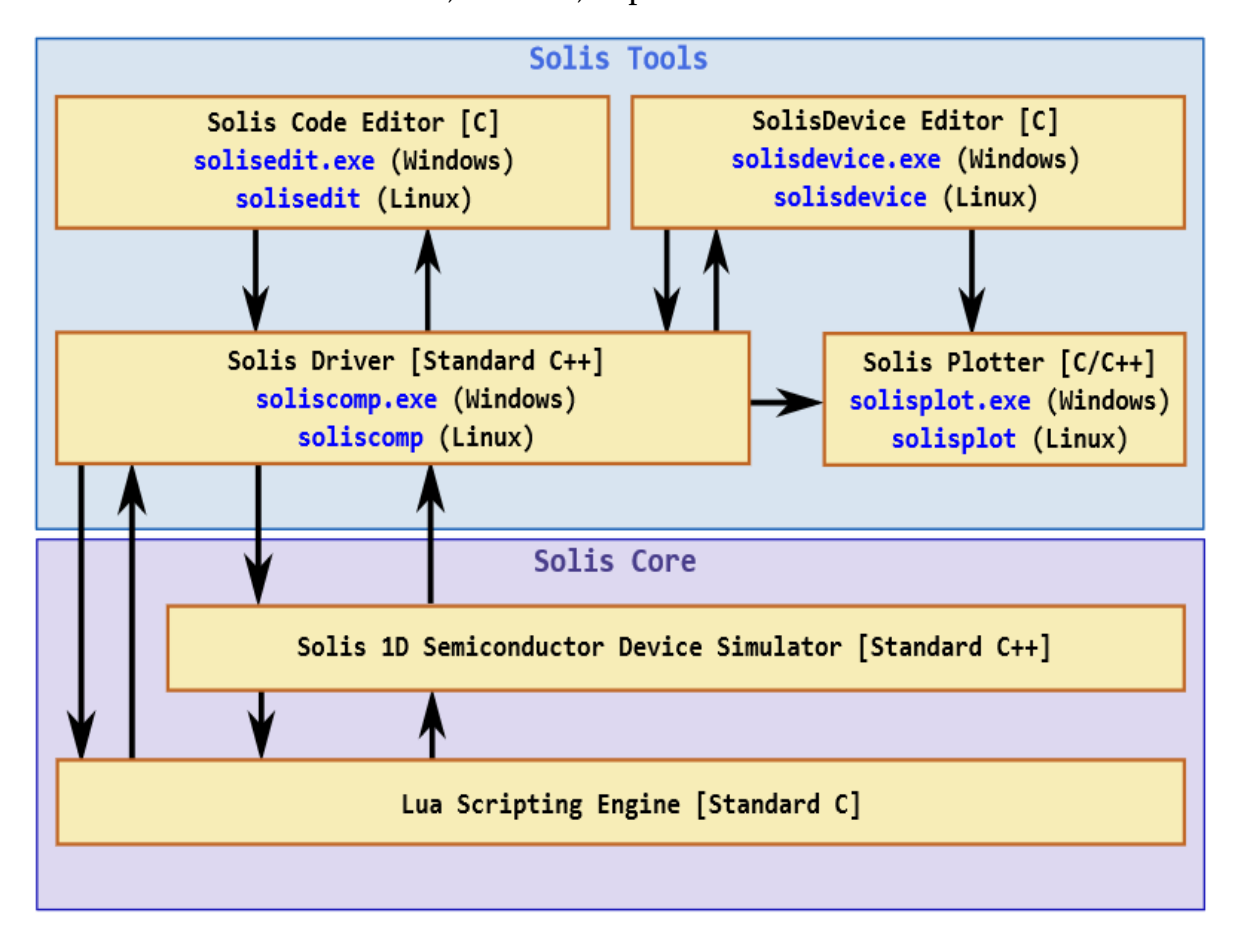


Figure III.1: A schematic of the Solis architecture. The core part of Solis is entirely coded in standard C++ (the Lua engine being coded in standard C) and is easily portable to almost all operating systems, in addition to the natively supported Windows and Linux systems. The Solis code editor, device editor, and data plotter are developed in C and use the IUP GUI toolkit coded in C [7] and the Scintilla component coded in C++ [8].

These tools are independent and can be used in a complementary way; For example, solisdevice can be used to perform simulations in a complete graphical environment. To develop a complete simulation framework, with custom physical models and optimization scripts, one can use solisedit to achieve full control over the code. These tools are, by design, compatible; e.g., an input file created with the code editor can be open/modified by the graphical device editor, and vice versa [4].

III.2.2 Solis Input File Format

The Solis input format is an easy-to-use plain-text format with a simple syntax and some useful features such as variable definition and a mathematical parser.

Solis simulates a device structure such as shown in Figure III.2. To describe such a device, Solis uses a very simple input file format, inspired by the INI format. With this text format, Solis input file is simple to generate/handle, to read and understand. The Solis input file extension is .solis. The basic syntax of a Solis input is shown in Figure III.3 [9].

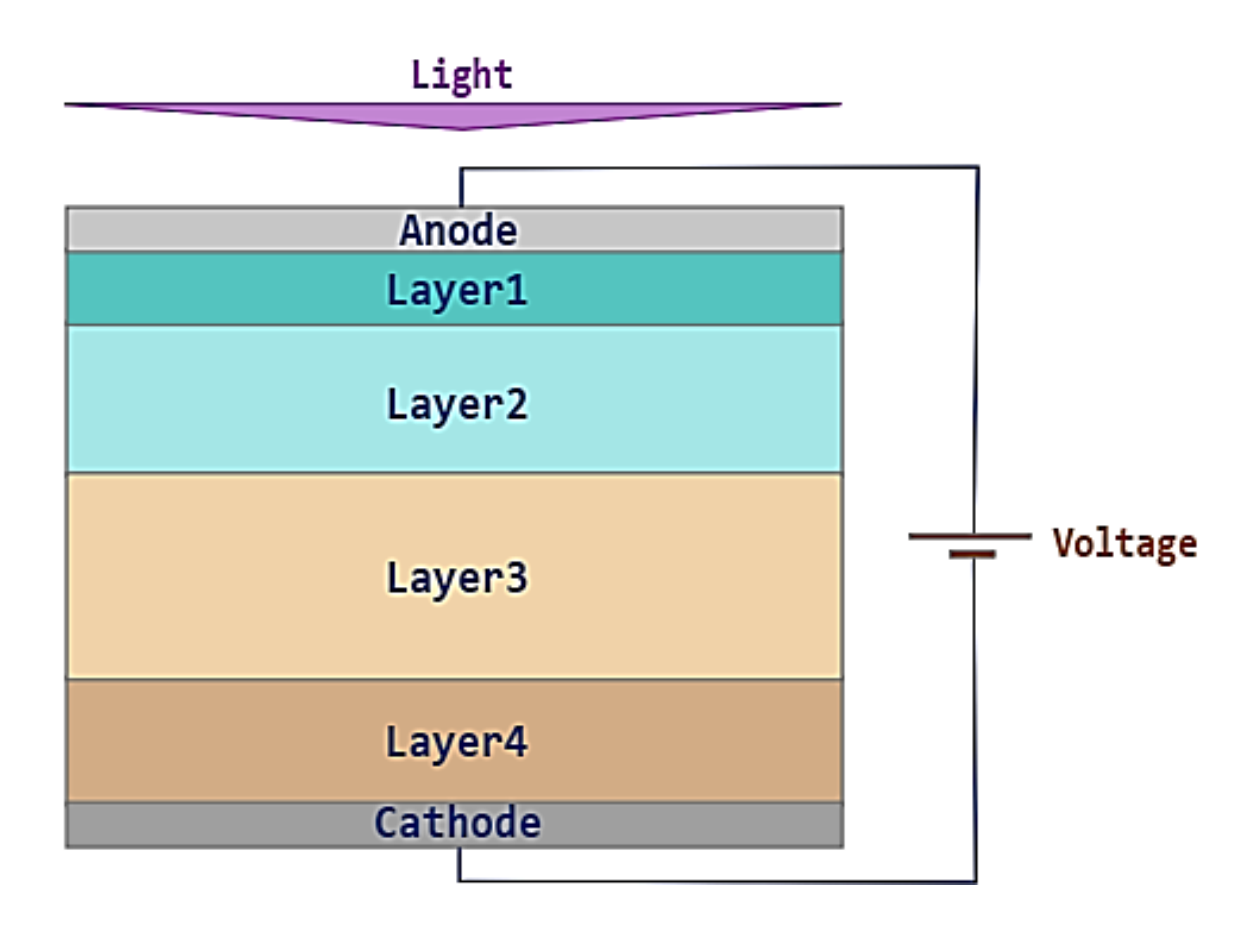


Figure III.2: A schematic structure of a device as simulated by Solis [9].

```
fig-Origin-graded0405-nkSingleGalnP08-GaAs12.solis
      # Solis <SL>
     # Solis <Version 3.0 Build 2311>
 4 □ [Device]
          # Name="NP-GaInP/GaAs single solar cell"
 5
          Temperature=300
 7

  □

  [Layer1]

 8
          Material="InGaP"
          Composition.x=0.4
 9
          Thickness=0.8
10
11
         Mesh.Points=600
12
    □ [Layer2]
          Material="GaAs"
13
          Thickness=1.2
14
15
          Mesh.Points=600
16 ☐ [Anode]
17
          Anode.Type="Ohmic"
18
          Anode.Boundary="Neumann"
19
    □ [Cathode]
          Cathode.Type="Ohmic"
20
21
          Cathode.Phi=0
22
          Cathode.Boundary="Neumann"
23
    □ [Voltage]
24
          Voltage.Source="Npne"
25
          Voltage.Start=-2
26
27
          Voltage.End=2
28
          Voltage.Step=0.005
29
          Voltage.Jinf=-2000
30
          Voltage.Jsup=2000
31 ♀ [Light]
          Light.Source="AM1.5"
32
33
          Light.Start=0.2
                                                                       Solis
                                                                                    Ln 17 / 53
                                                                                                       Col 23
```

Figure III.3: Solis Input Syntax [9].

III.2.3. Solis tools

Five independent tools are distributed with Solis [9]:

- A code editor, solisedit.exe (or solisedit under Linux).
- A graphical device editor, solisdevice.exe (or solisdevice under Linux).
- A data plotter, solisplot.exe (or solisplot under Linux).
- Only for Linux: solisparallel, to run solar cell parallel simulations using MPI (Message Passing Interface).
- A scientific calculator, soliscalc.exe (or soliscalc under Linux).
- A database tool, solisdatabase.exe (Windows) or solisdatabase (Linux).

In addition, Solis includes an interactive terminal emulator (solisterm, only under Linux), a standalone version of the embedded terminal in SolisEdit.

The Solis code editor, SolisEdit, is completely configurable and provides all of the features of contemporary editors, including syntax highlighting, autocompletion, markers, indentation control, find/replace, and file explorer (Figure III.4).

The Solis input files (. solis) and model files (.lua) may be edited using SolisEdit. It also supports a number of languages that scientists and engineers use, including C/C++, Bash, Python, Octave, Fortran, LATEX1, and Makefile. The language is automatically selected based on the file extension.

To make working with files easier, SolisEdit incorporates a File Explorer. One can configure the File Explorer to display just certain files (filter) based on their extension by right-clicking the root directory and choosing the appropriate filter [9]. A system of colored markers that are shown in the margins of the current documents in SolisEdit (Figure III.4) allows users to view the edited or saved parts of the document in real time. By choosing Edit/Remove Markers from the menu, one can reset the markers at any moment [9].

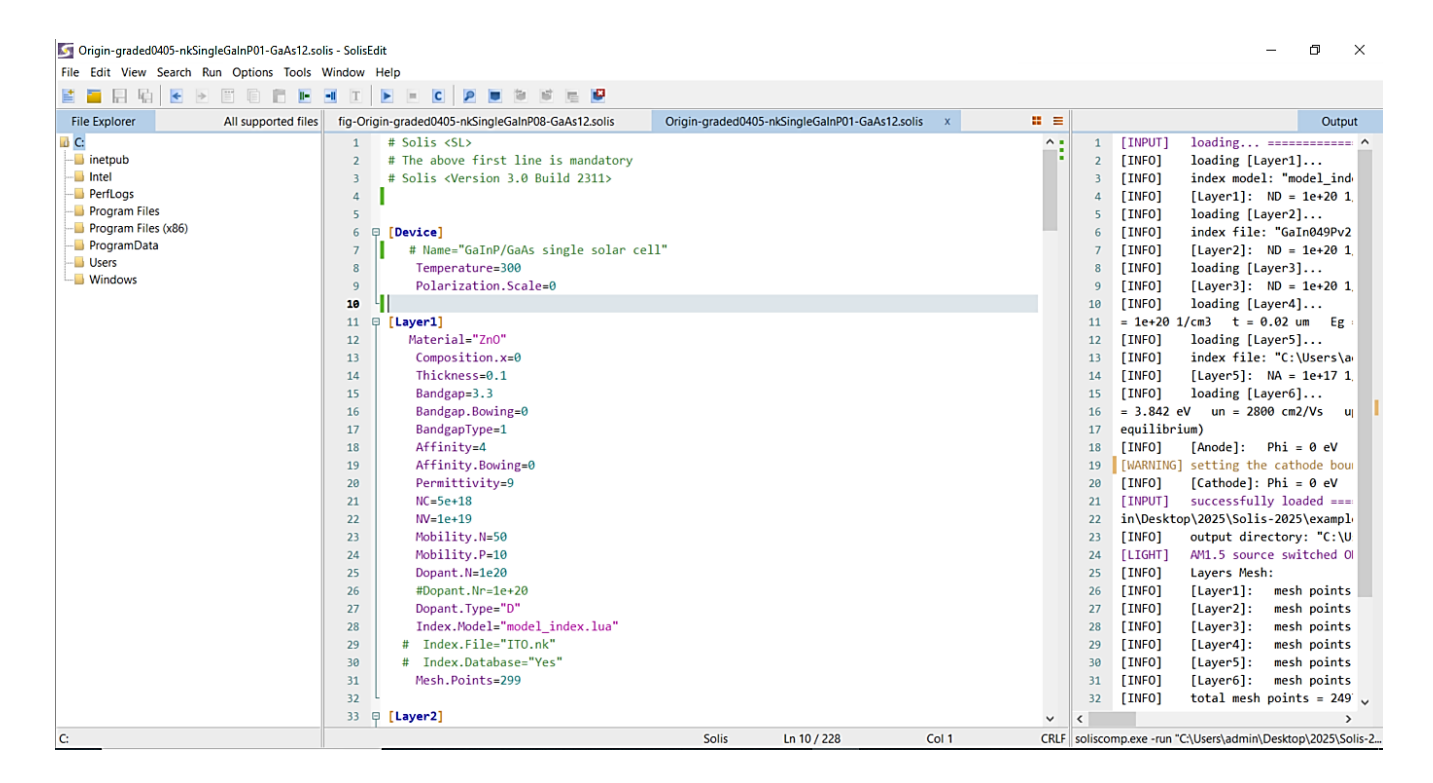


Figure III.4: SolisEdit Screenshot [9].

SolisDevice is the Solis graphical device editor to build graphically the device to simulate. It offers a very easy way to perform simulations with a simple and functional user interface (screenshot in Figure III.5).

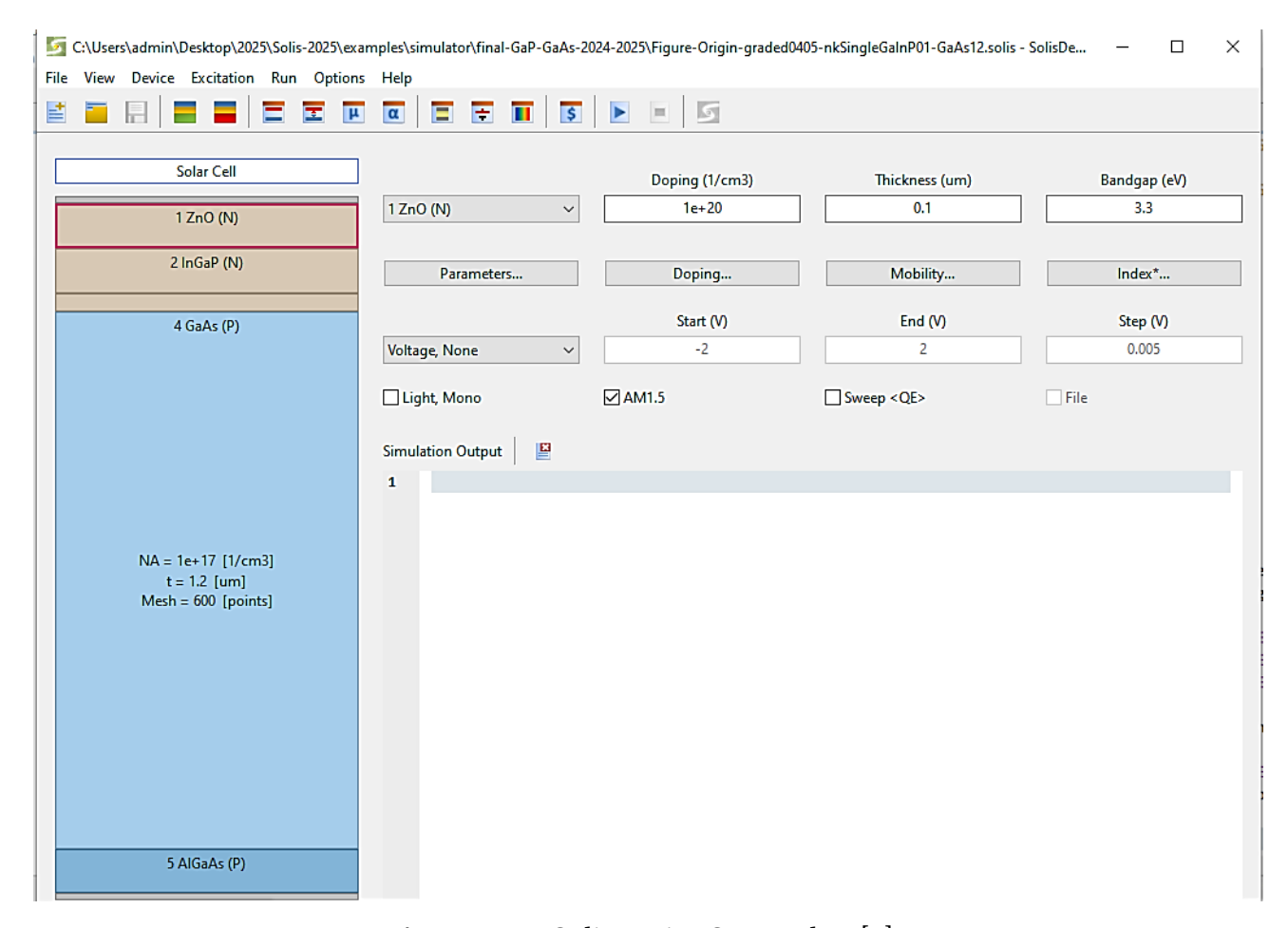


Figure III.5: SolisDevice Screenshot [9].

It generates the same input file than entered with SolisEdit. An input graphically created with SolisDevice can be edited with SolisEdit and vice-versa. With SolisDevice one can add/move/resize/delete a layer and set the material parameters. In the layer parameters dialog (Figure III.6), one can enter the semiconductor material properties: bandgap, affinity, permittivity, direct, Auger and SRH recombination, etc. The layer material can be set using the integrated Solis database: Device/Material... menu. In this dialog, one can also select Lua model files for bandgap and permittivity [9].

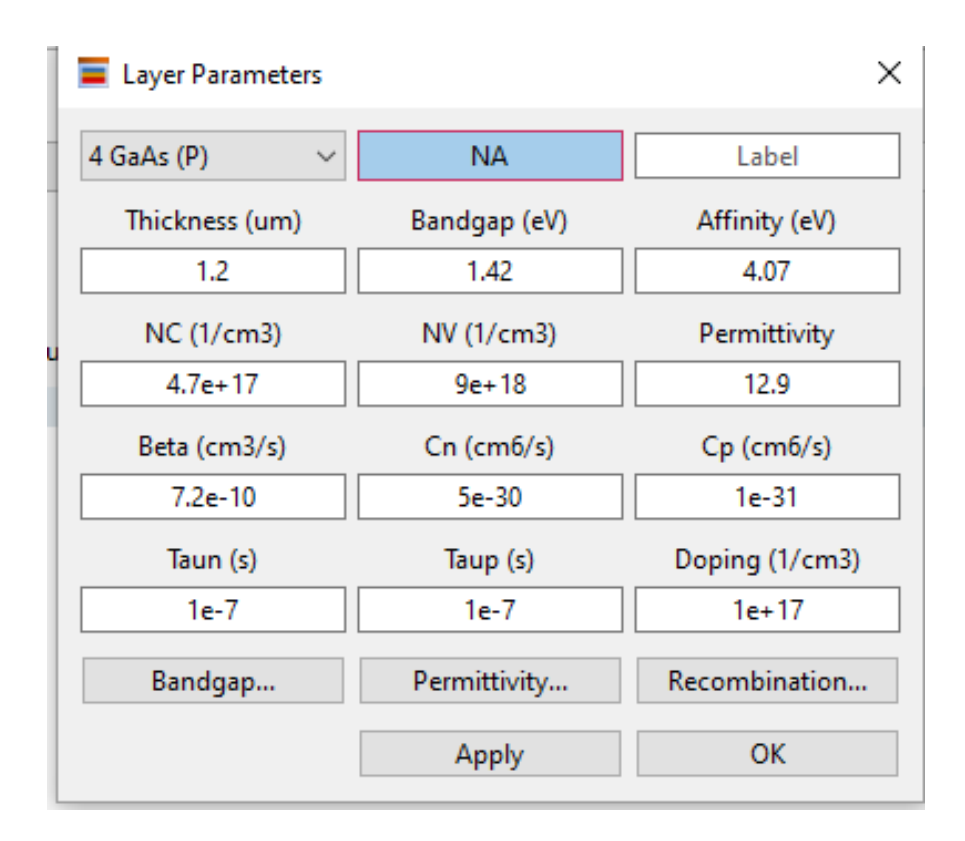


Figure III.6: SolisDevice: Parameters Dialog [9].

By selecting the **Doping** button, the relevant window (Figure III.7) may be used to adjust the layer doping settings. These parameters correspond to the dopant type and concentration, the reference concentration, and the electron and hole lifetimes. the doping Lua model file can also be selected in this dialog.

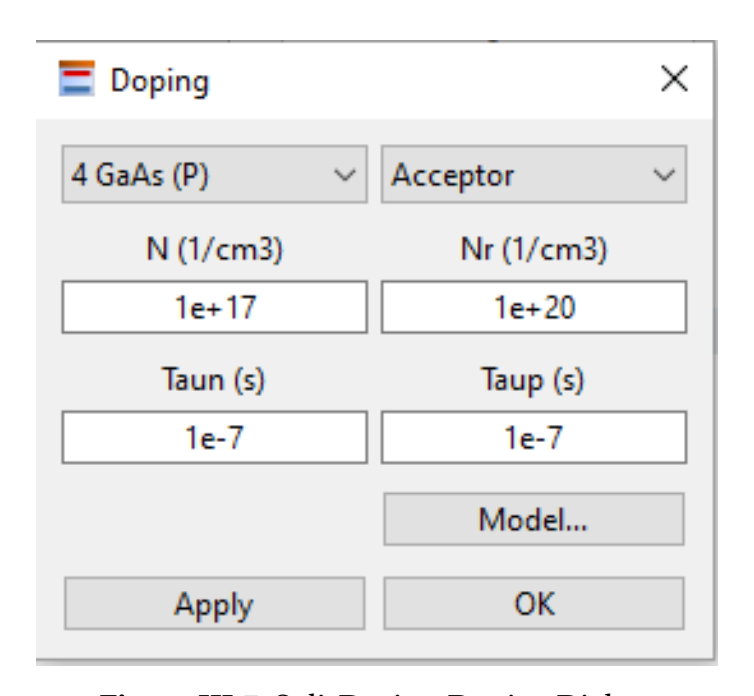


Figure III.7: SolisDevice: Doping Dialog.

Traps can be added/deleted/modified using the corresponding dialog shown by selecting the Device/Traps... menu (Figure III.8). Defect parameters correspond to the type and concentration of defects, the reference concentration, the activation energy, the lifetimes of electrons and holes, and the trap degeneracy. A Lua model file for traps can also be selected in this dialog.

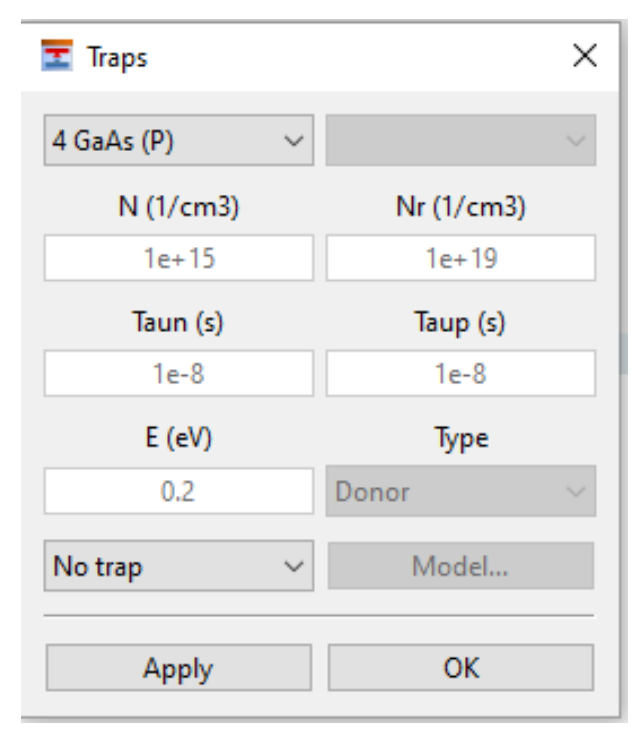


Figure III.8: SolisDevice: Traps Dialog.

By selecting the Device/Index... menu, the Refractive Index and Extinction Coefficient are configured in the window that appears (Figure III.9). Selecting the Lua model file for extinction coefficient and refractive index spectra may also be done in this box by pressing the Model... button.

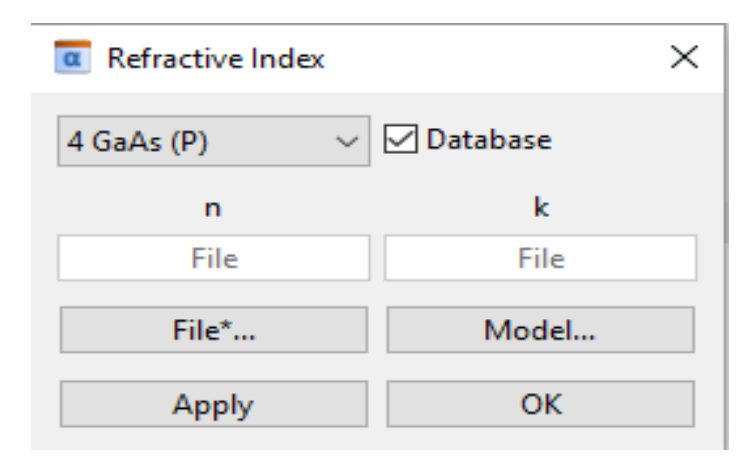


Figure III.9: SolisDevice: Refractive Index and Extinction Coefficient Dialog.

Anode and Cathode parameters are defined in the dialog shown by selecting the Device/Contacts... menu (Figure III.10). To define the Lua model file for the anode and cathode refractive index and extinction coefficient spectra, one press the Model... button.

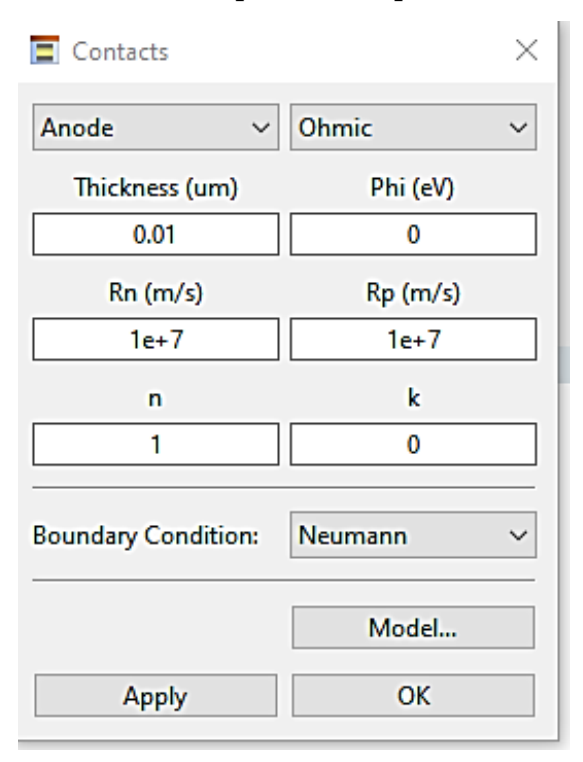


Figure III.10: SolisDevice: Anode and Cathode Dialog.

To define the Voltage and Light parameters, one uses the corresponding dialog shown by selecting the Device/Voltage... or the Device/Light... menu (Figure III.11). To set custom voltage sweep, one press File... in the voltage dialog. Similarly, one can define custom light spectrum by selecting File... in the light dialog.

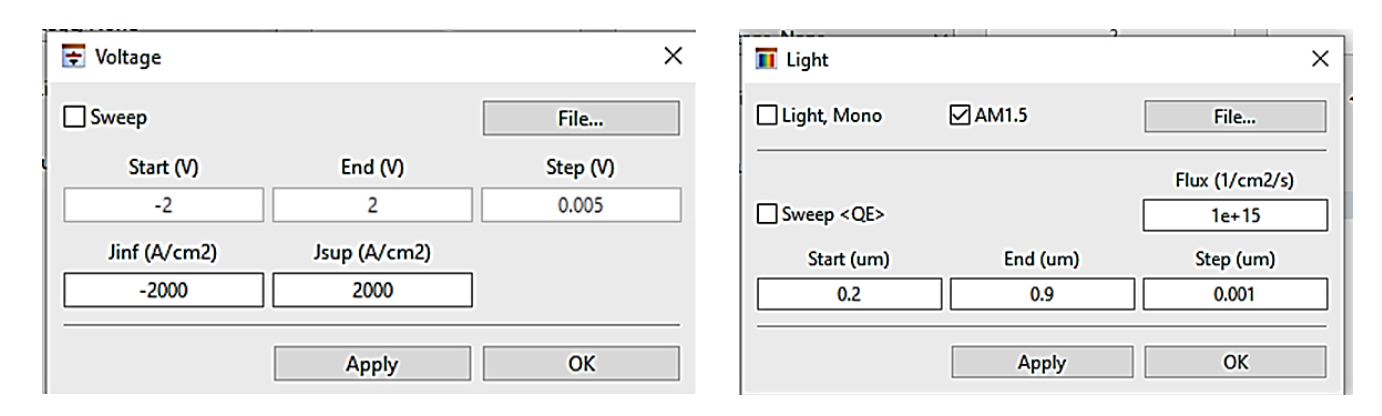


Figure III.11: SolisDevice: Voltage and Light Dialog.

The Solis data plotter, SolisPlot (screenshot in Figure III.12), is usually not used as a standalone application. It is rather used by the simulator driver soliscomp, the code editor SolisEdit or the

graphical device editor SolisDevice to plot the simulation results. But it can be used alone to directly plot simulation results or other data. To do so, one just launches SolisPlot, browse to the simulation output directory and select the corresponding file as shown on Figure III.13 for (J - V) characteristic curve of a simulated solar cell. With SolisPlot, one can control every aspect of the plot curves, axes, scale, add lines, etc. The plot can be saved in the SVG format (and PDF format under Linux).

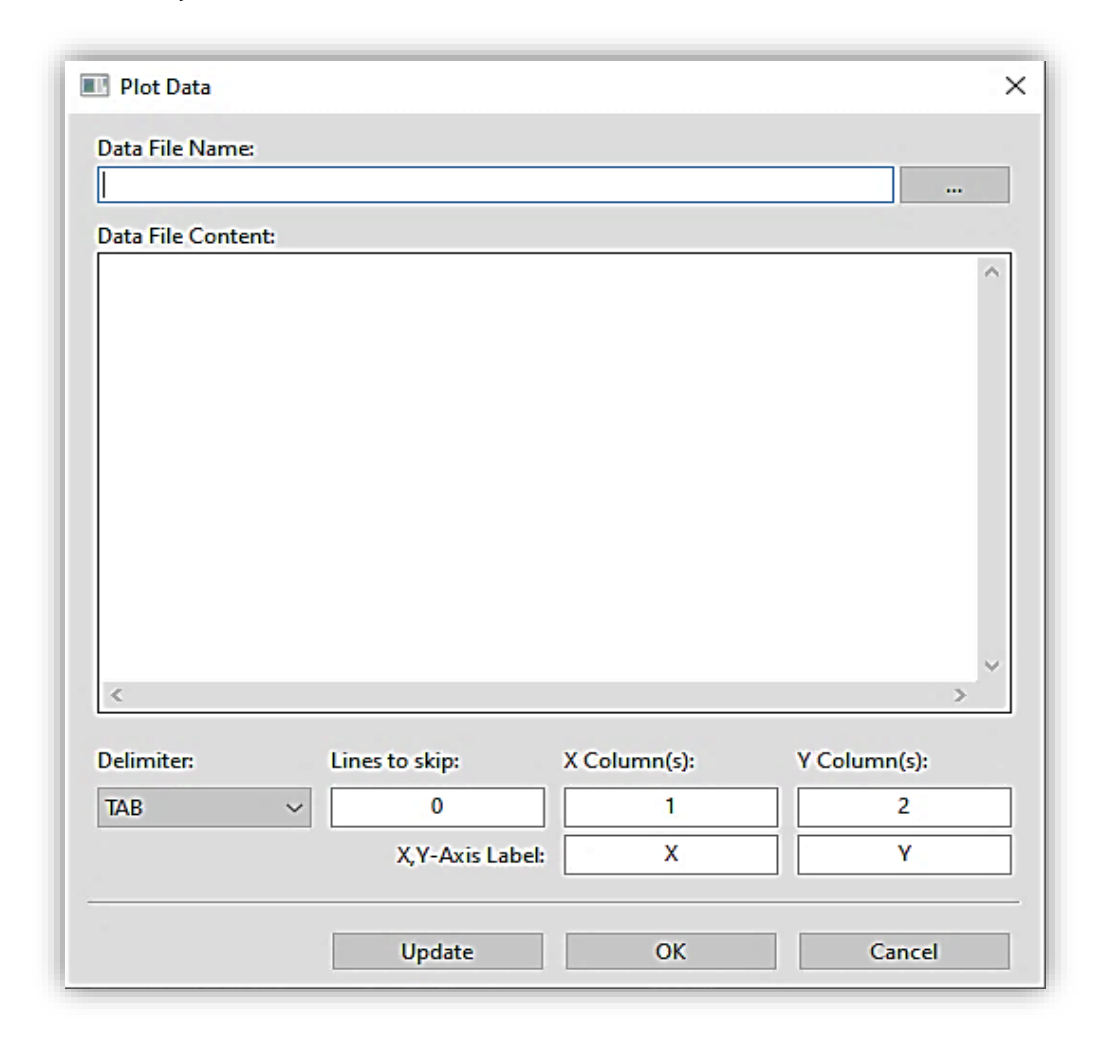


Figure III.12: SolisPlot Screenshot.

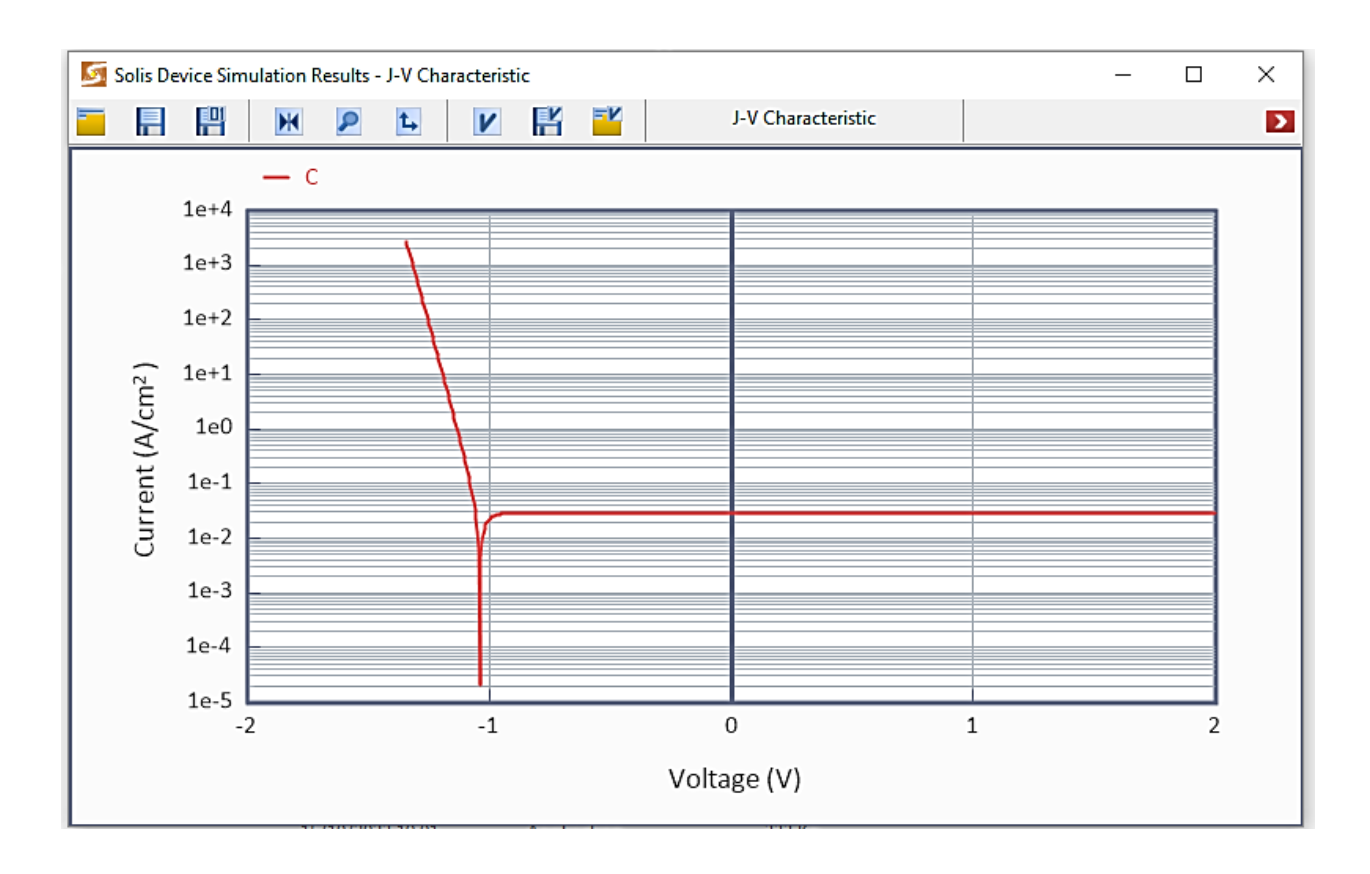


Figure III.13: (J - V) curve from SolisPlot.

III.3 Description of the studied multilayer solar cells based on GaInP/GaAs heterojunction

The studied solar cells based on GaInP/GaAs heterojunction are designed in single and tandem configurations and are illustrated respectively in cases (a) and (b) of Figure III.14. The input parameters related to each layer of the simulated solar cells are summarized in Table III.2. In addition to the top anode and bottom cathode, the single solar cell (Figure III.14 (a)) consists of the following layers:

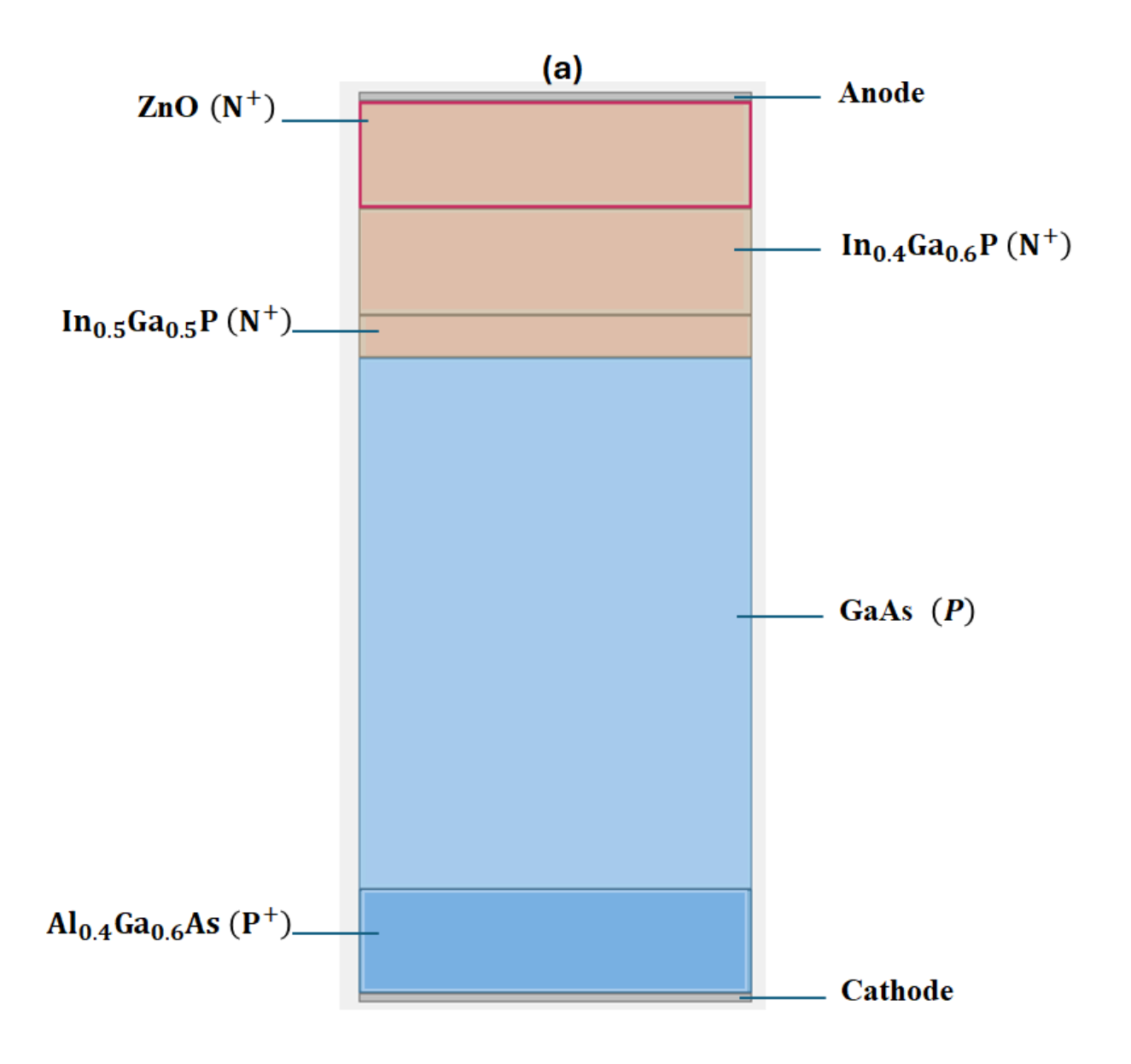
- ✓ A highly doped N-type (N^+) ZnO region of 0.1 µm thickness.
- \checkmark A highly doped N-type (N⁺) In_{0.4}Ga_{0.6}P region of 0.1 μm thickness.
- ✓ A highly doped N-type (N^+) In_{0.5}Ga_{0.5}P region of 0.04 µm thickness.
- ✓ A doped P-type GaAs region of 1.2 µm thickness.
- ✓ A highly doped P-type (P^+) Al_{0.4}G $a_{0.6}$ As region of 0. 1 µm thickness.

The tandem solar cell (Figure III.14 (b)) consists of the following layers:

- ✓ A highly doped N-type (N^+) ZnO region of 0.1 µm thickness.
- ✓ A highly doped N-type (N^+) I $n_{0.4}$ G $a_{0.6}$ P region of 0.1 µm thickness.
- \checkmark A doped P-type In_{0.4}Ga_{0.6}P region of 0.1 μm thickness.

Chapter III: Study of Multilayer Solar Cells Based on GaInP/GaAs Heterojunction

- ✓ A highly doped P-type (P^+) I $n_{0.4}$ G $a_{0.6}$ P region of 0.01 µm thickness.
- ✓ A highly doped N-type (N^+) I $n_{0.5}$ G $a_{0.5}$ P region of 0.01 μ m thickness.
- ✓ A highly doped N-type (N^+) GaAs region of 0.1 µm thickness.
- ✓ A doped P-type GaAs region of 1.2 µm thickness.
- ✓ A highly doped P-type (P^+) Al_{0.4}G $a_{0.6}$ As region of 0. 1 µm thickness.



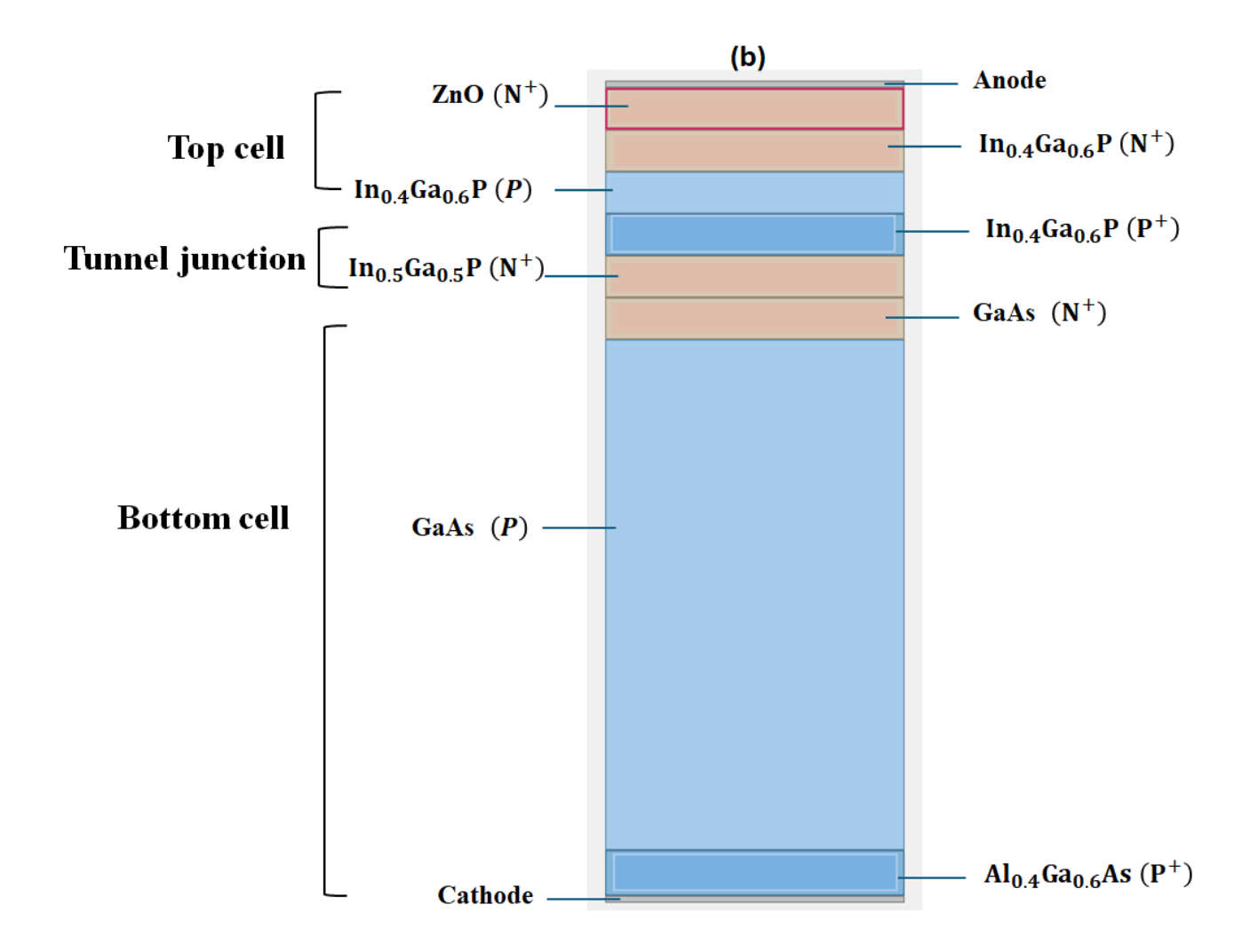


Figure III.14: Structure of the studied solar cells based on GaInP/GaAs heterojunction: (a) Single solar cell, (b) tandem solar cell.

Table III.2. Baseline parameters for modeling the single and tandem solar cells based on GaInP/GaAs heterojunction at $T = 300 \, ^{\circ}K$.

Parameters	ZnO	$In_{0.4}Ga_{0.6}P$	$In_{0.5}Ga_{0.5}P$	GaAs	$Al_{0.4}$ G a_{06} As
Energy band gap, $E_g(eV)$	3.3	1.8936	1.802	1.42	1.716
Relative dielectric permittivity, ε_r	9	10.466	10.7033	12.9	11.764
Electron affinity, χ_{sc} (eV)	4	4.032	4.09	4.07	3.842

Effective density of state at E_C ,	5 × 10 ¹⁸	1.8×10^{19}	1.8×10^{19}	4.7×10^{17}	1.8×10^{19}
N _C (cm ⁻³) Effective density			1.9× 10 ¹⁹		
of state at E_V ,	10^{19}	1.9×10^{19}	2.0 / 1 / 20	9×10^{18}	1.9×10^{19}
N_V (cm^{-3})					
Electron mobility, μ_n	50	950	1125	8500	2800
$(cm^2V^{-1}s^{-1})$					
Hole mobility, $\mu_p (cm^2V^{-1}s^{-1})$	10	130	125	400	280
Density of N-type doping $N_d(cm^{-3})$	10 ²⁰	10 ²⁰	10 ²⁰	-	-
Density of P-type doping N_a	-	10 ²⁰	-	10^{17}	10 ²⁰
(cm^{-3})					
Electron life time, $\tau_n(s)$	10 ⁻⁷	10 ⁻⁷	10^{-7}	10^{-7}	10 ⁻⁷
Hole life time,	10^{-7}	10^{-7}	10^{-7}	10 ⁻⁷	10 ⁻⁷
$\tau_p(s)$					

III.4 Results and discussion

III.4.1 Single solar cell based on GaInP/GaAs heterojunction

Figures III.15, III.16 and III.17 display, respectively, the band gap diagram at thermal equilibrium, short circuit and open circuit conditions for the single solar cell based on GaInP/GaAs heterojunction. The variations in conduction band (E_C) and valence band (E_V) levels across the layers reflect the material properties and doping concentrations, with distinct band offsets at the interfaces. These offsets play a crucial role in reducing recombination and facilitating efficient charge transport. At thermal equilibrium, the Fermi level alignment throughout the device indicates energy equilibration and provides information on doping characteristics in the N^+ and P^+ regions. The presence of band bending signifies internal

electric fields at the junctions, which are essential for effective electron-hole pair separation and transport.

Under short-circuit conditions, the built-in voltage remains at V_d , as in thermal equilibrium, since no photo-carrier accumulation occurs at the cell edges. Consequently, the photo-bias voltage between the cell edges is zero, and the significant band bending observed at the depletion layer remains unchanged, consistent with thermal equilibrium. However, light absorption leads to photogeneration and an increase in carrier density within the device, causing the quasi-Fermi levels to split into E_{fn} for electrons and E_{fp} for holes. These changes enhance charge separation and charge carrier dynamics within the structure. As no photocarrier accumulation occurs at the cell edges, the resulting photocurrent reaches its maximum value, known as the short-circuit current density.

Under open-circuit conditions, photo-carrier accumulation at the cell edges reaches its maximum, meaning that charge photogeneration and separation occur without current flow. This leads to a greater splitting of the quasi-Fermi levels, E_{fn} and E_{fp} , indicating the generation of a significant photovoltage due to efficient photon absorption and charge carrier separation. As a result, the built-in voltage decreases relative to V_d due to the influence of the forward bias photovoltage, and the band bending at the depletion layer is significantly reduced.

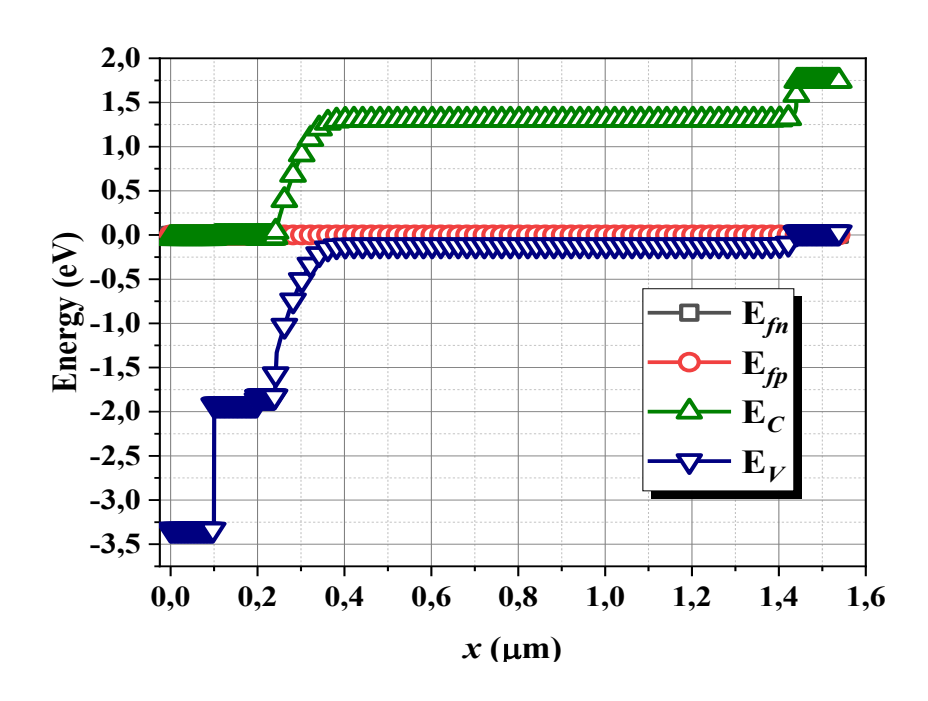


Figure III.15: Band gap diagram at thermal equilibrium for the single solar cell.

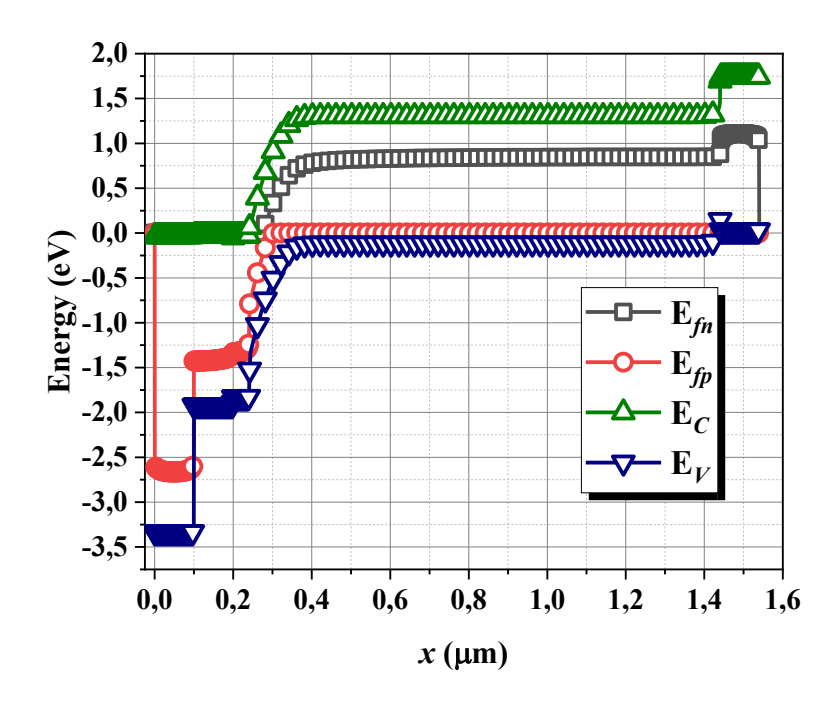


Figure III.16: Band gap diagram at short circuit conditions for the single solar cell

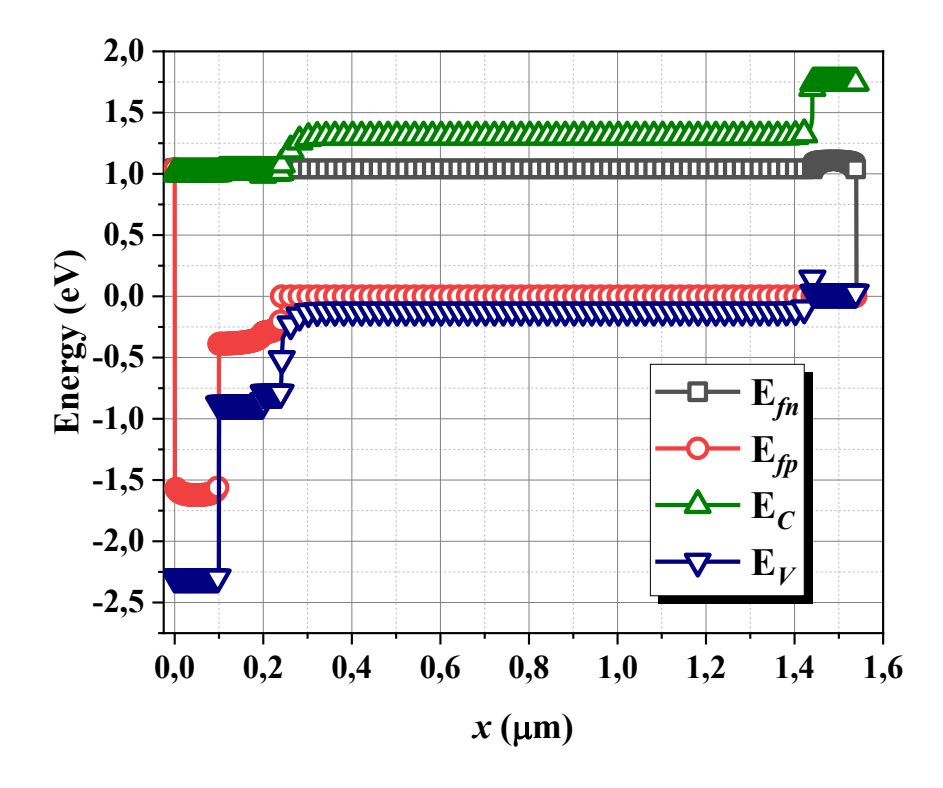


Figure III.17: Band gap diagram at open circuit conditions for the single solar cell.

Figure III.18 illustrates the distribution of free carrier densities (electrons and holes) within the solar cell under thermal equilibrium, short circuit, and open circuit conditions. At thermal equilibrium, the carrier densities are relatively stable and reflect the balance of intrinsic and dopant-induced carriers. Under short circuit conditions, a noticeable variation in carrier densities appears in regions where carriers are minorities, as well as near the depletion layer,

due to the photogeneration and carrier flow toward the contacts. Under the open circuit condition, the significant splitting of the quasi-Fermi levels results in pronounced carrier density variations, especially in regions where carriers are minorities, , as well as near the depletion layer, reflecting the establishment of a significant photovoltage. These observations highlight the dynamic behavior of charge carriers across different operational states, which is critical for understanding the solar cell's performance and efficiency.

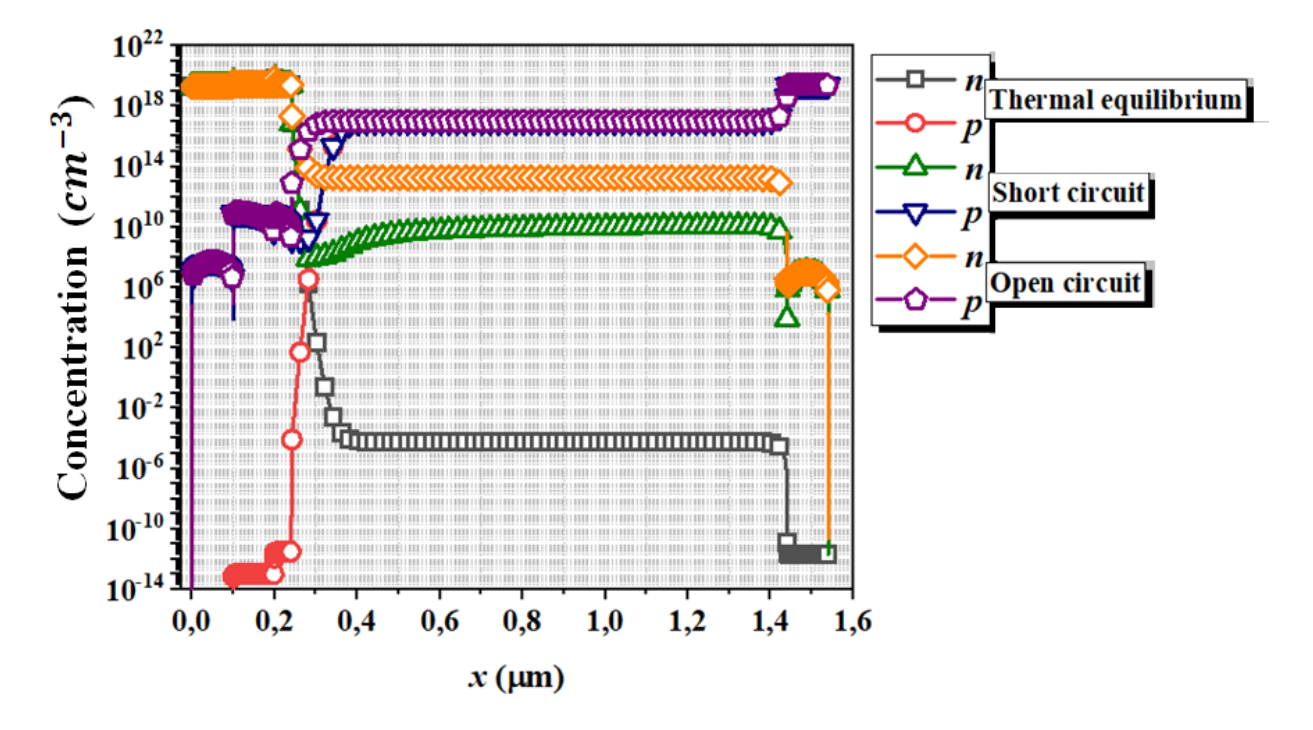


Figure III.18: Free carrier density distributions at thermal equilibrium, short and open circuit conditions for the single solar cell.

Figure III.19 displays the J-V and P-V electrical characteristics under the AM1.5 standard solar spectrum for the single solar cell. The J-V curve, characterized by its steep slope and high current density at lower voltages, indicates efficient carrier generation and collection, with a short-circuit current density (J_{sc}) of $29.227 \, mA/cm^2$ and an open-circuit voltage (V_{oc}) of $1.039 \, \text{V}$. The P-V curve reaches a peak power density (P_{max}) of $0.02671 \, W/cm^2$, demonstrating the solar cell's capability to convert sunlight into electrical power effectively. The fill factor (FF) of 87.58% shows a minimal series resistance effect and effective charge transport leading to an overall efficiency (E_{ff}) of 26.90%. These curves reflect the critical interplay between current, voltage, and power. The photovoltaic output parameters of the solar cell are also presented in Table III.3.

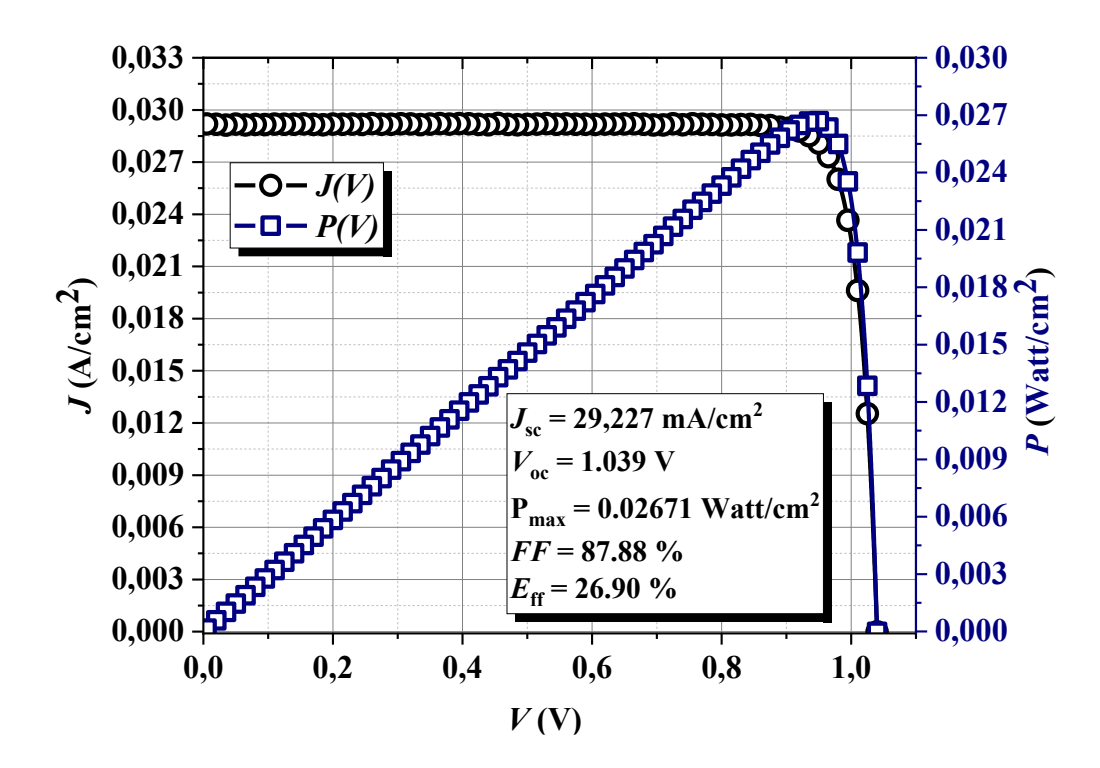


Figure III.19: J - V and P - V electrical characteristics under the AM1.5 standard solar spectrum for the single solar cell.

Table III.3: Photovoltaic output parameters of the single solar cell based on GaInP/GaAs heterojunction

	$J_{sc}(mA/cm^2)$	$V_{oc}(V)$	FF (%)	$P_{max} (W/cm^2)$	$E_{ff}(\%)$
Single solar cell					
based on	29.227	1.039	87.88	0.02671	26.90
GaInP/GaAs					
heterojunction					

III.4.2 Effect of thickness variation on the photovoltaic output parameters of the single solar cell based on GaInP/GaAs heterojunction

As shown on Figure III.20, varying the thickness of the N⁺-type ZnO layer (first layer) from 0.01 μ m to 0.5 μ m has no discernible effect on the key output photo-parameters, including J_{sc} , V_{oc} , FF, and E_{ff} . Each parameter remains relatively constant across this range, indicating that the thickness of the N⁺-type ZnO layer does not play a critical role in determining the photovoltaic performance of the cell under the AM1.5 standard solar spectrum. This stability suggests that the optical and electrical properties of the ZnO layer are sufficient to maintain consistent solar cell performance within the given thickness range.

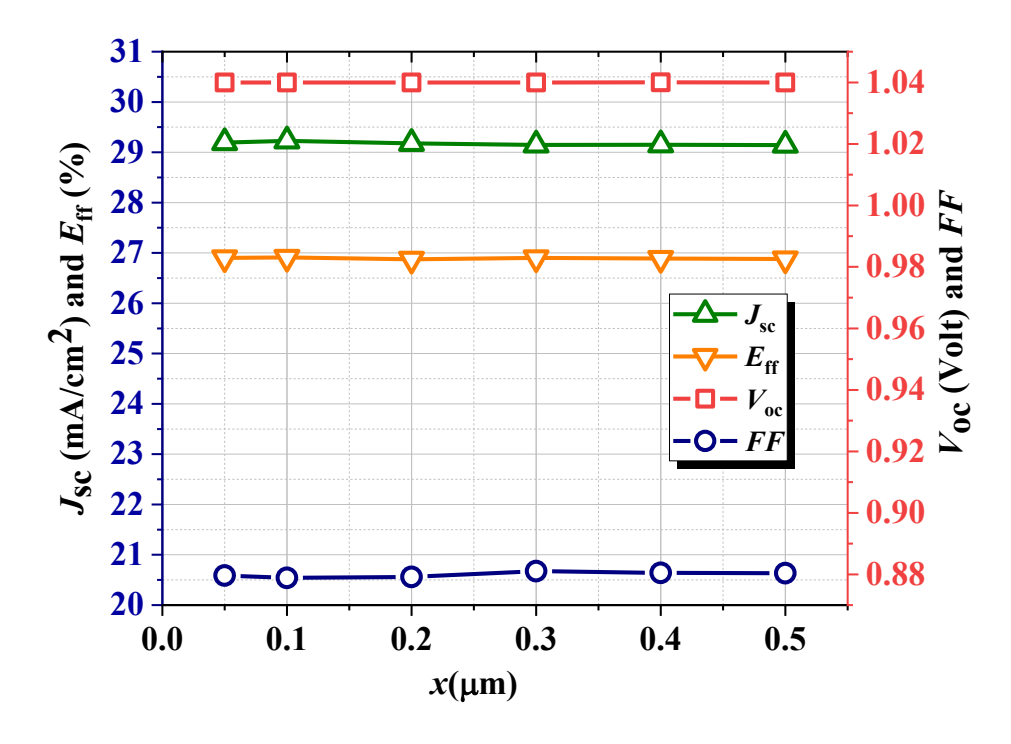


Figure III.20: Dependence of photovoltaic output parameters on the thickness of the N⁺-type ZnO layer in the single solar cell.

Figure III.21 shows the thickness variation effect of the N⁺-type $In_{0.4}Ga_{0.6}P$ layer (second layer) on : (a) I - V characteristics and (b) photovoltaic output parameters of the single solar cell. Increasing the thickness of the N⁺-type I $n_{0.4}$ G $a_{0.6}$ P layer within the range [0.01 μ m - 0.5 μ m] significantly affects the I-V characteristics of the cell (Figure III.21 (a)), leading to a notable reduction in current density. This decline indicates a reduced ability of the active layer to absorb photons and convert them into charge carriers, or increased carrier losses due to recombination. The curves show that the highest current is achieved at the smallest thickness (0.01 µm), and it decreases progressively with increasing thickness, suggesting that excessive thickness weakens photo-collection efficiency. Figure III.21 (b) and Table III.4 further display a substantial reduction in J_{sc} , which directly diminishes the cell's conversion efficiency (E_{ff}) from 27.15% to 20.88%, while V_{oc} shows a slight decrease and FF remains relatively stable. This implies that the efficiency variations are mainly due to changes in J_{sc} , rather than FF, and thinner layers of In_{0.4}Ga_{0.6}P are more effective in enhancing the solar cell's performance. These observations underline the critical role of the N⁺-type $In_{0.4}Ga_{0.6}P$ layer's thickness in optimizing charge transport and maintaining high photovoltaic efficiency, highlighting the necessity of precise thickness calibration for this layer.

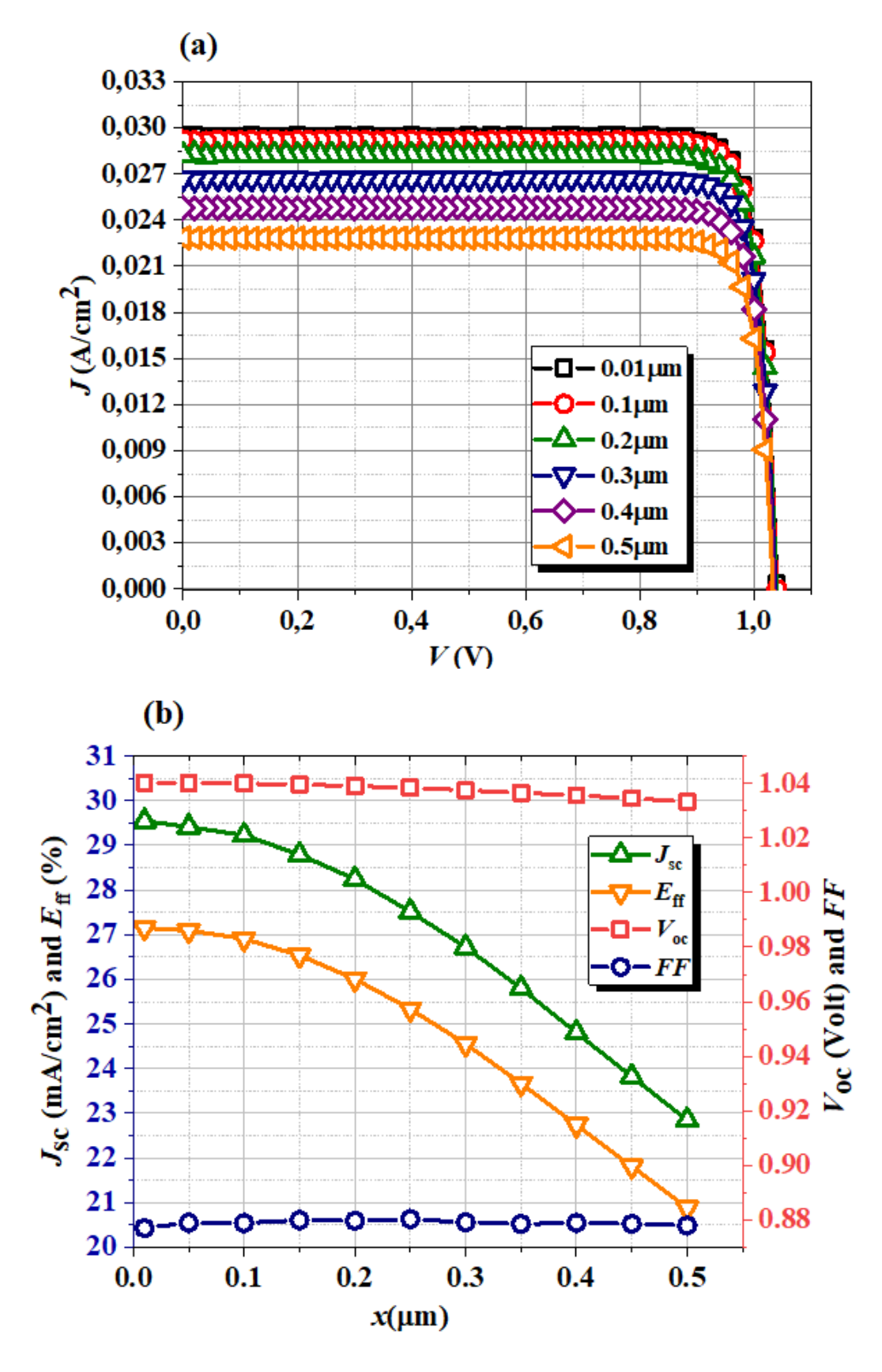
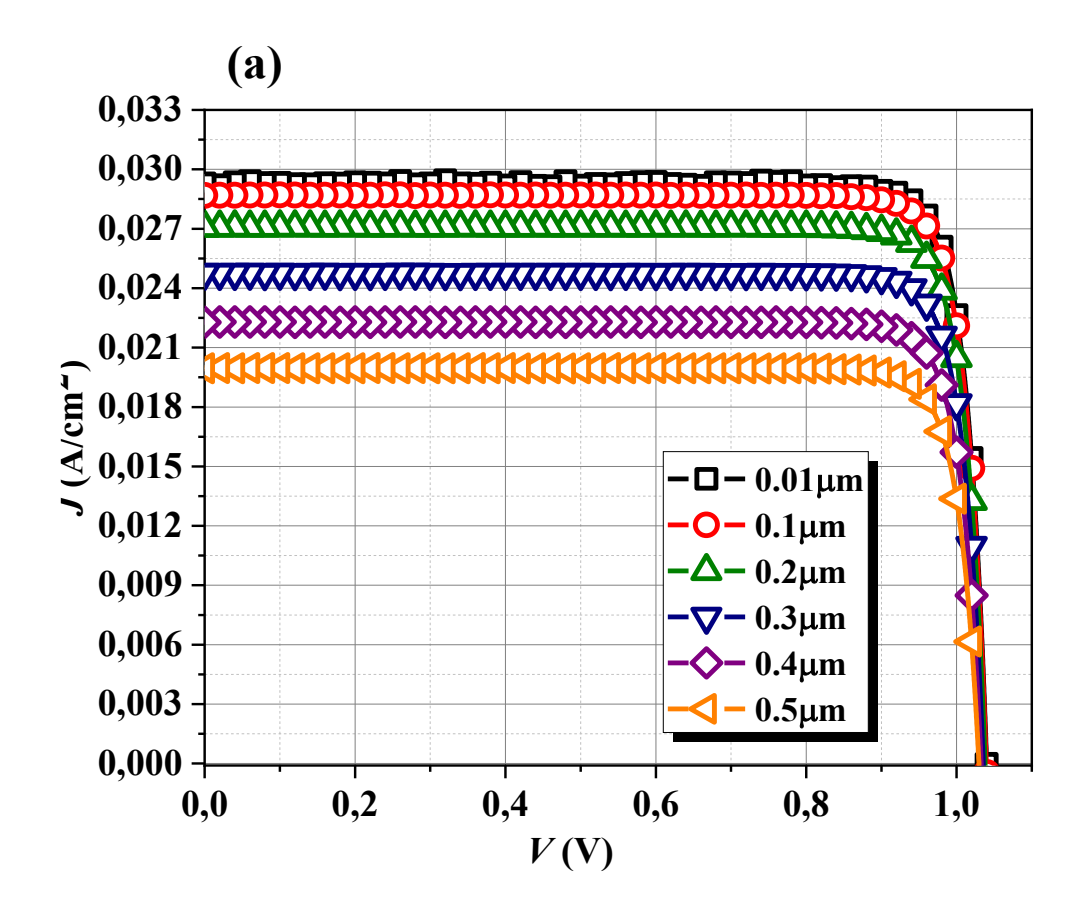


Figure III.21: Thickness variation effect of the N⁺-type $In_{0.4}Ga_{0.6}P$ layer on: (a) J-V characteristics and (b) photovoltaic output parameters of the single solar cell.

Table III.4: Dependence of photovoltaic output parameters on the thickness of the N⁺-type $In_{0.4}Ga_{0.6}P$ layer in the single solar cell.

Thickness (µm)	$J_{sc}(\text{mA}/cm^2)$	$V_{oc}(V)$	FF (%)	$P_{max} (W/cm^2)$	$E_{ff}(\%)$
0.01	29.545	1.040	87.70	0.02695	27.15
0.1	29.227	1.039	87.88	0.02671	26.90
0.2	28.246	1.039	87.96	0.02581	26.00
0.3	26.721	1.037	87.91	0.02437	24.55
0.4	24.804	1.035	87.89	0.02257	22.74
0.5	22.849	1.033	87.79	0.20072	20.88

Figure III.22 highlights the significant impact of varying the thickness of the third layer, composed of N⁺-type I $n_{0.5}$ G $a_{0.5}$ P, from 0.01 μ m to 0.5 μ m, on the solar cell's performance.



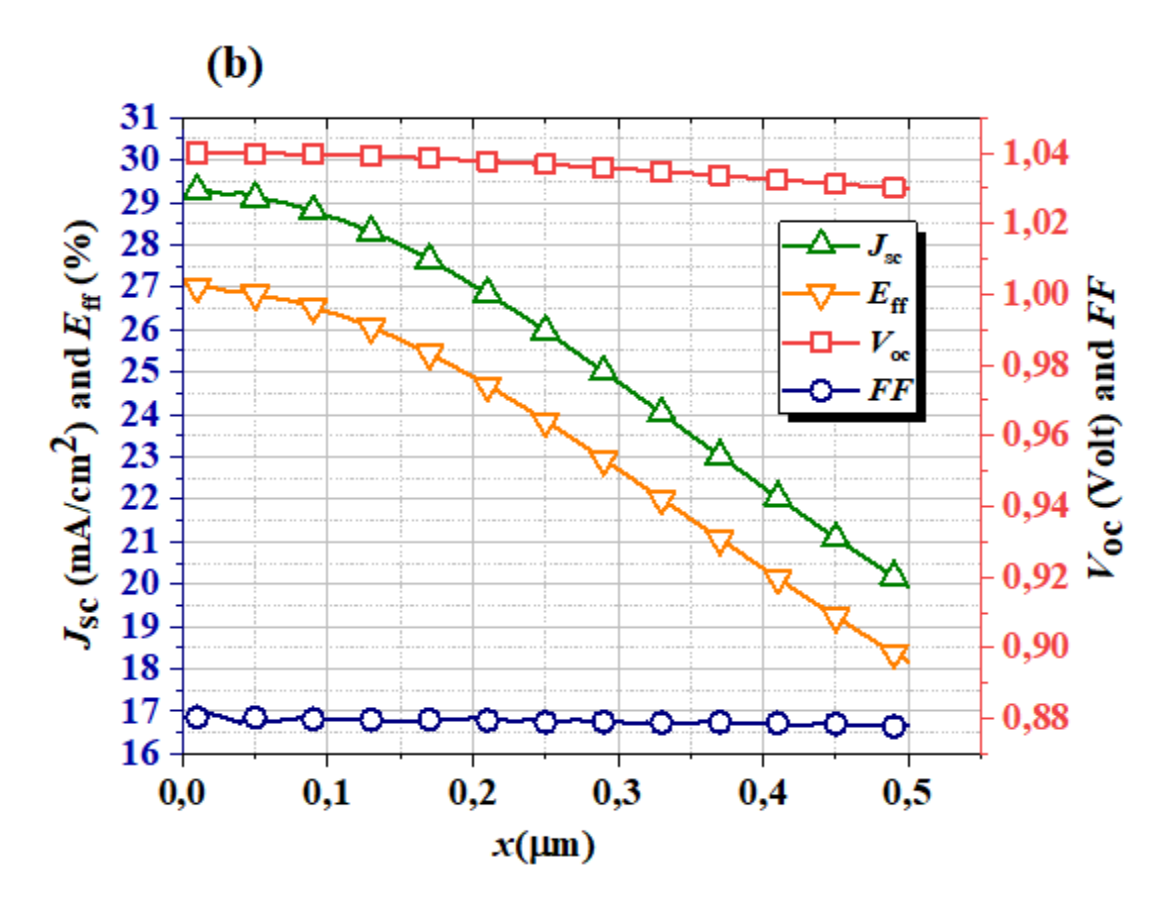


Figure III.22: Thickness variation effect of the N⁺-type $In_{0.5}Ga_{0.5}P$ layer on: (a) J-V characteristics and (b) photovoltaic output parameters of the single solar cell.

In particular, Figure III.22 (a) reveals a clear decline in current density across the J-V characteristics as the layer thickness increases. The highest current density is achieved at the minimal thickness of 0.01 μ m, after which it gradually diminishes with increasing thickness. This reduction signifies a decline in charge carrier transport efficiency, attributed to diminished photon absorption and an increase in carrier recombination phenomena. These factors collectively limit the generation of photogenerated carriers, eventually confirming that excessive layer thickness deteriorates photo-collection efficiency.

Complementary, Figure III.22 (b) and Table III.5 illustrate a significant decline in the short-circuit current density (J_{sc}) , which directly contributes to a reduction in the solar cell's conversion efficiency (E_{ff}) from 27.01% to 18.17%. Meanwhile, the open-circuit voltage (V_{oc}) exhibits only a slight decrease, while the fill factor FF remains nearly unchanged. This indicates that variations in efficiency are predominantly influenced by changes in J_{sc} rather than FF, reinforcing the conclusion that thinner layers of $In_{0.5}Ga_{0.5}P$ are more beneficial for improving solar cell performance. These findings suggest that increased layer thickness imposes

limitations on carrier collection, underlining the importance of precisely optimizing this parameter to maximize photovoltaic efficiency.

Table III.5: Dependence of photovoltaic output parameters on the thickness of the N⁺-type $In_{0.5}Ga_{0.5}P$ layer in the single solar cell.

Thickness (µm)	$J_{sc}(\text{mA}/cm^2)$	$V_{oc}(V)$	FF (%)	$P_{max} (W/cm^2)$	$E_{ff}(\%)$
0.01	29.292	1.039	88.03	0.02681	27.01
0.1	28.675	1.039	87.99	0.02623	26.42
0.2	27.051	1.037	88.02	0.02471	24.89
0.3	24.772	1.035	87.89	0.02254	22.71
0.4	22.283	1.032	87.87	0.02022	20.37
0.5	19.95	1.029	87.82	0.01804	18.17

Figures III.23 (a) and (b), together with table III.6, illustrate the profound impact of increasing the thickness of the fourth layer, composed of P-type GaAs, which serves as the base layer of the solar cell. As the thickness increases from 0.1 μ m to 3.5 μ m, there is a clear enhancement in J_{sc} , leading to a significant improvement in the cell's conversion efficiency (E_{ff}) from 18.23% to 28.68%. This increase can be attributed to the fact that the P-type GaAs layer is the primary region where optical absorption occurs, generating a larger number of electronhole pairs with thicker layers. The enhanced photogeneration of carriers increases J_{sc} , improving the overall efficiency despite a slight reduction in open-circuit voltage (V_{oc}), which could result from increased recombination losses or altered electric field distributions. The stability of the fill factor (FF) across these thicknesses indicates that the cell's capacity to effectively convert absorbed light into electrical power remains consistent, and the thickness effect primarily impacts light absorption and current generation rather than internal resistance. These results underscore the critical role of the P-type GaAs layer in determining the cell's optical and electrical properties, highlighting the importance of optimizing its thickness to balance absorption and carrier collection for maximum photovoltaic performance.

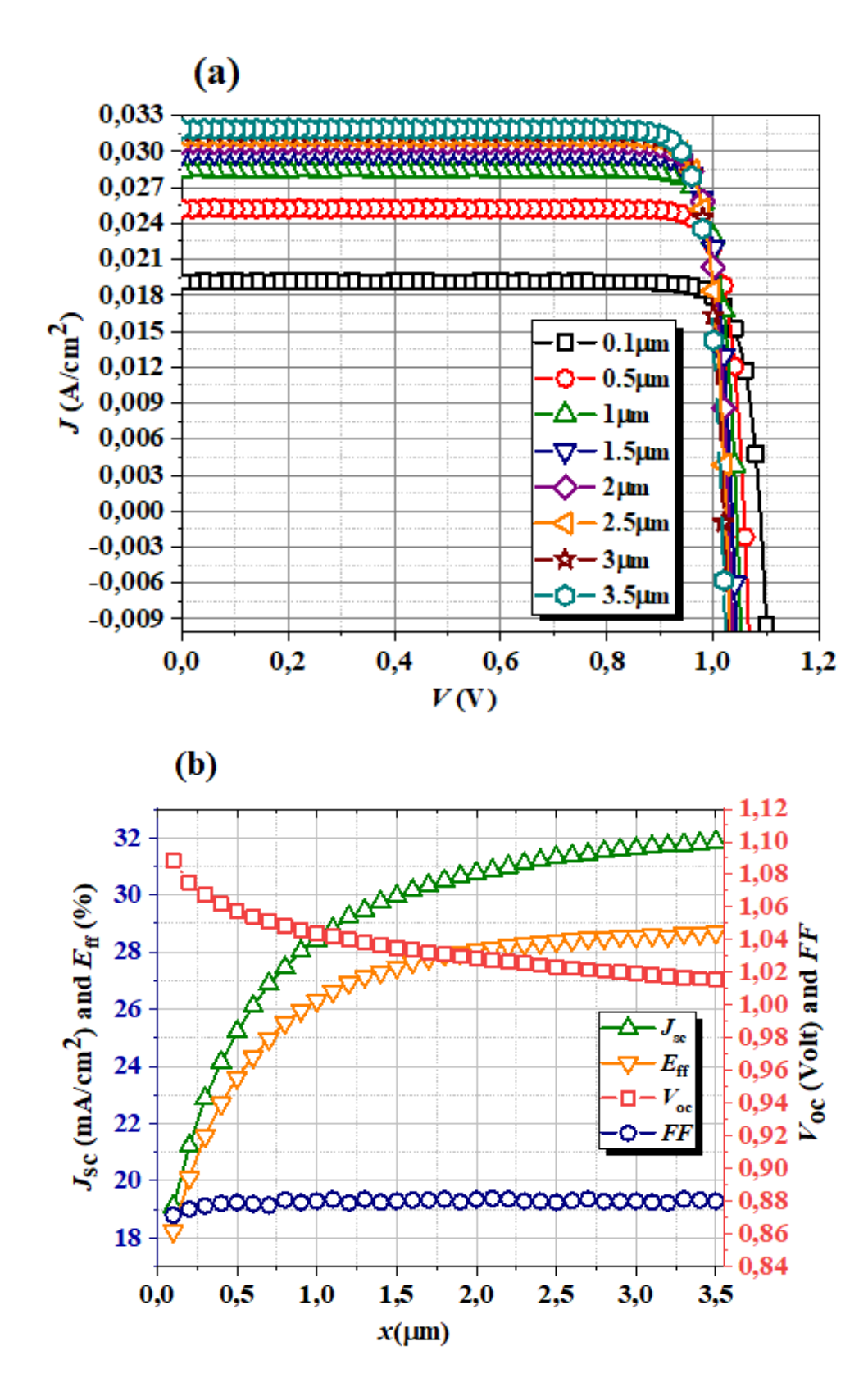


Figure III.23: Thickness variation effect of the P-type GaAs layer on: (a) J - V characteristics and (b) photovoltaic output parameters of the single solar cell.

Table III.6: Dependence of photovoltaic output parameters on the thickness of the P-type GaAs layer in the single solar cell.

Thickness (µm)	$J_{sc}(\text{mA}/cm^2)$	$V_{oc}(V)$	FF (%)	$P_{max} (W/cm^2)$	$E_{ff}(\%)$
0.1	19.094	1.088	87.13	0.01810	18.23
0.5	25.210	1.057	87.91	0.02367	23.61
1	28.423	1.043	88.00	0.02611	26.30
1.5	29.944	1.035	88.00	0.02727	27.47
2	30.764	1.028	88.10	0.02787	28.08
2.5	31.304	1.023	87.92	0.02816	28.37
3	31.610	1.019	87.99	0.02834	28.55
3.5	31.860	1.015	87.99	0.02847	28.68

Figure III.24 demonstrates that varying the thickness of the fifth (last) layer, composed of P^+ -type $\mathrm{Al}_{0.4}\mathrm{Ga}_{0.6}\mathrm{As}$, has no discernible effect on the output photo-parameters of the solar cell, including the J_{sc} , V_{oc} , FF, and E_{ff} ..

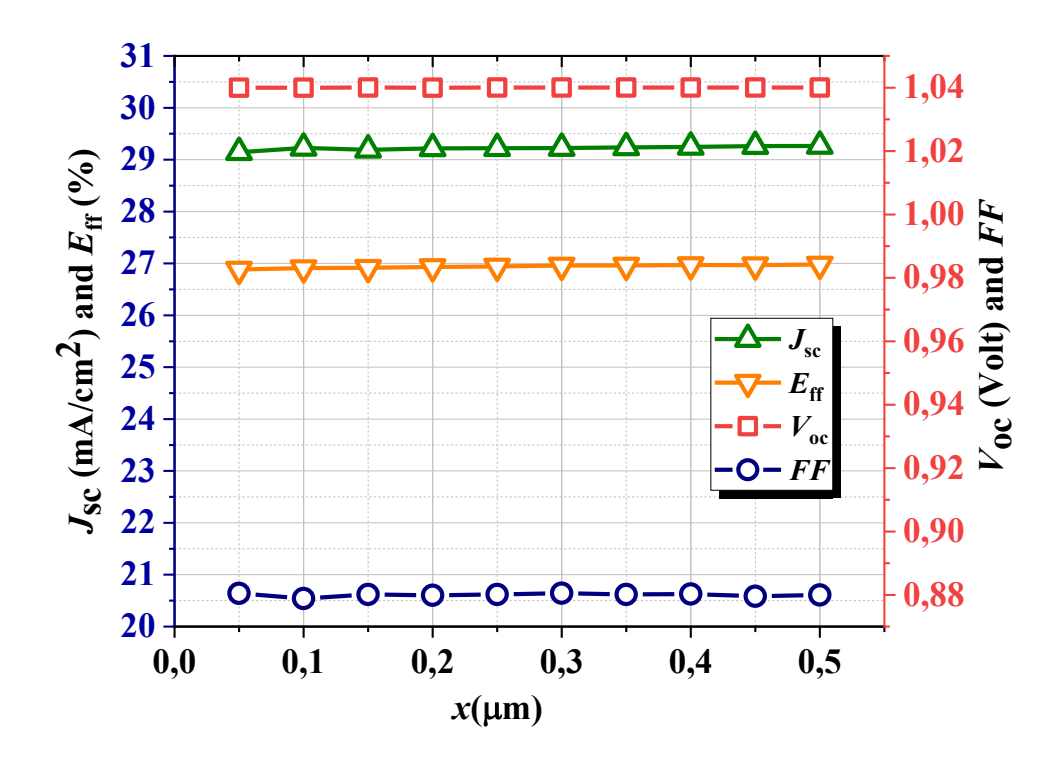


Figure III.24: Dependence of photovoltaic output parameters on the thickness of the P^+ -type $Al_{0.4}Ga_{0.6}As$ layer in the single solar cell.

This invariance can be attributed to the role of the P^+ -type $Al_{0.4}Ga_{0.6}As$ layer within the cell. As the heavily doped lowest layer, its primary function is to facilitate hole collection at the back

contact and improve overall junction stability rather than contribute significantly to optical absorption or carrier generation. Since this layer is positioned at the bottom of the cell and does not interact substantially with the incident light, increasing its thickness does not enhance photogeneration or absorption. Furthermore, its electrical properties, such as conductivity, are sufficiently optimized at minimal thickness, ensuring consistent performance regardless of further thickness increments. Thus, the cell's design minimizes the influence of this layer's dimensions on the critical output parameters.

III.4.3 Effect of doping variation on the photovoltaic output parameters of the single solar cell based on GaInP/GaAs heterojunction

Figures III.25 and III.26 display, respectively, the dependence of the single solar cell output photo-parameters on the donor doping concentration (N_d) in the second layer (of N*-type I $n_{0.4}Ga_{0.6}P$) and in the third layer (of the N*-type I $n_{0.5}Ga_{0.5}P$). Decreasing the doping concentration from 10^{20} cm $^{-3}$ to 10^{15} cm $^{-3}$ in the emitter layers, including the second and third layers, has no discernible effect on the output photo-parameters of the solar cell. The invariance of key parameters including the J_{sc} , V_{oc} , FF, and E_{ff} across this wide range of doping concentrations suggests that the emitter layers' doping level is not a critical factor in determining the solar cell's overall performance. This behavior can be explained by the sufficient carrier transport and collection mechanisms already established within the emitter layers at lower doping concentrations, alongside the negligible influence of higher doping levels on the optical absorption and carrier generation processes. The emitter layers effectively fulfill their roles in facilitating carrier flow and maintaining device efficiency regardless of doping concentration adjustments.

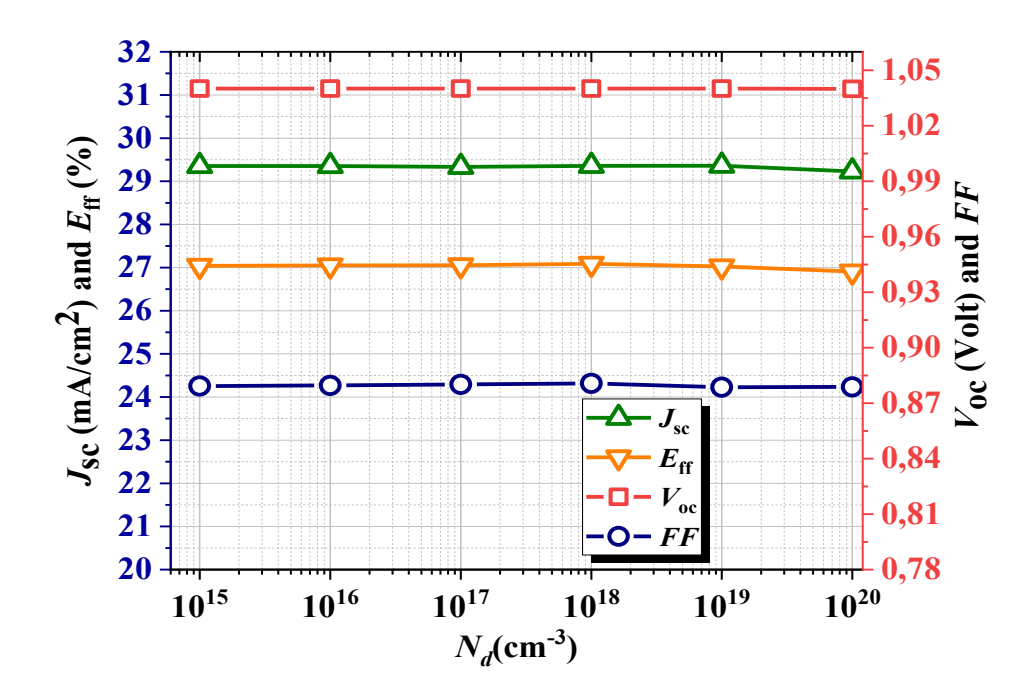


Figure III.25: Dependence of photovoltaic output parameters on the donor doping concentration (N_d) of the N⁺-type I $n_{0.4}$ G $a_{0.6}$ P layer in the single solar cell.

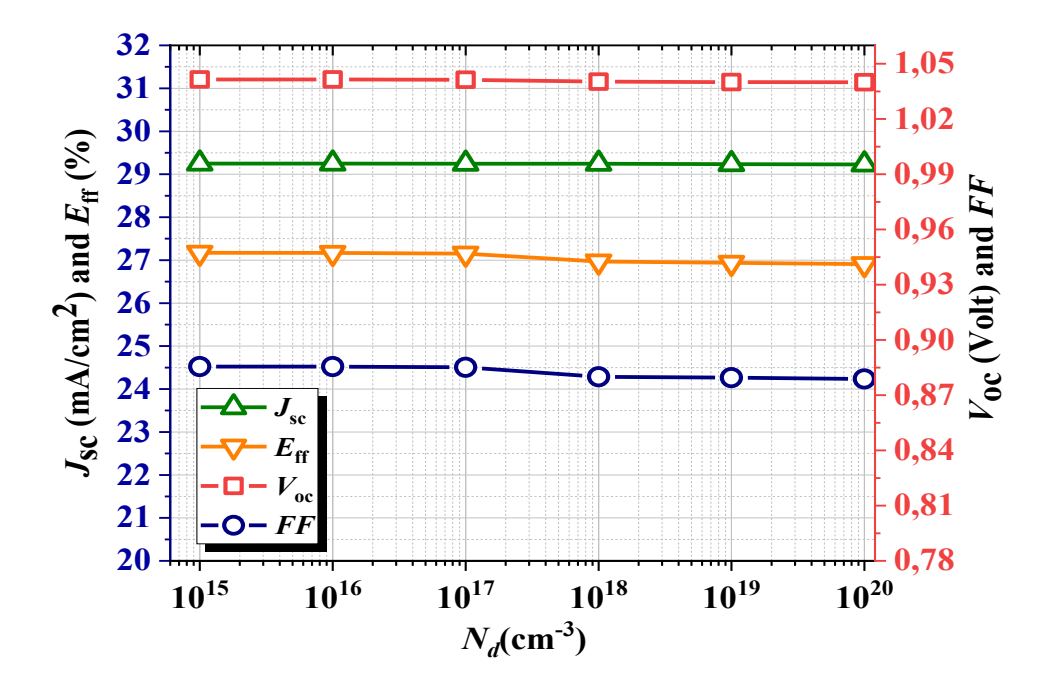
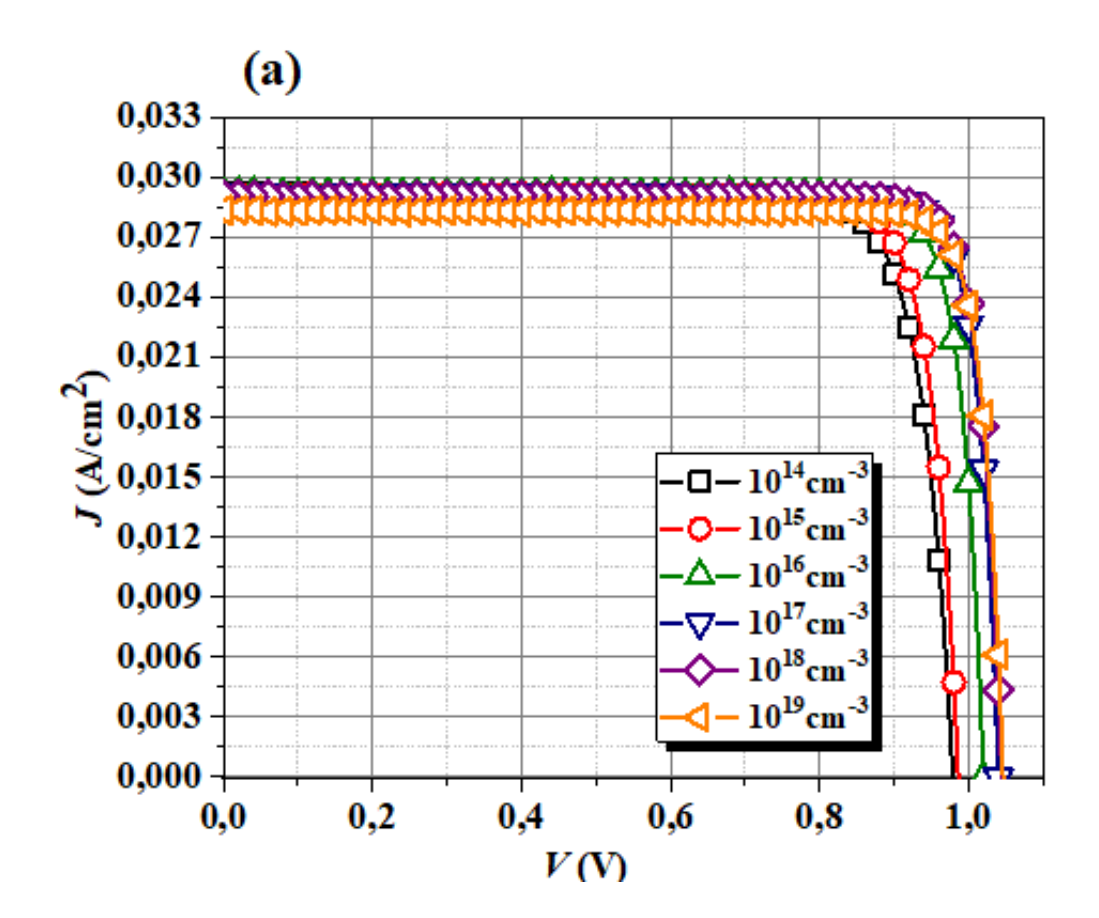


Figure III.26: Dependence of photovoltaic output parameters on the donor doping concentration (N_d) of the N⁺-type I $n_{0.5}$ G $a_{0.5}$ P layer in the single solar cell.

Figure III.27 illustrates the influence of varying the doping concentration (N_a) of the P-type GaAs layer (fourth layer), on: (a) J - V characteristics and (b) photovoltaic output parameters, within the range of 10^{14} cm⁻³ to 10^{19} cm⁻³. As the doping concentration increases, the photocurrent and then J_{sc} exhibit a slight decline, primarily due to elevated recombination rates

at higher carrier densities, which delay the effective collection of photogenerated carriers. In contrast, V_{oc} and FF steadily improve, likely as a result of enhanced electrical conductivity and stronger electric fields that facilitate better carrier separation. Additionally, higher doping levels can reduce resistive losses, thus contributing to an improved FF. Moreover, increasing the P-type doping concentration in the GaAs base layer reduces the dark saturation current, as the latter is inversely related to the doping concentration. Since V_{oc} is inversely proportional to the saturation current, its reduction leads to a corresponding increase in V_{oc} . These combined effects drive an increase in the conversion efficiency (E_{ff}) up to a peak of 27.01% observed at a doping concentration of $10^{18} \ cm^{-3}$ as shown in Table III.7. Beyond this threshold, efficiency begins to decline, as the opposing effects of sensitive recombination surpass the advantages of improved conductivity and field strength. This behavior underlines the dual role of the P-type GaAs layer as both the primary region for optical absorption and photogenerated carrier collection, highlighting the critical importance of optimizing its doping concentration to achieve the best photovoltaic performance.



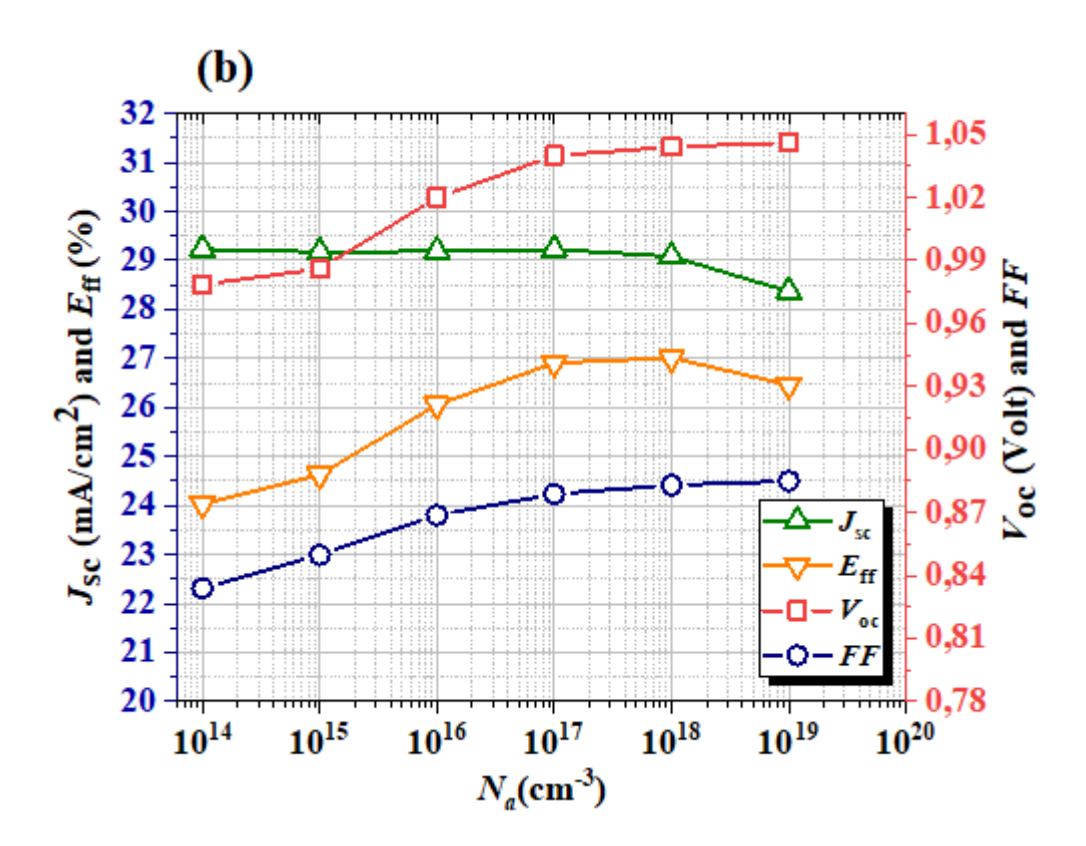


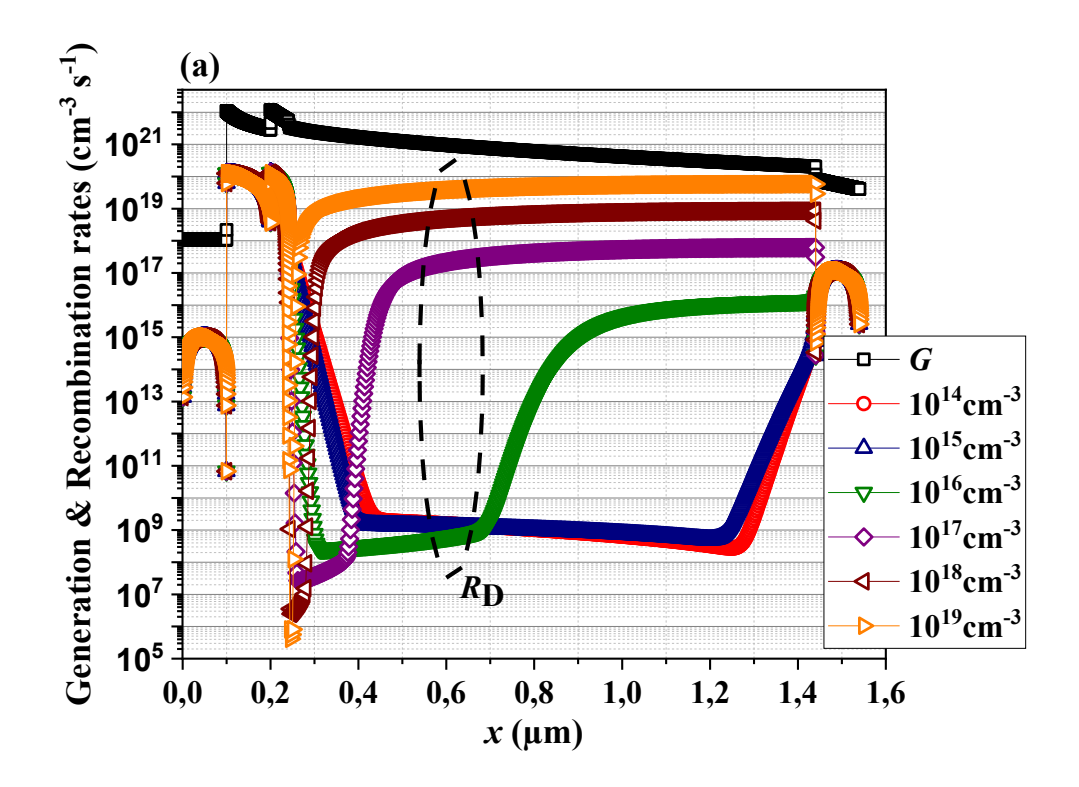
Figure III.27: Effect of the acceptor doping concentration (N_a) of the P-type GaAs layer on: (a) J - V characteristics and (b) photovoltaic output parameters of the single solar cell.

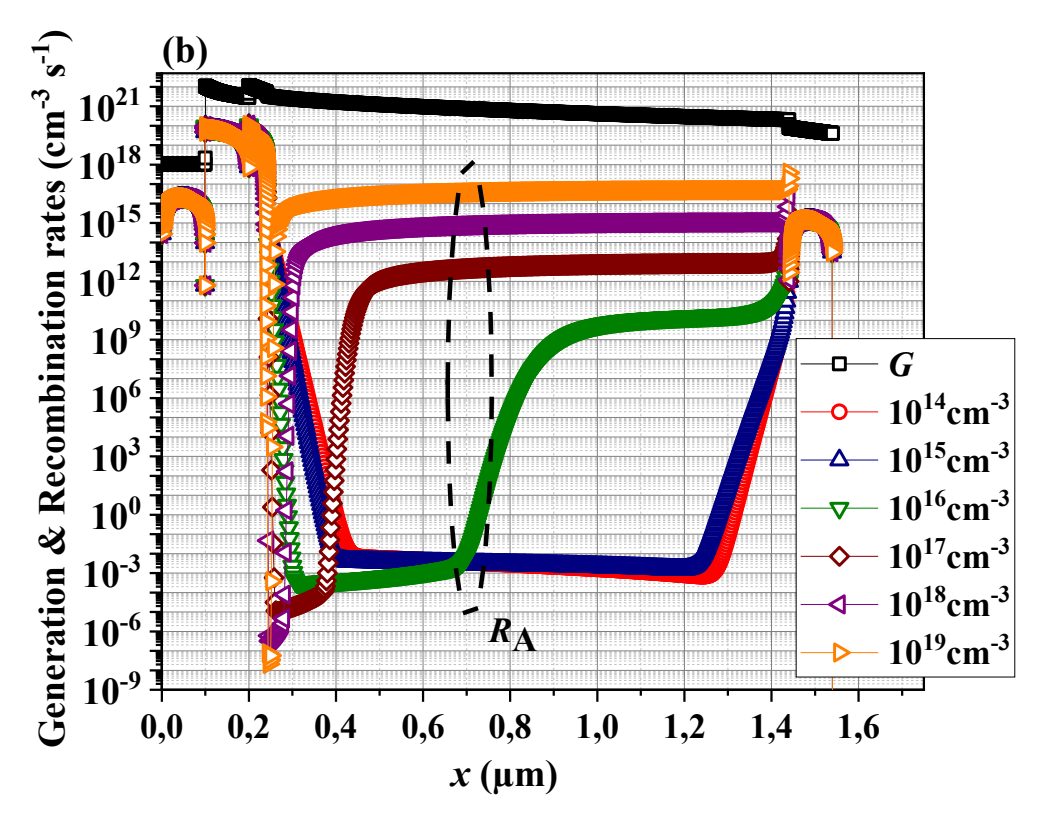
Table III.7: Dependence of photovoltaic output parameters on the acceptor doping concentration (N_a) of the P-type GaAs layer in the single solar cell.

Doping concentration (cm^{-3})	$J_{sc}(\text{mA}/cm^2)$	$V_{oc}(\mathbf{V})$	FF (%)	$P_{max} (W/cm^2)$	$E_{ff}(\%)$
10 ¹⁴	29.231	0.978	83.38	0.02385	24.02
10 ¹⁵	29.174	0.986	84.98	0.02444	24.62
10 ¹⁶	29.192	1.019	86.87	0.025860	26.05
10 ¹⁷	29.227	1.039	87.88	0.02670	26.90
10 ¹⁸	29.083	1.044	88.29	0.02681	27.01
10 ¹⁹	28.371	1.046	88.499	0.02626	26.46

Increasing the P-type doping concentration in the GaAs base layer significantly amplifies recombination rates as shown in Figure III.28, where cases (a), (b) and (c) display, respectively, the distribution of the direct (radiative) recombination rate (R_D), the Auger recombination rate

 (R_A) and the Shockley-Read-Hall recombination rate (R_{SRH}) . The optical generation rate (G) is also presented.





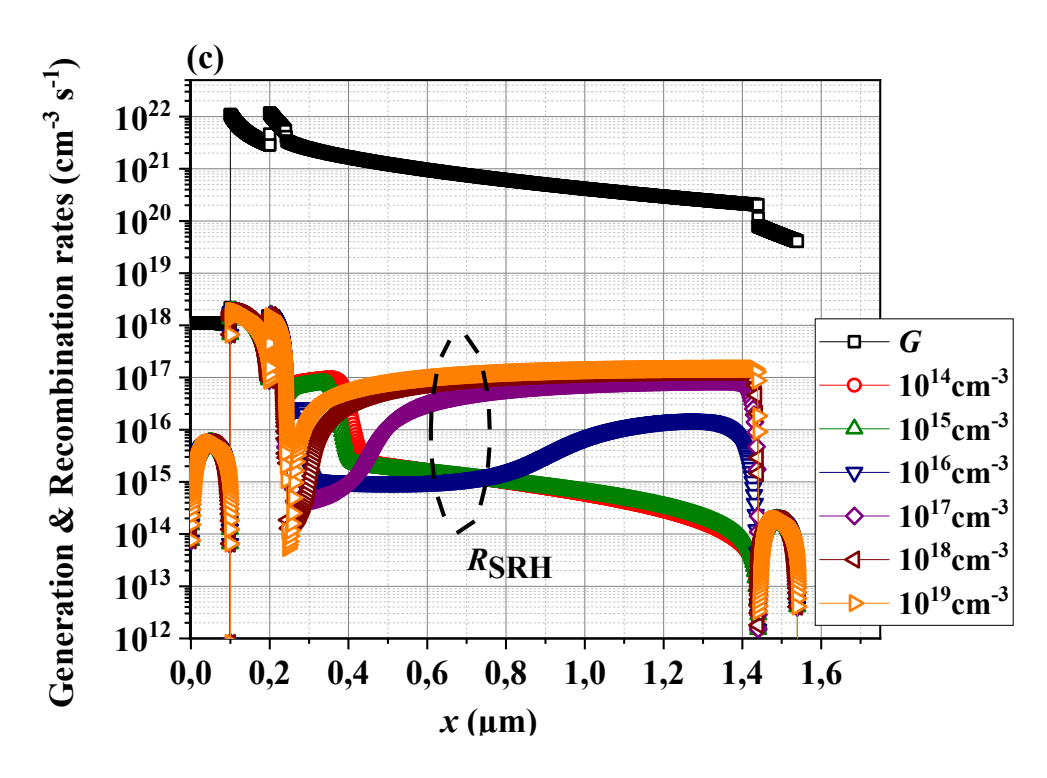


Figure III.28: Effect of the P-type doping concentration in the GaAs base layer on the distribution of: (a) the direct (radiative) recombination rate (R_D) , (b) the Auger recombination rate (R_A) and (c) the Shockley-Read-Hall recombination rate (R_{SRH}) .

Higher doping introduces more acceptor atoms, which increases the concentration of holes—the majority carriers—thereby raising the probability of recombination as the minority electrons encounter holes more frequently. This process reduces the minority carrier lifetime, as scattering and trapping events become more pronounced at elevated carrier densities. Additionally, at high doping levels, Auger recombination becomes significant; this non-radiative mechanism involves energy transfer to another carrier, effectively removing charge carriers from contributing to the current. Higher doping can also introduce defects or impurities in the crystal lattice, serving as recombination centers that accelerate carrier annihilation.

Figure III.29 reveals that varying the p-type doping concentration in the fifth layer, composed of $Al_{0.4}Ga_{0.6}As$, from $10^{15}\ cm^{-3}$ to $10^{20}\ cm^{-3}$ has no discernible impact on the solar cell's output photo-parameters, including J_{sc} , V_{oc} , FF, and E_{ff} . This invariance can be attributed to the specific role of the $Al_{0.4}Ga_{0.6}As$ layer within the cell structure. As a heavily doped P^+ layer, its primary purpose is to serve as a cover layer that facilitates hole collection at the back contact and enhances the stability of the junction. Unlike the active regions such as the base layer or emitter, this layer does not contribute significantly to optical absorption or photogenerated

carrier dynamics. Furthermore, its electrical properties, such as conductivity and band alignment, are already optimized at relatively low doping concentrations, ensuring consistent performance even as the doping level increases. Consequently, variations in the doping concentration of this layer have no substantial influence on the cell's overall photovoltaic behavior.

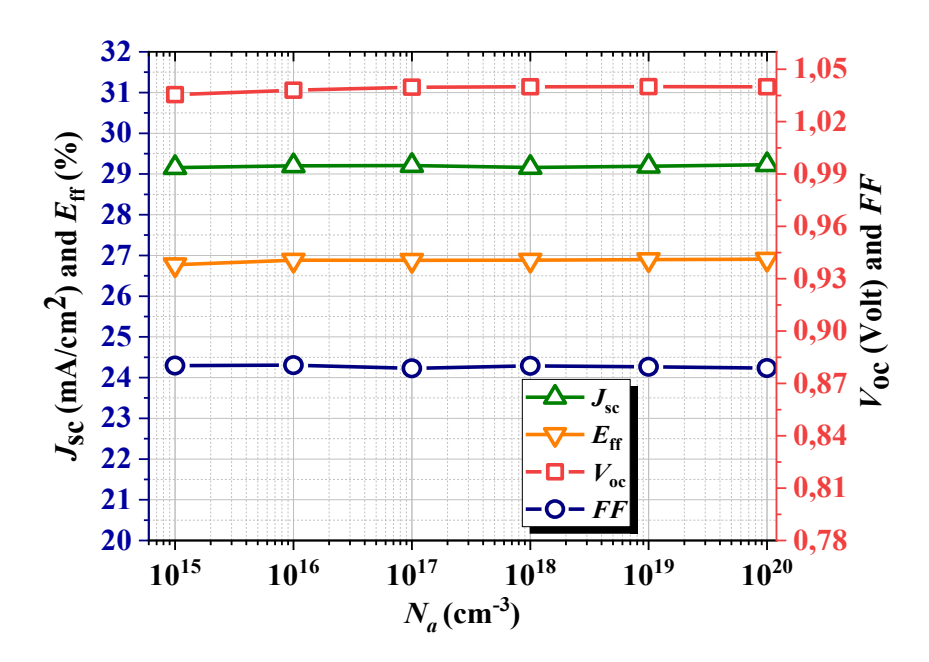


Figure III.29: Dependence of photovoltaic output parameters on the acceptor doping concentration (N_a) of the P⁺-type $Al_{0.4}Ga_{0.6}As$ layer in the single solar cell.

The optimization of the single solar cell based on the GaInP/GaAs heterojunction can be achieved by reducing the thickness of the second and third layers to the minimum possible value of 0.01 μ m, while increasing the thickness of the base layer (fourth layer) to 3.5 μ m and doping it with $N_a = 10^{17} cm^{-3}$. This configuration yields impressive output photo-parameters, including an efficiency (E_{ff}) of 29.088%, J_{sc} of 32.29 mA/ cm^2 , V_{oc} of 1.0158 V, and FF of 88.032%. This optimized structure provides a conversion efficiency value close to 29.1 % stated in recent researches [10, 11].

III.4.4 Tandem solar cell based on GaInP/GaAs heterojunction

The tandem solar cell, based on the GaInP/GaAs heterojunction, consists of a top sub-cell and a bottom sub-cell connected via a tunnel junction, as previously described in Section III.3. This configuration enhances solar energy conversion efficiency by allowing the top sub-cell, with its wide bandgap (E_g), to absorb high-energy photons, while the bottom sub-cell captures

lower-energy wavelengths, thereby optimizing utilization of the solar spectrum. The energetic band diagrams of the tandem solar cell are presented in Figures III.30, III.31, and III.32, corresponding to thermal equilibrium, short-circuit, and open-circuit conditions.

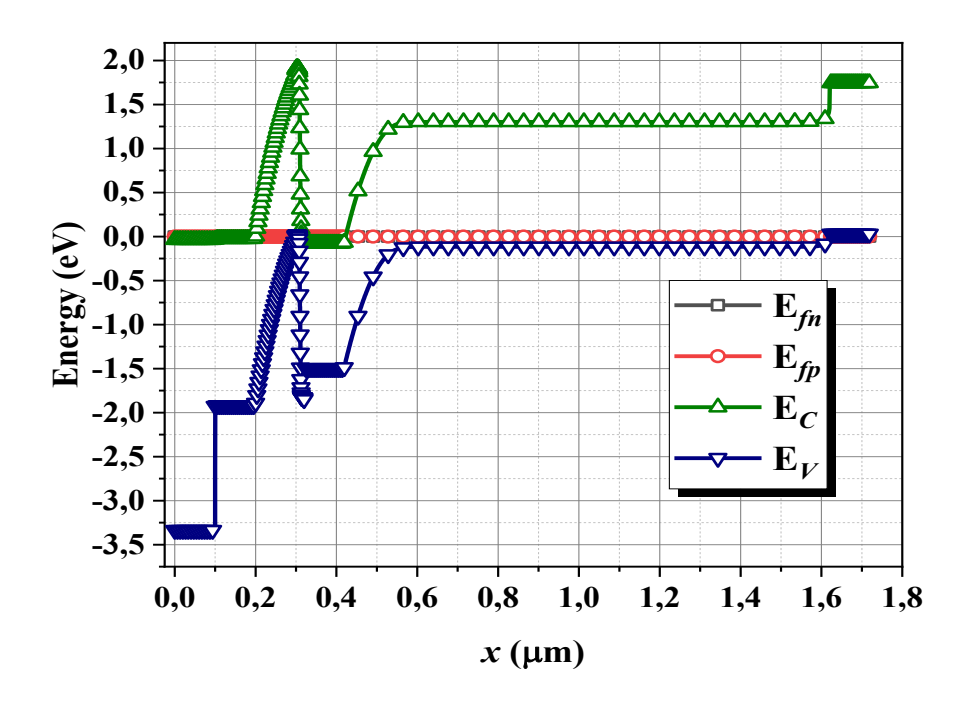


Figure III.30: Energetic band gap diagram at thermal equilibrium of the tandem solar cell based on GaInP/GaAs heterojunction.

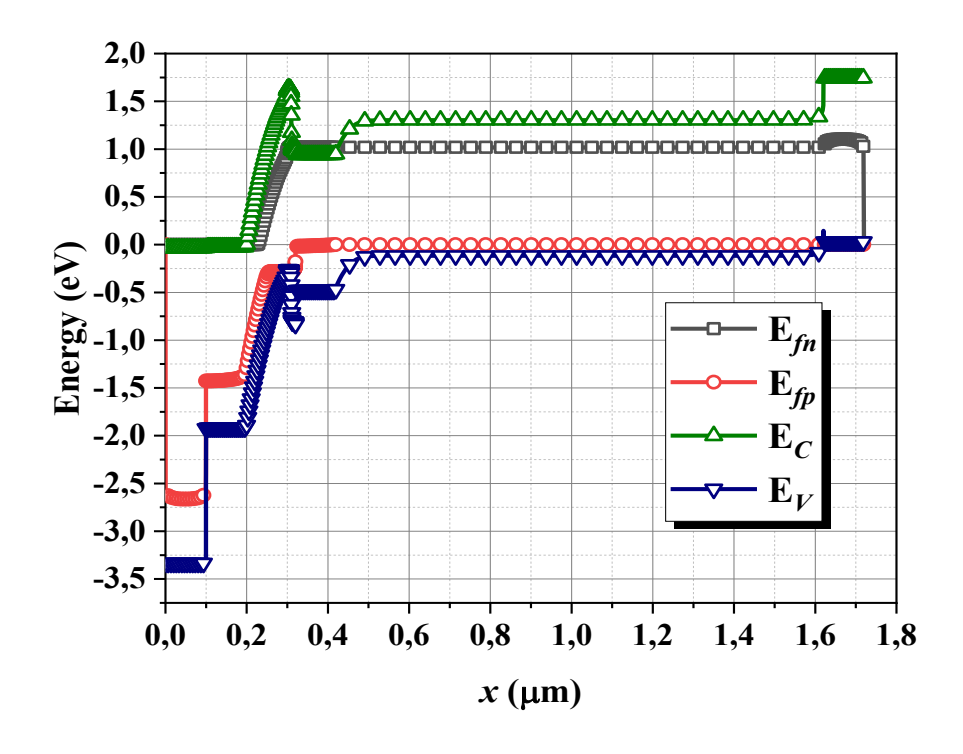


Figure III.31: Energetic band gap diagram at short circuit conditions of the tandem solar cell based on GaInP/GaAs heterojunction.

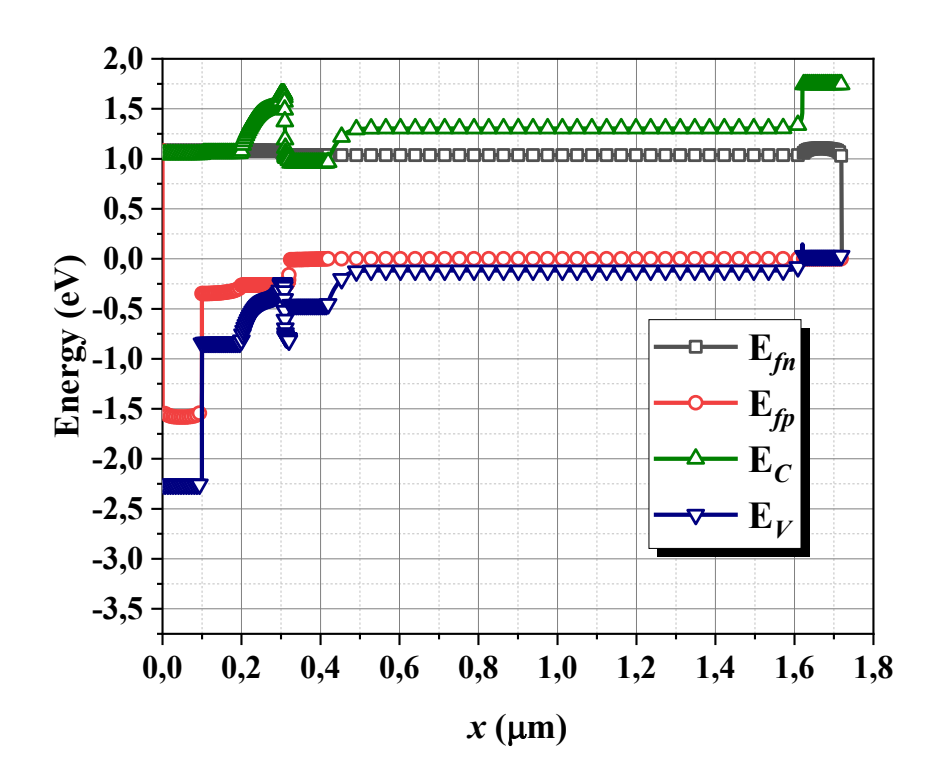


Figure III.32: Energetic band gap diagram at open circuit conditions of the tandem solar cell based on GaInP/GaAs heterojunction.

These diagrams highlight the conduction band edge (E_C) , valence band edge (E_V) , and quasi-Fermi levels (E_{fn} for electrons and E_{fp} for holes), which are crucial for carrier transport and junction behaviour. The tunnel junction, composed of highly doped P*-type ${\rm I}n_{0.4}{\rm G}a_{0.6}{\rm P}$ and N⁺-type $In_{0.5}Ga_{0.5}P$, ensures efficient charge transfer between sub-cells while minimizing resistive losses. Under thermal equilibrium, strong band bending is observed within the P-type $In_{0.4}Ga_{0.6}P$ base layer of the top sub-cell, and the P-type GaAs base layer of the bottom sub-cell, identifying them as the primary regions where depletion layers are established. The Fermi level alignment throughout the device reflects the equilibrium condition maintained under thermal equilibrium, ensuring structural stability while optimizing charge extraction. In this state, the Fermi level remains constant across all materials, indicating no charge carrier flow, with electron density being higher in N-type regions, while hole density is higher in P-type regions. The diagram also highlights the variation in band gaps between different semiconductor materials, where GaInP layers possess a larger band gap compared to GaAs layers, creating energy barriers that help in charge carrier separation and preventing unwanted recombination. The doping concentration influences the position of the Fermi level, as increasing the doping concentration improves charge separation efficiency but may also lead to higher recombination rates at excessively high doping levels.

Under short-circuit conditions, light absorption induces photogeneration, leading to increased carrier density within the device and the splitting of the quasi-Fermi levels into E_{fn} for electrons and E_{fp} for holes. The separation of charge carriers improves photovoltaic conversion efficiency, allowing the cell to operate at maximum short-circuit current (J_{sc}) without external voltage influence. Although the band bending is reduced, particularly within the P-type GaAs base layer of the bottom sub-cell, the overall built-in voltage remains at V_d , as in thermal equilibrium. This is because no photo-carrier accumulation occurs at the cell edges under short-circuit conditions, where the current density reaches its maximum value, J_{sc} . Under opencircuit conditions, photo-carrier accumulation at the cell edges reaches its peak, as charge photogeneration and separation occur in the absence of current flow. This leads to a pronounced splitting of the quasi-Fermi levels, E_{fn} and E_{fp} , indicating the generation of a substantial photovoltage due to efficient photon absorption and charge carrier separation. Consequently, band bending is significantly reduced within both the P-type $In_{0.4}Ga_{0.6}$ P base layer of the top sub-cell and the P-type GaAs base layer of the bottom sub-cell, while the built-in voltage decreases relative to V_d due to the forward bias photovoltage effect.

Figure III.33 presents the J-V characteristics of the top sub-cell, bottom sub-cell, and tandem solar cell, showcasing the impact of combining different absorber layers on overall photovoltaic performance.

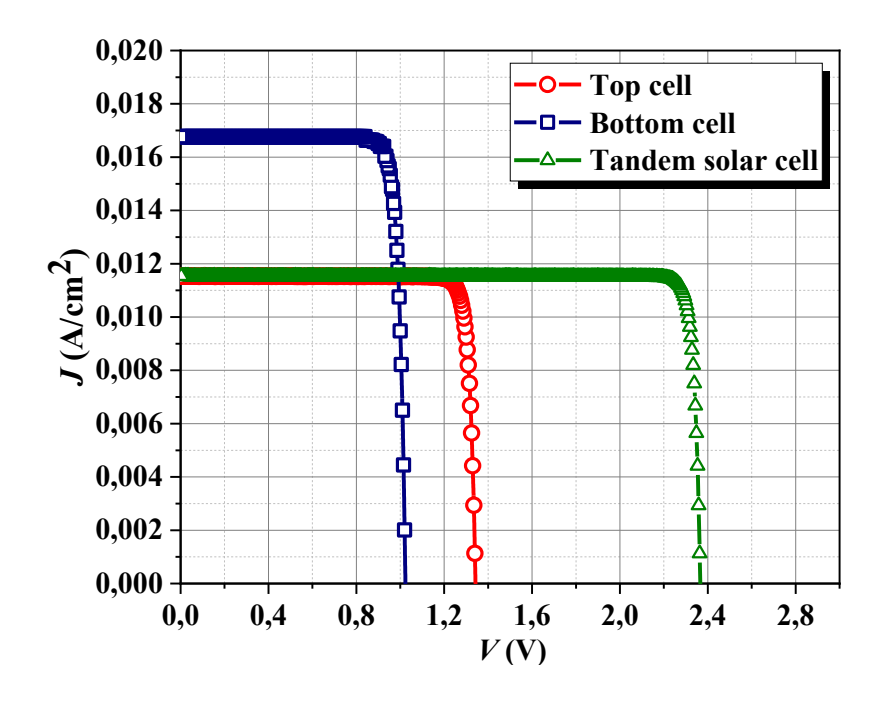


Figure III.33: J - V characteristics of the top sub-cell, bottom sub-cell, and tandem solar cell based on GaInP/GaAs heterojunction, under the AM1.5 standard solar spectrum.

Table III.8: Photovoltaic output parameters of the top sub-cell, bottom sub-cell, and tandem solar cell based on GaInP/GaAs heterojunction.

	$J_{sc}(mA/cm^2)$	$V_{oc}(\mathbf{V})$	FF (%)	$P_{max} (W/cm^2)$	$E_{ff}(\%)$
Top sub-cell	11.529	1.342	90.32	0.01398	14.08
Bottom sub-cell	16.768	1.023	88.38	0.01516	15.27
Tandem solar cell	11.529	2.366	93.81	0.02559	25.77

The top sub-cell exhibits a short-circuit current density (J_{sc}) of 11.529 mA/cm² and an open-circuit voltage (V_{oc}) of 1.342 V, leading to a conversion efficiency of 14.08%, while the bottom sub-cell demonstrates a higher J_{sc} of 16.768 mA/cm² but a lower V_{oc} of 1.023 V, achieving an efficiency of 15.27%. The tandem solar cell, integrating both sub-cells, follows the characteristic behavior of multi-junction devices, where the J_{sc} is limited by the lowest J_{sc} among the sub-cells—resulting in a value of 11.52 mA/cm². However, the open-circuit voltage in the tandem structure is additive, yielding a higher V_{oc} of 2.366 V. Consequently, the enhanced voltage compensation enables the tandem solar cell to achieve a conversion efficiency of 25.77% as shown on Table III.8.

To enhance the output photo-parameters of the tandem solar cell, we aim to achieve current matching between the top and bottom sub-cells by optimizing the base layer thickness (P-type $In_{0.4}Ga_{0.6}P$) of the top sub-cell within the range of [0.1 μ m - 1 μ m]. As illustrated in Figure III.34, and Table III.9, increasing the base layer thickness of the top sub-cell leads to a notable rise in its short-circuit current density (J_{sc}), from 11.529 mA/cm² to 16.768 mA/cm², aligning it with the J_{sc} value of the bottom sub-cell. Additionally, the open-circuit voltage (V_{oc}) of the top sub-cell experiences a slight improvement, reaching 1.357 V. Consequently, the conversion efficiency of the top sub-cell is significantly enhanced to 20.65% when its base layer thickness is optimized at 0.94 μ m. This adjustment successfully balances the photogeneration and carrier collection processes, contributing to better overall tandem solar cell performance.

Figure III.35 and Table III.9 illustrate the remarkable enhancement of the tandem solar cell's output photo-parameters following the achievement of the current matching condition between the top and bottom sub-cells.

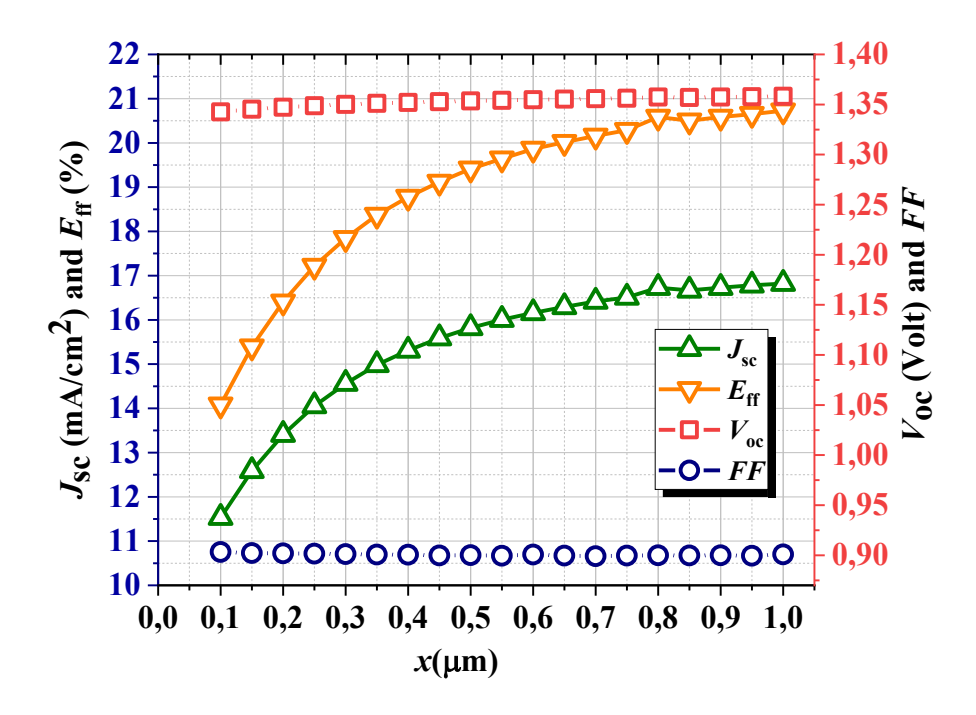


Figure III.34: Dependence of the top sub-cell output photo-parameters on the base layer thickness (P-type $In_{0.4}Ga_{0.6}P$) of the top sub-cell.

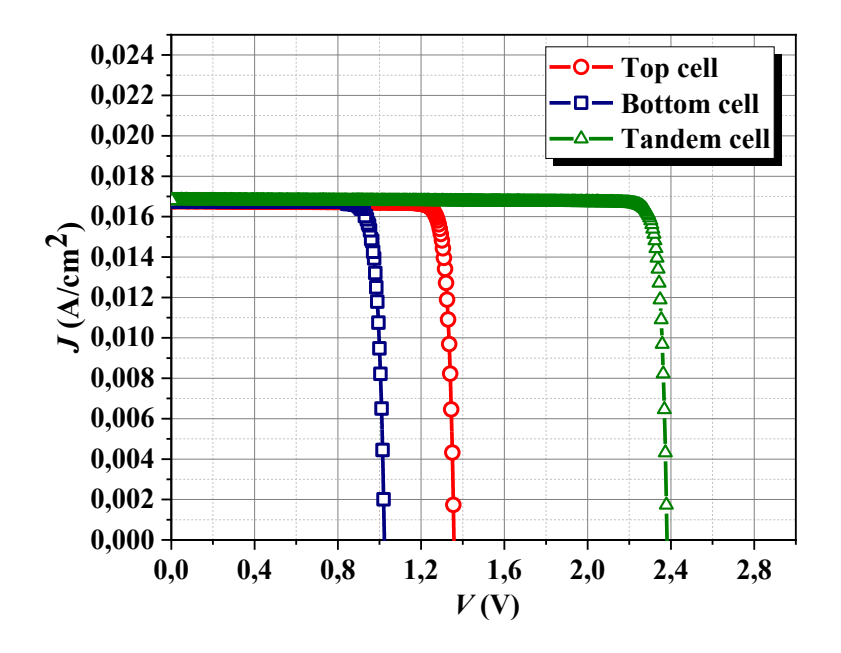


Figure III.35: J - V characteristics of the top sub-cell, bottom sub-cell, and tandem solar cell based on GaInP/GaAs heterojunction under the AM1.5 standard solar spectrum, with the achievement of the current matching condition between the top and bottom sub-cells.

Table III.9: Photovoltaic output parameters of the top sub-cell, bottom sub-cell, and tandem solar cell based on GaInP/GaAs heterojunction, with the achievement of the current matching condition between the top and bottom sub-cells.

	$J_{sc}(mA/cm^2)$	$V_{oc}(V)$	FF (%)	$P_{max} (W/cm^2)$	$E_{ff}(\%)$
Top sub-cell	16.768	1.357	90.04	0.02050	20.65
Bottom sub-cell	16.768	1.023	88.38	0.01516	15.27
Tandem solar cell	16.768	2.381	89.33	0.03566	35.93

This optimization results in a significant increase in the short-circuit current density (J_{sc}) , reaching 16.768 mA/cm², while the open-circuit voltage (V_{oc}) improves to 2.381 V. Consequently, the conversion efficiency (E_{ff}) is elevated to an impressive 35.93%, demonstrating the effectiveness of current matching in maximizing the photovoltaic performance of the tandem solar cell. The improved obtained E_{ff} is within the range [35%-36.86%] reached by recent works of Makambo. et al. [12].

III.5 Conclusion

This chapter analysed the performance of multi-layer GaInP/GaAs heterojunction solar cells, focusing on single-junction and dual-junction tandem configurations under standard AM1.5 solar irradiation, with an optical power of $P_{opt}=0.099271\,W/cm^2$ and an ambient temperature of T=300K. Using Solis-1D simulation software, we examined the electrical properties, including J-V and P-V characteristics, deriving key photovoltaic parameters such as short-circuit current density (J_{sc}), open-circuit voltage (V_{oc}), maximum output power (P_{max}), fill factor (FF) and photovoltaic conversion efficiency (E_{ff}). For the single-junction cell, optimization focused on adjusting the thickness and doping levels of various layers. The results showed that increasing the thicknesses of N⁺-type $In_{0.4}Ga_{0.6}P$ or N⁺-type $In_{0.5}Ga_{0.5}P$ layers led to a continuous decrease in J_{sc} and E_{ff} . However, increasing the thickness of the P-type GaAs base layer significantly enhanced efficiency, while variations in doping concentration influenced recombination rates and voltage stability. The optimal configuration was achieved by reducing the thickness of the second (N⁺-type $In_{0.4}Ga_{0.6}P$) and the third (N⁺-type $In_{0.5}Ga_{0.5}P$) layers to their minimum possible value of 0.01 μ m while increasing the thickness of the P-type GaAs base layer (fourth layer) to 3.5 μ m and doping it with $N_a=10^{17}cm^{-3}$. This configuration

Chapter III: Study of Multilayer Solar Cells Based on GaInP/GaAs Heterojunction

provided impressive output photo-parameters, achieving an efficiency (E_{ff}) of 29.088%, J_{sc} of 32.29 mA/ cm^2 , V_{oc} of 1.0158 V, and FF of 88.032%.

The tandem solar cell initially exhibited a J_{sc} of 11.52 mA/cm² and a V_{oc} of 2.366 V with a conversion efficiency of 25.77%. However, further optimization through current matching between the top and bottom sub-cells, achieved by increasing the thickness of the P-type $In_{0.4}Ga_{0.6}P$ base layer of the top sub-cell, led to a final efficiency of 35.93%. These findings highlight the critical role of current matching in maximizing the photovoltaic performance of GaInP/GaAs tandem solar cells.

III.6. References

- [1] M. H. Zehender., S. A. Svatek, M. A. Steiner, I. García, P. García Linares, E. L Warren, A. Martí, A. C. Tamboli, & E. Antolín, (2021). Inverted GaInP/GaAs three-terminal heterojunction bipolar transistor solar cell. *IEEE Photovoltaic Specialists Conference*, https://doi.org/10.1109/PVSC45281.2020.9301000...
- [2] M. A. Steiner, R. M. France, J. Buencuerpo, J. F. Geisz, M. P. Nielsen, A. Pusch, W. J. Olavarria, M. Young, & N. J. Ekins-Daukes, (2020). High efficiency inverted GaAs and GaInP/GaAs solar cells with strain-balanced GaInAs/GaAsP quantum wells. *Advanced Energy Materials*, https://doi.org/10.1002/aenm.202002874.
- [3] A. Myllynen, T. Sadi & J. Oksanen, (2020). Interdigitated back-contact double-heterojunction GaInP/GaAs solar cells. *Progress in Photovoltaics: Research and Applications*, https://doi.org/10.1002/pip.3339.
- [4] S. Ould Saad Hamady, Solis: a modular, portable, and high-performance 1D semiconductor device simulator, J Comput Electron 19 (2020) 640–647. https://doi.org/10.1007/s10825-020-01477-7.
- [5] S. Selberherr, Analysis and Simulation of Semiconductor Devices, Springer Vienna (2012), 978-3-7091-8752-4. https://doi.org/10.1007/978-3-7091-8752-4.
- [6] D. L. Scharfetter and H. K. Gummel, Large-signal analysis of a silicon Read diode oscillator, IEEE Transactions on Electron Devices (1969), vol. 16, no. 1, pp. 64-77, https://doi.org/10.1109/T-ED.1969.16566.
- [7] Tecgraf/PUC-Rio Library Download IUP Portable User Interface Documentation, (1994–2017). https://documentation.help/IUP2.3/download_tips.html.
- [8] Scintilla and SciTE, (1998–2016). https://www.scintilla.org/.
- [9] S. Ould Saad Hamady, Solis 1D Semiconductor Device Simulator, manual (2023) http://www.hamady.org/download/solis_simulator.pdf.
- [10] J. Pastuszak, P. Węgierek, Photovoltaic Cell Generations and Current Research Directions for Their Development, Materials 15 (2022) 5542. https://doi.org/10.3390/ma15165542

Chapter III: Study of Multilayer Solar Cells Based on GaInP/GaAs Heterojunction

- [11] S. Ghosh, R. Yadav, Future of photovoltaic technologies: A comprehensive review, Sustainable Energy Technologies and Assessments 47 (2021) 101410. https://doi.org/10.1016/j.seta.2021.101410.
- [12] J.B. Makambo, P.E. Imoisili, T.C. Jen, Efficiency Assessment of GaInp/GaAs Tandem Solar Cells: Analytical Investigation and Numerical Simulation, Key Engineering Materials 997 (2024) 53–60. https://doi.org/10.4028/p-MO0K1l.

General conclusion

Multi-layer solar cells utilizing the GaInP/GaAs heterojunction offer significant advantages, primarily due to the exceptional electronic properties of GaInP and GaAs, such as high absorption coefficients and the ability to tune the energy bandgap E_g ; which ensure optimal utilization of the solar spectrum, and contribute to enhanced optical absorption and efficient charge carrier transport. Furthermore, the excellent lattice matching between GaInP and GaAs minimizes defect formation at the interface, preserving carrier mobility and reducing recombination losses. When incorporated into a multi-layer architecture, this interaction between the materials enables improved spectral absorption, enhancing the generation of photogenerated carriers and leading to a substantial increase in photovoltaic conversion efficiency. The precise control over the energy bandgap in this heterojunction structure allows for personalised performance optimization, making GaInP/GaAs-based multi-junction solar cells a convincing choice for achieving higher efficiency in advanced photovoltaic technologies.

In this work, we presented a study of a multi-layer solar cell based on the GaInP/GaAs heterojunction, examining both single-junction and dual-junction tandem configurations. The analysis assumes standard AM1.5 solar irradiation with an optical power $P_{opt} = 0.099271 \, W/cm^2$ at an ambient temperature of 300 K. Numerical simulations using Solis-1D software enabled the evaluation of key electrical properties, including current density-voltage (J - V) and power-voltage (P - V) characteristics, from which crucial photovoltaic performance parameters were derived: short-circuit current density (J_{sc}) , open-circuit voltage (V_{oc}) , maximum output power (P_{max}) , fill factor (FF) and photovoltaic conversion efficiency (E_{ff}) .

Single-junction cell findings

The initial configuration of the single-junction solar cell yielded J_{sc} of 29.227 mA/cm^2 , V_{oc} of 1.039 V, P_{max} of 0.02671 W/cm^2 , FF of 87.58% and overall efficiency (E_{ff}) of 26.90%. By adjusting the thickness of the second layer (N⁺-type In_{0.4}Ga_{0.6}P) between 0.01 μ m and 0.5 μ m, a significant reduction in J_{sc} was observed, decreasing the efficiency from 27.15% to 20.88%. Similarly, modifying the thickness of the third layer (N⁺-type In_{0.5}Ga_{0.5}P) in the same range led to a pronounced decline in J_{sc} , reducing efficiency from 27.01% to 18.17%. However, increasing the thickness of the fourth layer (P-type GaAs) from 0.1 μ m to 3.5 μ m resulted in a notable improvement, enhancing J_{sc} and boosting efficiency from 18.23% to 28.68% due to increased optical absorption. Adjusting the doping concentration (N_a) of the P-type GaAs layer between

 10^{14} cm⁻³ and 10^{19} cm⁻³ revealed a slight decline in J_{sc} due to sensitive recombination, while V_{oc} and FF steadily improved, peaking at an efficiency of 27.01% for a doping level of 10^{18} cm⁻³. Optimizing the single-junction cell by minimizing the second- and third-layers' thickness to 0.01 µm, expanding the base layer to 3.5 µm, and doping it at 10^{17} cm⁻³, resulted in J_{sc} of 32.29 mA/ cm^2 , V_{oc} of 1.0158 V, FF of 88.032%. and efficiency of 29.088%.

Dual-junction tandem cell findings

The initial tandem solar cell configuration produced J_{sc} of 11.52 mA/cm² and V_{oc} of 2.366 V, yielding an efficiency of 25.77%. The top sub-cell exhibited J_{sc} of 11.529 mA/cm² and V_{oc} of 1.342 V, achieving 14.08% efficiency, while the bottom sub-cell recorded J_{sc} of 16.768 mA/cm² and V_{oc} of 1.023 V, achieving 15.27% efficiency. To enhance the tandem cell's output, current matching between the top and bottom sub-cells was achieved by increasing the base layer thickness (P-type $In_{0.4}Ga_{0.6}P$) of the top sub-cell from 0.1 µm to 1 µm. This modification improved J_{sc} in the top sub-cell from 11.529 mA/cm² to 16.768 mA/cm², ensuring alignment with the bottom sub-cell's J_{sc} , while V_{oc} of the top sub-cell increased slightly to 1.357 V, raising its efficiency to 20.65% at an optimized base layer thickness of 0.94 µm. The optimization strategy led to a remarkable improvement in tandem cell performance, enhancing J_{sc} to 16.768 mA/cm², V_{oc} to 2.381 V, and achieving an impressive final efficiency of 35.93%. These results underscore the critical role of current matching in maximizing photovoltaic performance for GaInP/GaAs-based tandem solar cells.

Abstract

We conducted a study on multilayer solar cells based on a GaInP/GaAs heterojunction, analysing the performance of both single-junction and dual-junction tandem solar cells under standard solar irradiation conditions (AM1.5), with an optical power of $P_{opt} = 0.099271 \, W/cm^2$ at a temperature of T = 300K. Using Solis-1D simulation software, we determined the electrical characteristics of these solar cells, including current density-voltage (I-V) and power-voltage (P-V) profiles, and extracted key photovoltaic parameters such as short-circuit current density (J_{sc}) , open-circuit voltage (V_{oc}) , maximum power (P_{max}) , fill factor (FF), and conversion efficiency (E_{ff}) . For the single-junction solar cell, our investigation focused on optimizing layer thickness and doping concentrations to maximize conversion efficiency. The results revealed that reducing the thickness of the N⁺-type $In_{0.4}Ga_{0.6}P$ and N⁺-type $In_{0.5}Ga_{0.5}P$ layers to 0.01 μm , while simultaneously increasing the P-type GaAs base layer thickness to 3.5 µm and doping it at a concentration of $10^{17} cm^{-3}$, significantly enhanced the conversion efficiency (E_{ff}) from 26.92% to 29.088%. For the dual-junction tandem solar cell, performance was further improved by increasing the thickness of the P-type $In_{0.4}Ga_{0.6}P$ base layer in the top sub-cell to 0.94 μm . This optimization facilitated current density matching (J_{sc}) between the top and bottom sub-cells, ultimately raising the overall efficiency from 25.77% to 35.93%. These findings underscore the crucial role of doping concentration and layer thickness optimization, as well as current matching between sub-cells, in enhancing photovoltaic performance and maximizing solar cell efficiency, thus contributing to the development of advanced solar energy technologies.

Keywords: GaInP/GaAs heterojunction; Solar cells; Multilayers; Solis-1D; Conversion efficiency; Solar energy.

ملخص

أجرينا دراسة على الخلايا الشمسية متعددة الطبقات القائمة على الوصلة غير المتجانسة GalnP/GaAs ، حيث قمنا بتحليل أداء كلِّ من الخلايا الشمسية ذات الوصلة الأحادية والخلايا الشمسية الترادفية مزدوجة الوصلة تحت ظروف الإشعاع الشمسي القياسي(AM1.5) باستطاعة ضوئية $P_{opt}=0.099271~W/cm^2$ و عند درجة حرارة الإشعاع الشمسية القياسي(AM1.5) باستطاعة ضوئية Solis-1D لحساب الخصائص الكهربائية لهذه الخلايا الشمسية، بما في ذلك منحنيات كثافة التيار-الجهد (J-V) والاستطاعة-الجهد (P-V) ، واستخرجنا الوسائط الفوطوفولطائية الرئيسية، مثل كثافة تيار الدارة القصيرة(J-V) ، جهد الدارة المفتوحة (V_{oc}) ، الاستطاعة الأعظمية (P-V) ، معامل التعبئة (P-V) ، معامل التعبئة وكثاءة أو مردود التحويل الفوطوفولطائي (F_f) . بالنسبة للخلية الشمسية ذات الوصلة الأحادية ، ركّزت دراستنا على تحسين سُمك الطبقات وتركيزات التطعيم لتحقيق أعلى كفاءة تحويل. وأظهرت النتائج أن تقليل سُمك طبقي النوع P الى 10.0 ميكرومتر، مع زيادة سُمك طبقة القاعدة GaAs من النوع P إلى 25.08 ميكرومتر، مع زيادة سُمك طبقة القاعدة المردود التحويل (E_{ff}) من 10.17 أدى إلى زيادة مردود التحويل (E_{ff}) من 26.92% إلى 829.08% القاعدة P في الخلية الفرعية العلوية إلى 0.94 ميكرومتر، مما ساعد على تحقيق توافق في كثافة التيار (J_{sc}) بين الخلايا الفرعية (العلوية والسفلية)، وبالتالي رفع المردود الكلي من 25.27% إلى 25.5% الى 35.5% المردود الكلي من 25.5% إلى 35.6%.

تؤكد هذه النتائج على أهمية تحسين تركيز التطعيم وسُمك الطبقات، بالإضافة إلى تحقيق توافق التيار بين الخلايا الفرعية، لتعزيز الأداء الفوطوفولطائي وزيادة كفاءة تحويل الطاقة الشمسية ، مما يسهم في تطوير تقنيات الطاقة الشمسية المتقدمة.

الكلمات المفتاحية: الوصلة غير المتجانسةGaInP/GaAs ؛ الخلايا الشمسية؛ الطبقات المتعددة:Solis-1D ؛ كفاءة الكلمات التحويل؛ الطاقة الشمسية.

REPUBLIQUE ALGERIENNE DEMOCRATIQUE ET POPULAIRE MINISTERE DE L'ENSEIGNEMENT SUPERIEUR ET DE LA RECHERCHE SCIENTIFIQUE UNIVERSITE MOHAMED KHIDER - BISKRA



الجمهورية الجزائرية الديمقراطية الشعبية وزارد التعليم العالي والبحث العلمي جامعة محمح خيضر بسكرة كلبة العلوم الدنبيقة

Faculté des SE

Département des Sciences de la matière

قسم :علوم المادة

Filière: Physique

تصريح شرفسي

خاص بالالتزام بقواعد النزاهة العلمية لإنجاز بحث

(ملحق القرار 1082 المؤرخ في 2021/12/27)

شعبة :الفيزياء

أنا الممضى أسفله،

	السيد(ة):بن الصمي. و عاع
الصفة: طالب سنة ثانية ماستر عيزباء	تخصص: هَيِن بِاعد عَلَمَ عَن الْلِهُ وَهِا قَا نَ مَعْجِه وَ وَ اللّهُ وَهِا قَا نَ مَعْجِه وَ وَ اللّهُ المامل(ة) لبطاقة التعريف الوطنية رقم: .666.4.606 ك.0
. الصادرة بتاريخ2.3/9./9 40.19	الحامل(ة) لبطاقة التعريف الوطنية رقم: .606.1/.0.6. ك. ٥
وم المادة	المسجل بكلية: ١١ لعلوم ١١ لد عَمِعَهُفسم: عل
	والمكلف بانجاز أعمال بحث : مذكرة
Study of me	eltilager Solar cells Based sieis
	eltilager Solar cells Based : wilsie Inflora As Reterojunction

أصرح بشرفي أني ألتزم بمراعاة المعايير العلمية والمنهجية ومعايير الأخلاقيات المهنية والنزاهة الأكاديمية المطلوبة في انجاز البحث المذكور أعلاه وفق ما ينص عليه القرار رقم 1082 المؤرخ في 2021/12/27 المحدد للقواعد المتعلقة بالوقاية من السرقة العلمية ومكافحتها.

التاريخ: 25/22/ 5م/ 55 م م

إمضاء المعنى بالأمر